(2)

AD-A212 099

REPORT DOCUMENTATION PAGE

ELECTE SEP 11 1989 S D B

1b RESTRICTIVE MARKINGS [illegible] FILE COP

2a SECURITY CLASSIFICATION AUTHORITY
UNCLASSIFIED

2b DECLASSIFICATION / DOWNGRADING SCHEDULE

3 DISTRIBUTION / AVAILABILITY OF REPORT
Approved for public release, distribution unlimited.

4. PERFORMING ORGANIZATION REPORT NUMBER(S)

5 MONITORING ORGANIZATION REPORT NUMBER(S)
AFOSR-TR- 89-1230

6a NAME OF PERFORMING ORGANIZATION
Mech. & Nuc. Engr. Dept.
Mississippi State University

6b OFFICE SYMBOL (If applicable)

7a NAME OF MONITORING ORGANIZATION
Air Force Office of Scientific Research

6c. ADDRESS (City, State, and ZIP Code)
P. O. Drawer ME
Mississippi State, MS 39762

7b ADDRESS (City, State, and ZIP Code)
Bolling Air Force Base
Washington, DC 20332

8a. NAME OF FUNDING / SPONSORING ORGANIZATION AFOSR

8b OFFICE SYMBOL (If applicable)
AFOSR/NA

9 PROCUREMENT INSTRUMENT IDENTIFICATION NUMBER
AFOSR-86-0178

8c. ADDRESS (City, State, and ZIP Code)
Bolling Air Force Base
Washington, DC 20332

10. SOURCE OF FUNDING NUMBERS

PROGRAM ELEMENT NO.	PROJECT NO.	TASK NO.	WORK UNIT ACCESSION NO
61102 F	2307	A4	

11 TITLE (Include Security Classification)
An Experimental Study of Surface Roughness Effects on Turbulent Boundary Layer Flow and Heat Transfer

12. PERSONAL AUTHOR(S)
Coleman, Hugh W.; Taylor, Robert P.; Hosni, M. H.; Brown, Glenn B.; Love, Philip H.

13a. TYPE OF REPORT ~~Final~~ Annual

13b. TIME COVERED FROM May 86 TO Mar 89

14. DATE OF REPORT (Year, Month, Day) 1989, April

15. PAGE COUNT 155

16. SUPPLEMENTARY NOTATION

17. COSATI CODES

FIELD	GROUP	SUB-GROUP

18. SUBJECT TERMS (Continue on reverse if necessary and identify by block number)
Turbulence and turbulent heat transfer

19. ABSTRACT (Continue on reverse if necessary and identify by block number)

The uncertainty analysis, design, and qualification of a Turbulent Heat Transfer Test Facility (THTTF) with a smooth wall test surface are presented, and initial results for a test surface roughened with hemispherical elements spaced four base diameters apart are discussed and compared with calculations from a previously developed discrete element prediction method. A description of the facility and discussions of details of the instrumentation systems, calibration procedures and uncertainties associated with the measurements are documented.

(Continued on reverse side.)

20. DISTRIBUTION / AVAILABILITY OF ABSTRACT
☒ UNCLASSIFIED/UNLIMITED ☐ SAME AS RPT. ☐ DTIC USERS

21. ABSTRACT SECURITY CLASSIFICATION
Unclassified

22a. NAME OF RESPONSIBLE INDIVIDUAL
Henry E. Helin

22b. TELEPHONE (Include Area Code)
(202) 767-4987

22c. OFFICE SYMBOL
AFOSR/NA

DD FORM 1473, 84 MAR

83 APR edition may be used until exhausted.
All other editions are obsolete.

SECURITY CLASSIFICATION OF THIS PAGE
UNCLASSIFIED

89 9 7 098

19. Abstract (Continued)

The smooth wall fluid dynamics data show that the facility was operating within the expected bounds over the Reynolds number range anticipated in future rough surface testing. The baseline smooth wall heat transfer data show that the qualification of the THTTF is complete and successful for x-Reynolds numbers up to 10 million. Constant wall temperature Stanton numbers determined using the energy balance technique are in excellent agreement with previous smooth wall data, which had been reported up to x-Reynolds numbers of 3.5 million. To the authors' knowledge, no smooth wall Stanton number data have been reported previously in the 3.5-10 million range covered by the THTTF data. Stanton numbers are determined in the THTTF to uncertainties of 2-5%, depending on flow conditions.

The initial rough wall data taken using the THTTF are for a surface roughened with hemispherical elements spaced four base diameters apart. The Stanton number and skin friction coefficient data are compared with predictions from the discrete element method using unmodified the roughness models developed previous to this effort. The skin friction predictions show excellent agreement with the data. This was not surprising considering the large size of the data base on which the roughness element drag coefficient model had been developed. The heat transfer predictions are in reasonably good agreement with the Stanton number data, although improvement would be desirable. Since the roughness element Nusselt number model was developed based on heat transfer data from the single rough surface used in the Stanford studies, it is encouraging that the heat transfer predictions are as good as they are. Further development of the roughness element Nusselt number model will be made when data are taken on additional rough surfaces in the THTTF.

PREFACE

This program was conducted by the Mechanical and Nuclear Engineering Department, Mississippi State University, P. O. Drawer ME, Mississippi State, MS 39762 under Grant AFOSR-86-0178 from the Air Force Office of Scientific Research, Bolling Air Force Base, Washington, DC 20332. Capt. Henry Helin managed the program for the Air Force Office of Scientific Research. The part of the program with which this report is concerned was conducted from May 1986 through April 1989.

The experimental apparatus used in this research program was acquired under Grant AFOSR-85-0075.

The authors wish to thank Capt. Hank Helin and Dr. Jim Wilson for their support and encouragement.

Accession For
NTIS GRA&I ☑
DTIC TAB ☐
Unannounced ☐
Justification
By
Distribution/
Availability Codes
Dist | Avail and/or Special
A-1

QUALITY INSPECTED 4

AFOSR-TR- 89-1230

AN EXPERIMENTAL STUDY OF SURFACE ROUGHNESS EFFECTS ON TURBULENT BOUNDARY LAYER FLOW AND HEAT TRANSFER

TABLE OF CONTENTS

Page

ABSTRACT i

PREFACE iii

NOMENCLATURE vi

SECTION 1 INTRODUCTION 1

- 1.1 BACKGROUND 1
- 1.2 OVERVIEW OF REPORT 4

SECTION 2 DESCRIPTION OF EXPERIMENTAL FACILITY 6

- 2.1 GENERAL DESCRIPTION 6
- 2.2 AIR FLOW SYSTEM 7
- 2.3 PLATE SYSTEM 9
- 2.4 COOLING WATER SYSTEM 11
- 2.5 DATA ACQUISITION SYSTEM 11

SECTION 3 SMOOTH WALL QUALIFICATION: FLUID DYNAMICS 17

- 3.1 FREESTREAM FLOW QUALITY 17
- 3.2 BOUNDARY LAYER TWO DIMENSIONALITY 18
- 3.3 SKIN FRICTION COEFFICIENT RESULTS 19
- 3.4 BOUNDARY LAYER PROFILE DATA 22

SECTION 4 SMOOTH WALL QUALIFICATION: HEAT TRANSFER 39

- 4.1 STANTON NUMBER RESULTS 39
- 4.2 TEMPERATURE PROFILE COMPARISON 43

SECTION 5 ADDITIONAL SMOOTH WALL HEAT TRANSFER RESULTS 53

- 5.1 THEORY 54
  - 5.1.1 Analogies 54
  - 5.1.2 Integral Equations 55
  - 5.1.3 Differential Equations 57
- 5.2 EXPERIMENTAL RESULTS 57
- 5.3 SUMMARY 62

TABLE OF CONTENTS (concluded)

SECTION 6 ROUGH WALL RESULTS 75
6.1 REVIEW OF THE DISCRETE ELEMENT PREDICTION MODEL 75
6.2 HEAT TRANSFER RESULTS 79
6.3 FLUID DYNAMICS RESULTS 80
SECTION 7 SUMMARY 100
REFERENCES 102
APPENDIX I EXPERIMENTAL STANTON NUMBER DETERMINATION AND ITS UNCERTAINTY ANALYSIS 108
APPENDIX II BOUNDARY LAYER PROBE MEASUREMENTS 138
APPENDIX III SKIN FRICTION COEFFICIENT DETERMINATION 145

NOMENCLATURE

A	plate surface area
B	bias limit
C_f	skin friction coefficient $(2\tau_w/\rho U_\infty^2)$
c_p	free stream specific heat
g	kernel function for specified heat flux
h	convective heat transfer coefficient
H	total enthalpy
ℓ_m	mixing length
P	pressure
Pr	Prandtl number
q_c	conductive heat loss rate
q_r	radiative heat loss rate
q_w''	wall heat flux
r	recovery factor
R	resistance
Re_x	Reynolds number based on x
Re_{xv}	Reynolds number based on xv (virtual origin)
Re_{δ_2}	momentum thickness Reynolds number $(\rho U_\infty \delta_2/\mu)$
Re_{Δ_2}	enthalpy thickness Reynolds number $(\rho U_\infty \Delta_2/\mu)$
Re_ϕ	Reynolds number based on unheated starting length
S	precision index
St	Stanton number $(h/\rho C_p U_\infty)$
t	95th percentile point for the two-tailed t distribution
T	total temperature
T_r	recovery temperature
T_o	freestream total temperature
T_p	plate surface temperature
T_w	top and side wall temperature
T_∞	freestream static temperature
T^+	nondimensional T $[(T_p - T)u^*/U_\infty(T_p - T_o)St]$

NOMENCLATURE (continued)

$\overline{t'v'}$	turbulent heat flux term
u	mean axial velocity
u_{eff}	effective velocity sensed by the hot-wire
U	95% coverage uncertainty
U_∞	free stream velocity
$(UA)_{eff}$	overall conductance for q_c calculation
u'	longitudinal velocity fluctuation
u'_{eff}	fluctuating component of effective velocity
$\overline{u'v'}$	Reynolds shear stress term
u^*	friction velocity $(U_\infty \sqrt{C_f/2})$
v	mean normal velocity
v'	normal velocity fluctuation
W	plate heater power
w'	transverse velocity fluctuation
x	longitudinal coordinate measured from nozzle exit plane
xv	longitudinal coordinate measured from virtual origin
y	coordinate normal to surface
y^+	nondimensional y (law of the wall) $y^+ = \frac{y}{\nu} u^*$

Greek

α	thermal diffusivity
β	incomplete Beta function
δ	boundary layer thickness
δ_1	displacement thickness
δ_2	momentum thickness
Δ	thermal boundary layer thickness
Δ_2	enthalpy thickness
ϵ	plate surface emissivity
κ	Karman constant
ϕ	unheated starting length
Γ	gamma function
μ	dynamic viscosity

NOMENCLATURE (concluded)

ν	kinematic viscosity
ρ	density
σ	Stephan-Boltzmann constant
τ	viscous shear stress

Subscripts

cal	calibration
inst	installation
Qt	quartz thermometer
t	turbulent
w	wall
∞	free stream

SECTION 1
INTRODUCTION

Heat transfer and skin friction can be significantly larger for a turbulent flow over a rough surface compared with an equivalent turbulent flow over a smooth surface. Many surfaces of engineering interest are rough in the aerodynamic sense. Missiles, re-entry vehicles, externally mounted stores on high performance aircraft, ship hulls, turbine blades, heat exchangers, piping networks and atmospheric flows are examples of systems in which surface roughness can play an important role in heat transfer and skin friction. In light of this broad applicability, there is significant engineering interest in the development of accurate predictive models for heat transfer and fluid mechanics in turbulent flow over rough surfaces.

1.1 BACKGROUND

Given the geometry of an object immersed in a flowfield, a specification of the freestream flow conditions, and a geometrical description of the roughness of the system surfaces, an analyst or designer would like at least to be able to predict the surface shear distribution, the heat transfer distribution, and the total drag. In the past, most of the research effort was to develop computational methods for various geometrics with smooth surfaces, and the roughness problem has received relatively little attention. However, many systems of engineering interest have surfaces which are aerodynamically rough. Therefore, if the heat transfer and fluid dynamics are to be predicted, computational procedures to model the effects of rough surfaces must be developed and proven by comparison with well-documented data sets.

Schlichting 1936 [1] experimentally investigated the fluid dynamics of this type of problem. He related his skin friction results on a range of well-described rough surfaces to the previous results obtained by Nikuradse 1933 [2] for sand-roughened pipes through definition of an equivalent sandgrain roughness. In subsequent surface roughness effects investigations, workers used these results of Schlichting and the equivalent sandgrain roughness concept to analyze their experimental data and to develop analytical models for use in predictive methods.

Over the past decade or so, a predictive approach called the discrete element method, which does not use the equivalent sandgrain roughness concept, has been used with varying degrees of rigor by several groups of researchers (Finson 1975 [3], Adams and Hodge 1977 [4], Finson and Wu 1979 [5], Finson and Clark 1980 [6], Lin and Bywater 1980 [7], Finson 1982 [8], Coleman, Hodge, and Taylor 1983 [9], Taylor, Coleman and Hodge 1985 [10]). Such approaches rely on empirical input in order to calibrate the roughness models.

Most of the roughness-influenced turbulence data taken over the years has been on ill-defined rough surfaces, with the reported results having equivalent sandgrain roughness values implicitly included at some stage of the data reduction. Recently, Coleman, Hodge, and Taylor 1983 [9] found that Schlichting had made erroneous assumptions during his data reduction which had significant effects on the data which he reported. The reevaluation of Schlichting's data (Coleman, Hodge, and Taylor 1984 [11]) showed that his skin friction results were too large by amounts ranging up to 73% and that his reported equivalent sandgrain roughness values were high by amounts ranging from 26% to 555%. These findings caused some consternation since practically all work since the 1930's on surface roughness effects relied significantly on either the skin friction or equivalent sandgrain roughness results as originally reported by Schlichting.

A series of data sets taken at Stanford University (Healzer 1974 [12], Pimenta 1975 [13], Coleman 1976 [14], Ligrani 1979 [15]) have been the only ones reported for a well-defined rough surface that contain heat transfer and skin friction distributions and velocity, temperature and Reynolds stress profiles. However, these data sets are for a single rough surface comprised of spheres of a single size packed in the most dense array. Holden 1983 [16] reported heat transfer and skin friction distribution measurements on well-defined surface roughness on cones, but the data were taken at hypersonic flow conditions.

Considering the limited range of previously reported rough surface data, it became apparent that there existed a critical need for accurate, precise, comprehensive data sets on both the heat transfer and the fluid dynamics in turbulent flow over well-defined rough surfaces. It was concluded that if a reasonable predictive capability is to be developed, then the additional experimental information (particularly for heat transfer) must be obtained. Recognition of this need led to funding under the DOD-University Research Instrumentation Program of a water tunnel facility and the Turbulent Heat Transfer Test Facility (THTTF) in the Thermal & Fluid Dynamics Laboratory at Mississippi State University. A comprehensive investigation of the effects of surface roughness element size, spacing and shape on skin friction in fully developed pipe flow over a wide range of Reynolds numbers was recently completed using the water tunnel facility in this laboratory [17-21].

The research program discussed in this report is intended to provide accurate, comprehensive sets of measurements of Stanton number distributions, skin friction coefficient distributions, and profiles of velocity, temperature and Reynolds stresses in turbulent boundary layer flows over surfaces roughened with well-defined roughness elements. These data will be used to improve and extend the roughness models in the discrete element prediction method, thus expanding our capability to predict the effects of surface roughness on turbulent flow and heat transfer.

The current phase of the research program will use six different test surfaces in the THTTF--one smooth and five rough. The smooth surface tests serve as a qualification check on the test facility and experimental procedures. Three of the rough test surfaces consist of smooth plates roughened with hemispherical roughness elements of 1.27 mm diameter spaced 2, 4, and 10 base diameters apart, respectively. The other two rough test surfaces consist of smooth plates roughened with elements that are truncated right circular cones of 1.27 mm base diameter with spacings of 2 and 4 base diameters, respectively.

The experimental plan is to test each set of surfaces with basic boundary conditions of zero pressure gradient and constant wall temperature over a number of freestream velocities between about 6 and 67 m/s such that the total set of data will thoroughly cover behavior in the aerodynamically smooth, transitionally rough, and fully rough regimes. The heat transfer data are the most critical, since the only such data currently available on a well-described rough surface are those from the previously discussed Stanford experiments, which used a single rough surface composed of 1.27 mm diameter spheres packed in the most dense array.

The THTTF was designed so that the 24 test plates, which make up its test surface, can be replaced with a new set without completely tearing down the test section. Some re-instrumentation, calibration and qualification is necessary for each new set of test plates, however, to maintain the high accuracy and precision which are an inherent part of the overall objective of this test program.

1.2 OVERVIEW OF REPORT

This report presents results for the smooth test surface and a rough surface with hemispherical elements at a spacing of four base diameters. The first tests were the calibration, qualification and general "shake-down" of the facility using the smooth test surface. The ability to reproduce accepted smooth wall results for non-isothermal turbulent boundary layer flow in the THTTF was deemed necessary before proceeding with rough wall investigations using the facility. In addition, the smooth wall data provide an appropriate baseline with which to compare the data obtained for rough walls using the same test apparatus.

This report is organized in the following manner. In Section 2, the THTTF and each of its four sub-systems are described. In Section 3, smooth wall fluid dynamics data including skin friction coefficient distributions and boundary layer profiles of mean velocity and Reynolds stresses are presented and compared to accepted, previously reported smooth wall data. The smooth wall qualification heat transfer data, including Stanton number distributions and boundary layer temperature profiles, are presented and compared to accepted, previously reported smooth wall data in Section 4. Also presented are Stanton number data which extend the previously published smooth wall data from x-Reynolds numbers of 3.5 million to 10 million. In Section 5, additional smooth wall heat transfer results are presented for a variety of non-constant wall temperature boundary conditions. In Section 6, the fluid dynamics and heat transfer data from the rough wall are presented and compared with calculations from the discrete element prediction method. The results from the research program are summarized in Section 7.

Detailed discussions of the experimental determination of Stanton number, its uncertainties, and estimates of the uncertainties in the various experimental measurements are presented in Appendix I. Probe measurements and calibrations are described in Appendix II for the hot-wire and thermocouple probes, while the determination of skin friction coefficients is covered in Appendix III.

SECTION 2

DESCRIPTION OF EXPERIMENTAL FACILITY

The Turbulent Heat Transfer Test Facility (THTTF) was constructed for the experimental investigation of heat transfer and fluid dynamics behavior in turbulent boundary layers over rough surfaces. The design of the THTTF was based on the preliminary analysis and design work of Norton 1983 [22]. The THTTF is geometrically similar to the test apparatus used in the Stanford University program that investigated turbulent boundary layer flow and heat transfer in flow over a single, porous rough surface with transpiration (Healzer 1974 [12], Pimenta 1975 [13], Coleman 1976 [14], Ligrani 1979 [15]).

2.1 GENERAL DESCRIPTION

The THTTF, shown schematically in Figure 1, is a closed loop subsonic wind tunnel designed to deliver a uniform air flow over a set of 24 individually heated flat test plates which are abutted together to form a continuous flat surface. Each plate can be maintained at a constant uniform temperature, and each set of rough plates has a well defined surface roughness. The Stanton number distribution along the test surface is obtained by applying an energy balance to each test plate. Distribution of the local skin friction coefficient along the test surface and other boundary layer parameters are determined with hot-wire anemometry. Thermal boundary layer parameters are determined from temperature profiles measured with a thermocouple probe and the appropriate hot-wire data.

Measurement of individual variables such as air velocity and plate temperature, the calibration of the instruments used to measure these variables, the determination of experimental Stanton numbers from these measured variables, and an analysis of the uncertainty associated with these Stanton numbers are presented in

Appendix I. The boundary layer probe measurement techniques are given in Appendix II, and the methods of determining local skin friction coefficients are discussed in Appendix III.

Four primary systems are required for the proper operation of the THTTF: (1) the air flow system, (2) the test plate system, (3) the cooling water system, and (4) the Automated Data Acquisition and Control System (ADACS). These are discussed in detail below.

2.2 AIR FLOW SYSTEM

The air flow system is a closed loop system designed to deliver a uniform velocity (6 to 67 m/s), low turbulence intensity, controlled temperature air flow at the 10.2 by 50.8 cm (4.0 by 20.0 in) inlet of the 2.4 m (8.0 ft) long test section which contains the test surface. These air velocities correspond to an x-Reynolds number range of about one million to ten million at the downstream end of the test section. A Buffalo Forge size 45AW industrial blower is the prime mover for the air flow system. The blower has a rating of 198 cubic meters of air per minute at 38 cm of water static pressure. An 18.6 kilowatt (25-hp) Dynamatic Model ACM-280 electric motor with an Eaton variable speed eddy current clutch drive system drives the blower with a belt and pulley system. Air velocity in the test section is set using the Eaton eddy clutch controller to control the rotation speed of the blower. The controller can be adjusted and set using a manually adjusted potentiometer or a dc-voltage signal from the ADACS.

Air exiting the blower enters a 1.2 m wide by 0.6 m tall wooden overhead duct which is connected to the blower and header by flexible couplings. The air then turns through the header and passes through a linen cloth filter in the filter box. Next the air passes through an air/water heat exchanger with a 4 row cooling coil. Upon leaving the heat exchanger, the air passes through a 3.8 cm thick aluminum honeycomb with a cell length-to-diameter ratio of 6 and then through a series of 4 woven stainless steel screens with an open area-ratio of 0.598 and a wire diameter of 0.136 mm.

Following the screens, the air enters a three-dimensional, 19.8 to 1 contraction ratio fiberglass nozzle with a 84 cm by 122 cm (33 in by 48 in) inlet and a 10 cm by 51 cm (4 in by 20 in) outlet. The nozzle was designed (Healzer 1974 [12]) to smoothly accelerate the flow without separation at the nozzle inlet or outlet. Uniform velocity air is delivered from the nozzle to the test section inlet. Measurements at freestream air velocities of 12 and 28 m/s indicated the axial velocity at the nozzle exit is uniform within about 0.5%. Freestream turbulence intensities measured 4 cm downstream of the nozzle exit were less than 0.3% for freestream velocities from 61 m/s down to 6 m/s and less than 0.4% at 3 m/s.

The test section has clear cast acrylic (plexiglass) sidewalls of 1.3 cm thickness and an adjustable, flexible, clear cast acrylic top of 1.3 cm thickness. The bottom wall is made up of the test plates. Static pressure taps, spaced every 10.2 cm even with the center of each plate in the test surface, are located in one of the sidewalls approximately 2.5 cm above the plates. Access holes for test probes are located along the center of the top wall, centered over each plate, and transversely at strategic locations. The holes are plugged with precision machined acrylic stoppers when probe access is not required.

The flexible upper surface of the test section can be adjusted to maintain the prescribed zero pressure gradient along the flow direction. A Dwyer inclined water manometer with a resolution of 0.06 mm of water was connected to the static pressure taps along the sidewall of the test section to measure the pressure gradient in the flow direction. The difference in static pressure in the test section between all pressure tap locations and that tap located at the second plate was maintained at less than 0.19 mm of water for a velocity of 12 m/s and to less than 0.32 mm of water for a velocity of 43 m/s.

As it exits the test section, the air passes through an adjustable plexiglass diffuser which links the test section to a vaned wooden diffuser. Easily removed screen inserts, which are used to produce a pressure drop and thus used as a coarse adjustment of the absolute static pressure level in the test section, are located at the entrance of the wooden diffuser. Following the vaned diffuser, the air enters the blower plenum from which it passes through a flexible coupling into the blower intake.

Suction and ejection of air to and from the test section through any small air gaps in the test section were minimized by equalization of the test section static pressure with the ambient pressure. Filtered make-up air to replace the inevitable air leakage from the overhead ducting, filter boxes, and heat exchanger was ducted through a box of adjustable orifices to the blower plenum. Very fine balancing of the test section air static pressure and the ambient pressure, typically to within ±0.13 mm of water, was accomplished by adjusting the orifices in the make-up air box.

In order to minimize vibrations, the blower and blower motor, which are the primary sources of mechanical vibrations, are mounted on a massive concrete pad with vibration dampening feet. Transfer of mechanical vibrations throughout the THTTF has been minimized by the use of non-rigid joints at key locations in the flow path to effectively isolate the test section from vibration sources. Noise from air flowing in the overhead duct, plenum, and header has been reduced by lining these air passages with batt insulation covered by rigid fiberglass insulation board. Blower and blower motor noise have been reduced by housing the blower and motor in vented, insulation-lined boxes.

2.3 PLATE SYSTEM

A cross sectional view of the test section is shown in Figure 2. The test plates are supported on precision straight edges which are thermally isolated from the steel side rails which provide the primary structural support. These side rails are heated and act as guard heaters that help to minimize the conduction heat losses from the plates. A removable, insulated, wooden enclosure around the base of the test section reduces heat loss from the metal support rails to the laboratory environment.

The 24 plates which comprise the test surface are each 10.2 cm (4.0 in) in the flow direction by 45.7 cm (18.0 in) in the transverse direction by 0.95 cm (0.375 in) thick. The precision machined test plates are made of electroless nickel plated aluminum. The smooth surface plates used in the baseline tests have a surface finish with centerline average roughness, Ra, measured as less than 0.5 micrometers. The rough wall plates discussed in this report have a centerline average roughness measured as less than 1.6 micrometers on the "smooth" wall portion of the plates. The plates are assembled using dowels to form a continuous and smooth test surface as shown in Figure 3. The allowable step (or mismatch) at the joint between two plates is 0.013 cm.

Each plate is instrumented with two thermistors for temperature measurement, and each has its own motor-driven variable voltage transformer/plate heater circuit which is controlled by the ADACS. A flexible resistance heating pad (plate heater) affixed to the bottom of each plate provides a uniform heat flux to the lower plate surface. The plate heaters, which were custom manufactured by Watlow Electric Manufacturing Co., are about one mm thick and are made of resistance wire spiraled around a glass cord sandwiched between two pieces of glass fabric coated with silicone rubber.

All heater circuits are supplied electrical power through the same Powermark-75110 A.C. voltage regulator which is connected to the building service (110 volt) as shown in Figure 4. Fine adjustment of the plate heater power is accomplished with a Powerstat-15M21 motor driven variable transformer in each heater circuit. These motor driven transformers are grouped in banks of 8, which are supplied power through 1 of 3 manually set Variac-W10 variable transformers used for gross step-down of the regulated power. Experience in acquiring the heat transfer data has shown that plate temperatures can be held within ±0.1 C of a prescribed constant temperature boundary condition along the entire test section.

2.4 COOLING WATER SYSTEM

The cooling water system maintains the test air at a constant temperature by extracting energy added by the heated plates and blower. Cool water from a 568 liter water storage tank is moved by a 186 watt (1/4 hp) Bell & Gossett Model 1522 pump through 5 cm pvc piping to a Trane air/water heat exchanger. The heat exchanger has 4 rows (in the flow direction) of finned cooling coils with a 84 cm by 112 cm (33 in by 48 in) area normal to the flow. Heat from the test air is transferred to the cooling water via the cooling coils before the air enters the nozzle and then the test section. Proportional amounts of warmer water returning from the cooling coils to the storage tank can be dumped into a floor drain through a 1.9 cm motorized ball valve, GF-Type 105. This ball valve may be adjusted and controlled manually or by the ADACS. Water level in the storage tank is maintained at a desired level with make-up cooling water dispensed through adjustable depth sensing valves fed by the building supply.

2.5 DATA ACQUISITION SYSTEM

A Hewlett-Packard Series 9000 Model-220 microcomputer and a Hewlett-Packard 3054A Automatic Data Acquisition and Control System are used to monitor and control the THTTF. The ADACS includes an HP-3437A high speed system voltmeter, an HP-3456A high resolution digital voltmeter, an HP-3497A data acquisition/control unit and a number of special function plug-in assemblies. A detailed discussion of the ADACS and its use in the THTTF is given by Suryanarayana 1986 [23].

Transducers that monitor the THTTF are wired into the ADACS, which relays the information to the microcomputer. The microcomputer digests the operating condition information, decides on the proper response based on programming, and sends commands for the proper controller response to the ADACS. The ADACS can control the rail heaters, plate heaters, cooling system dump valve, and blower motor in response to instructions from the microcomputer. When the THTTF has been brought to the desired equilibrium conditions, the computer directs the ADACS to perform the necessary data collection.

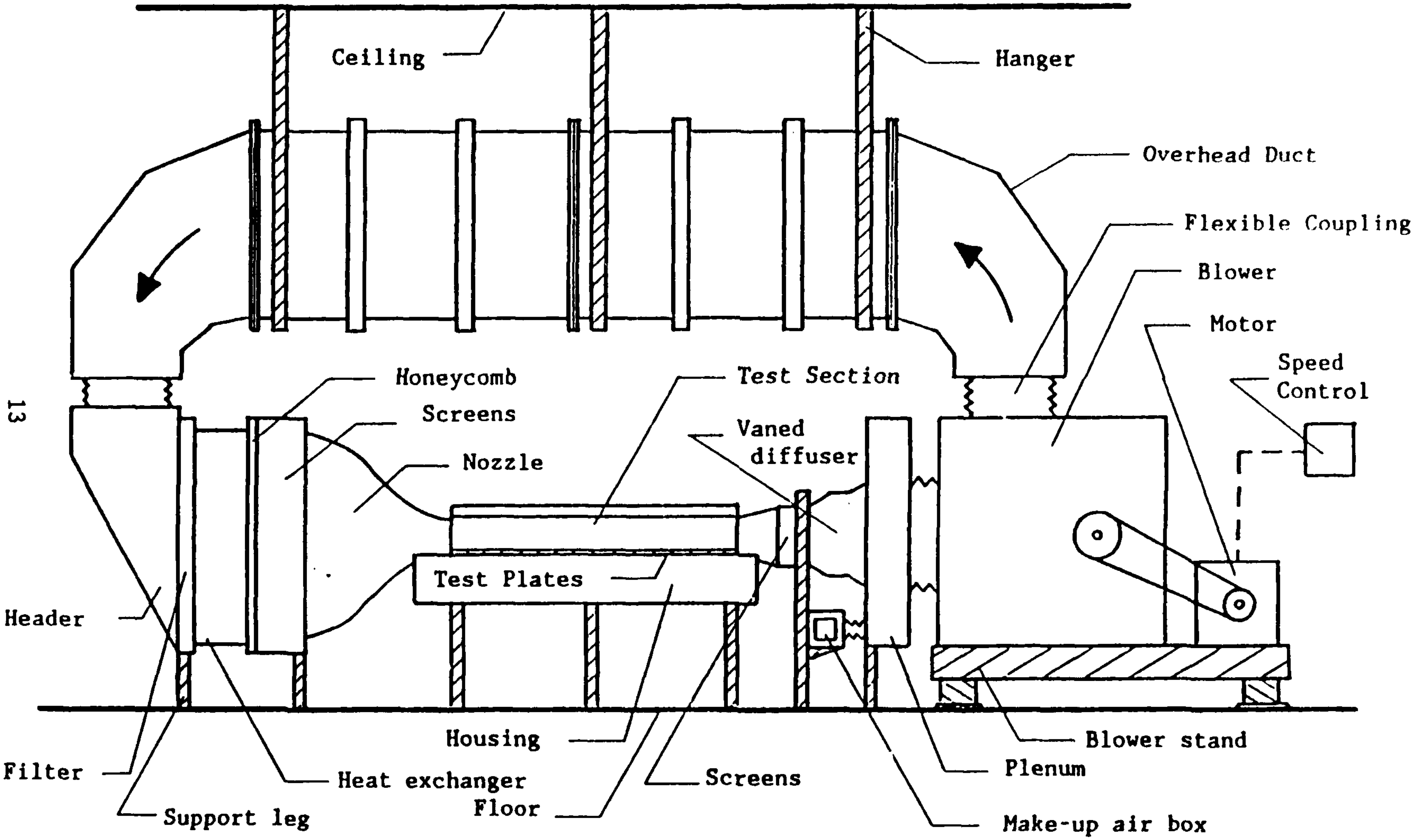
Ceiling
Hanger
Overhead Duct
Flexible Coupling
Blower
Motor
Speed Control
Honeycomb
Screens
Nozzle
Test Section
Vaned diffuser
Test Plates
Header
Housing
Filter
Heat exchanger
Floor
Screens
Support leg
Blower stand
Plenum
Make-up air box

Figure 1. Schematic of the Turbulent Heat Transfer Test Facility (THTTF).

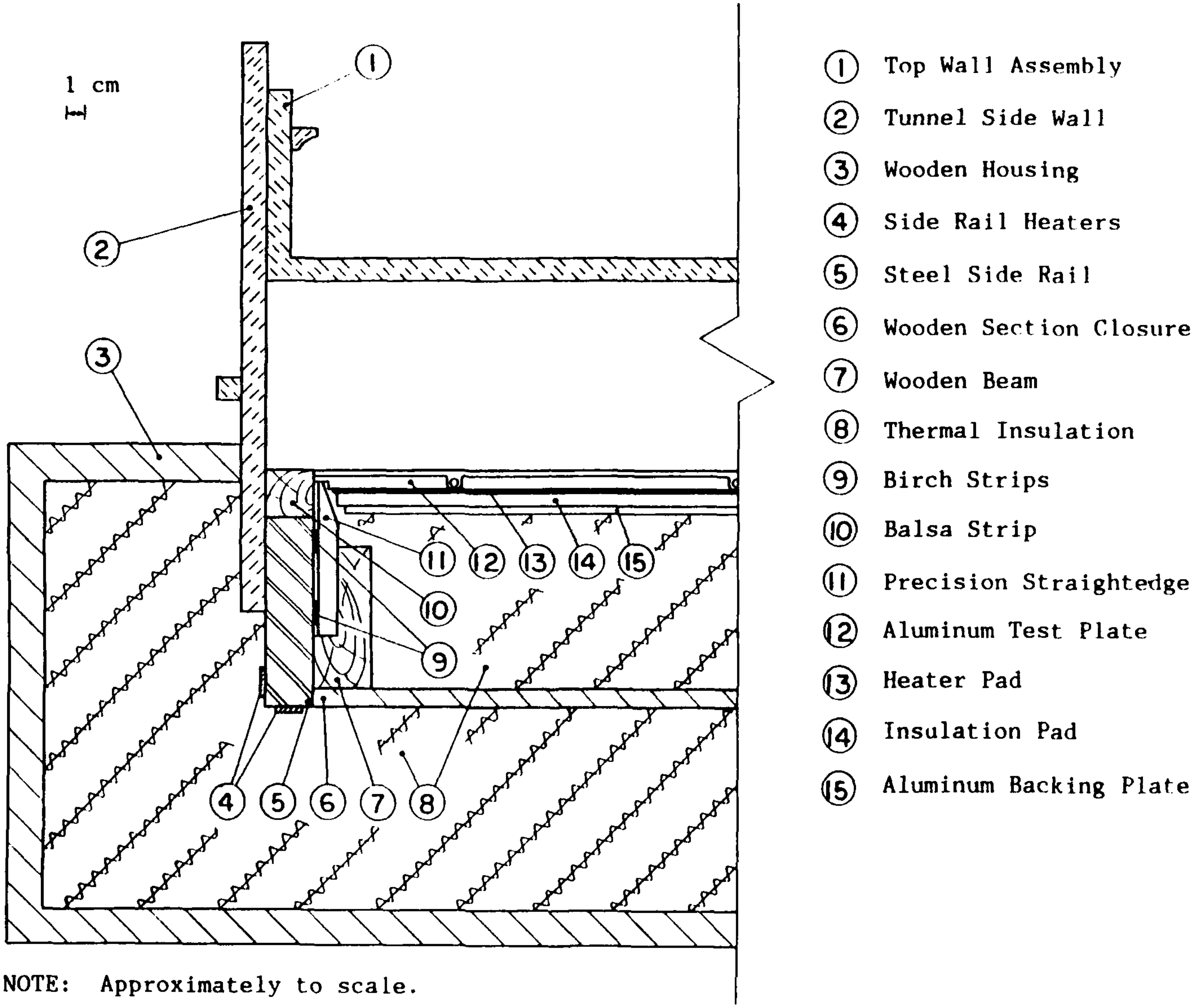
1 cm
①
②
③
④ ⑤ ⑥ ⑦ ⑧
⑨
⑩
⑪ ⑫ ⑬ ⑭ ⑮
① Top Wall Assembly
② Tunnel Side Wall
③ Wooden Housing
④ Side Rail Heaters
⑤ Steel Side Rail
⑥ Wooden Section Closure
⑦ Wooden Beam
⑧ Thermal Insulation
⑨ Birch Strips
⑩ Balsa Strip
⑪ Precision Straightedge
⑫ Aluminum Test Plate
⑬ Heater Pad
⑭ Insulation Pad
⑮ Aluminum Backing Plate

NOTE: Approximately to scale.

Figure 2. Cross Section of the THTTF Test Section.

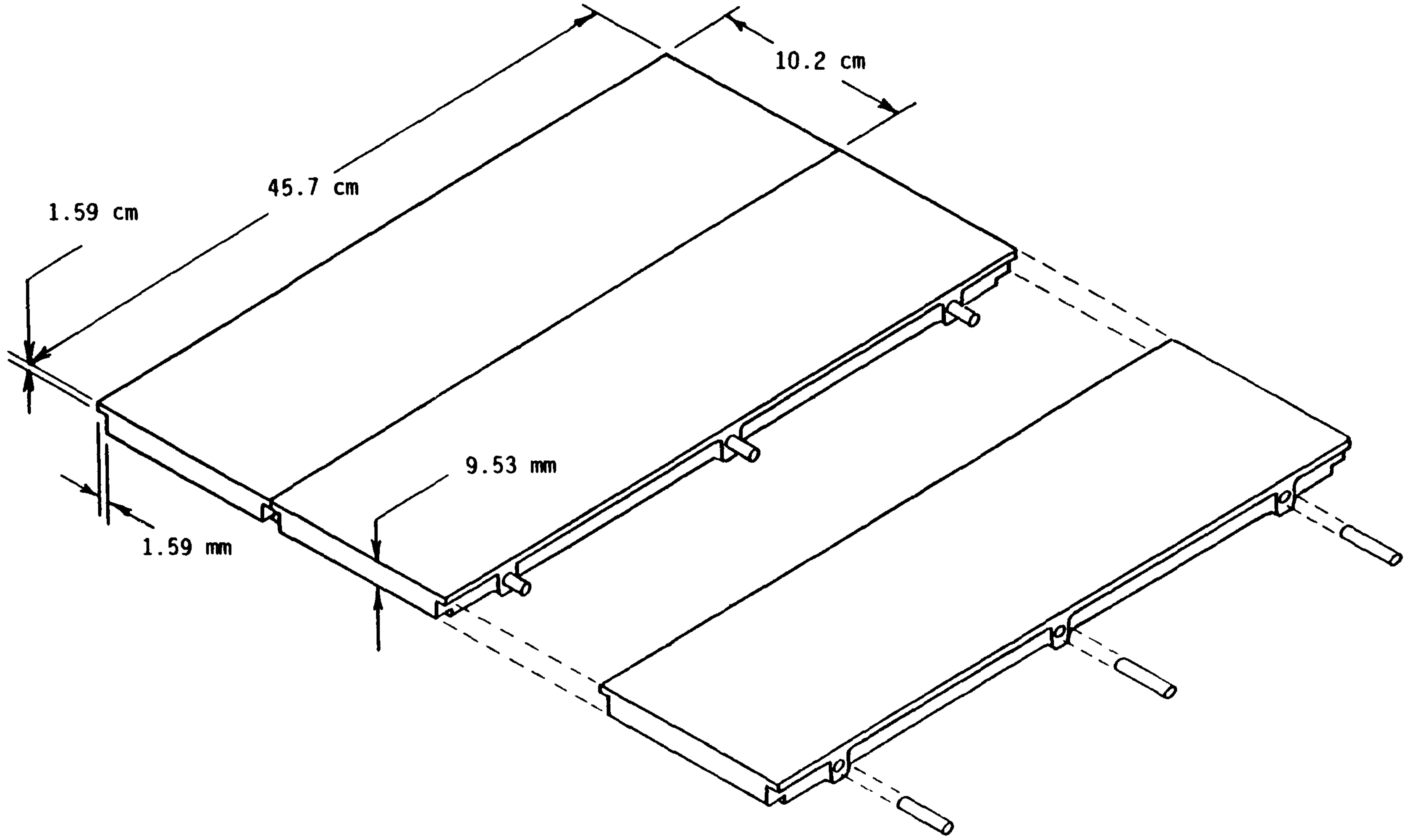
45.7 cm
10.2 cm
1.59 cm
9.53 mm
1.59 mm

Figure 3. Test Surface Assembly.

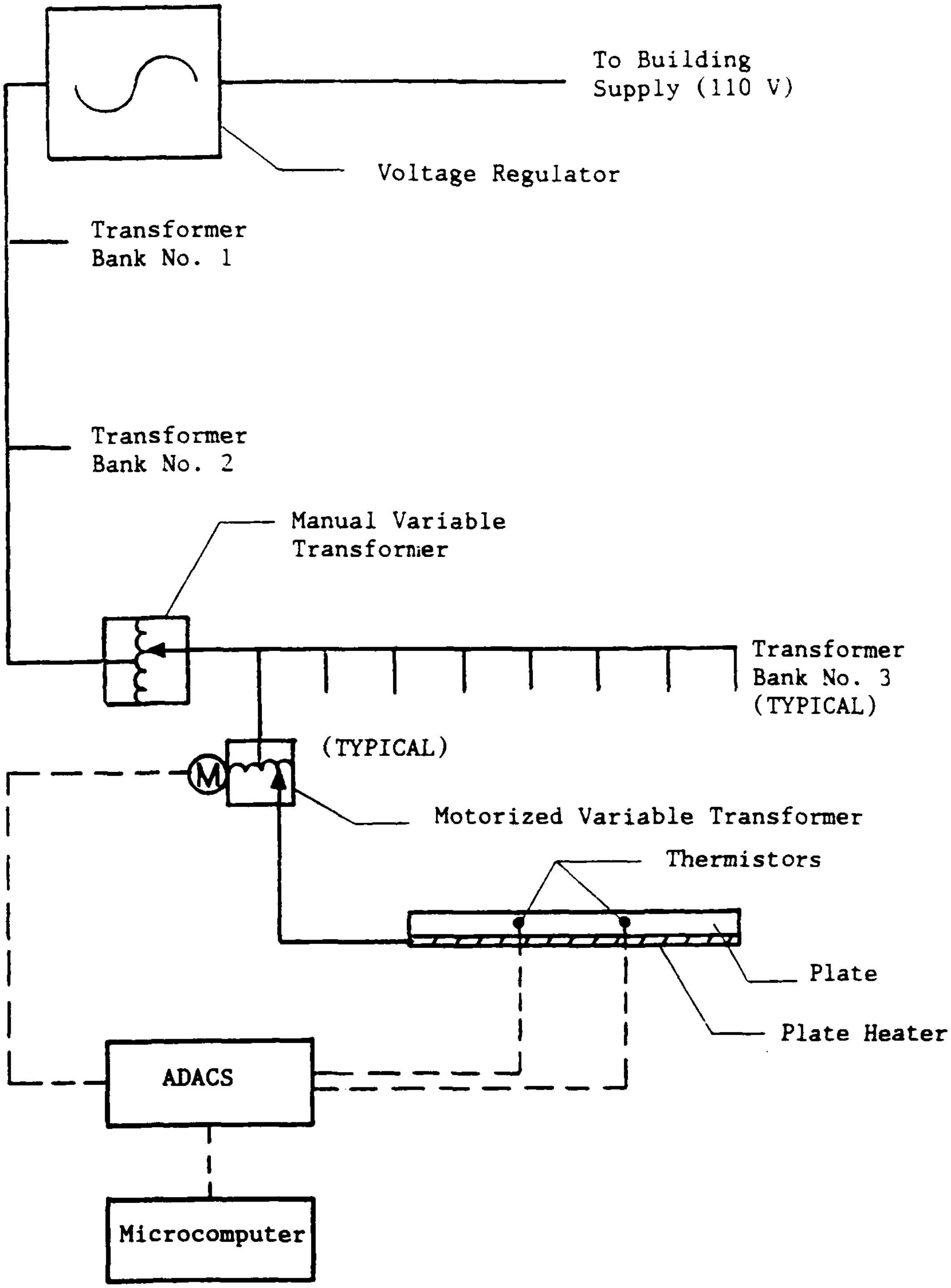
To Building
Supply (110 V)
Voltage Regulator
Transformer
Bank No. 1
Transformer
Bank No. 2
Manual Variable
Transformer
Transformer
Bank No. 3
(TYPICAL)
(TYPICAL)
M
Motorized Variable Transformer
Thermistors
Plate
Plate Heater
ADACS
Microcomputer

Figure 4. Schematic of the Plate Heater Power Circuit and Control Loop.

SECTION 3

SMOOTH WALL QUALIFICATION: FLUID DYNAMICS

The Turbulent Heat Transfer Test Facility (THTTF) was designed to provide quality heat transfer data primarily for zero pressure gradient, constant wall temperature, incompressible flow over flat plates with various surface roughnesses. To produce quality convective heat transfer data, the THTTF must produce flows with properties within acceptable fluid dynamics bounds, and the techniques used in collection of the fluid dynamics data must be proven. The discussion in this section is intended to show that the THTTF is operating within acceptable fluid dynamics bounds and to document the validity of the instrumentation, data collection and data reduction procedures. This objective is met by comparing the smooth wall data obtained in the THTTF with previously published, well-accepted smooth wall results of others. All comparisons in this section are for zero pressure gradient, incompressible, isothermal turbulent boundary layer flow over a smooth surface.

Fluid dynamics variables including profiles of mean velocity and Reynolds stresses and distributions of local skin friction coefficients were determined. A horizontal hot-wire probe and a slanted hot-wire probe were used to measure mean velocity and turbulence quantities as discussed in Appendix II. As discussed in Appendix III, skin friction coefficients were determined from Reynolds shear stress measurements made using hot-wire anemometry and also from Preston tube measurements. In the following, data taken using the THTTF are compared with data obtained on other test facilities which have generated definitive, accepted data.

3.1 FREESTREAM FLOW QUALITY

Pitot tube surveys of the air flow entering the test section were made at the nozzle exit for freestream air velocities of 12 and 28 m/s. The results indicate that the flow is uniform to within about 0.5% of the mean velocity.

As described previously, screens and honeycomb are used immediately downstream of the heat exchanger to suppress turbulent fluctuations in the air flow entering the nozzle. Hot-wire anemometry was used to measure the freestream turbulence intensity with the horizontal wire probe positioned at the test section centerline 4 cm downstream of the nozzle exit. These measurements showed the freestream turbulence intensity to be less than 0.3% for freestream velocities from 61 m/s down to 6 m/s and less than 0.4% at 3 m/s. This compares favorably with freestream turbulence intensities between 2 and 5 percent reported by Reynolds, Kays and Kline 1958 [24], whose smooth wall Stanton number data are considered definitive, for freestream velocities ranging from 14 to 39 m/s. Freestream turbulence intensity of about 0.7% was reported by Moffat 1967 [25], Kearney 1970 [26], and Orlando 1974 [27] for a wind tunnel somewhat similar in design to the THTTF, and Pimenta 1975 [13] reported a value of about 0.4% for the Stanford Roughness Rig which is geometrically similar to the THTTF.

3.2 BOUNDARY LAYER TWO DIMENSIONALITY

The two dimensionality of the flow was investigated by taking velocity profiles with the horizontal hot-wire at transverse stations spaced 5 cm apart over plate 11 (midway down the length of the test section at x = 1.07 m). Boundary layer velocity profile sets were taken at freestream velocities of 12 and 27 m/s. Momentum thicknesses determined from these transversely positioned velocity profiles are shown in Figure 5. The variation in the momentum thicknesses across plate 11 in the transverse direction was less than ±5% about the mean for both velocities. Healzer 1974 [12] reported a variation of the momentum thickness in the transverse direction of less than 3% at a velocity of 27 m/s for the Stanford Roughness Rig.

An additional check on the two dimensionality of the boundary layer was made by measuring the spanwise variation in the skin friction coefficient at plate 11 for a flow velocity of 12 m/s. Skin friction coefficients determined from a Preston tube measuring at positions spaced 0.6 cm (1/4 in) transversely across plate 11 varied by less than 9% peak to peak and less than 5% from the mean. Mehta and Hoffman 1987 [28] reported spanwise variations in local friction coefficients for their tests in two wind tunnels at Imperial College between 8% and 20% peak to peak.

3.3 SKIN FRICTION COEFFICIENT RESULTS

The definitive skin friction coefficient data for zero pressure gradient turbulent boundary layer flows over smooth surfaces are those of Schultz-Grunow 1941 [29]. Schultz-Grunow determined the drag across flat plates in turbulent flows of near zero pressure gradient with a "direct" measurement method, which used a sensitive lever-arm and wire torsion system to measure the drag on a movable plate section. He curvefit his data to get the explicit expression

$$C_f/2 = 0.185(\log_{10}Re_x)^{-2.584} \tag{1}$$

Schultz-Grunow's expression has been shown to match the data of numerous experimenters to within about ±10% and is referenced as definitive by Schlichting 1979 [30] and Kays and Crawford 1980 [31].

Equation (1) is written in terms of the distance from the plate's leading edge (x) for an ideal turbulent boundary layer starting exactly at the leading edge. A flat plate boundary layer that is tripped turbulent acts as if the turbulent boundary layer starts at a fictitious point (virtual origin) upstream of the trip. This virtual origin corresponds to the point where the turbulent boundary layer would begin if it was not preceded by a laminar boundary layer. Therefore, experimental skin friction data from the THTTF, which has a tripped boundary layer, is presented on the basis of a virtual origin when comparing it to the skin friction correlation in terms of x.

The expression used to determine the virtual origin from measured velocity profile data at each profile station is that given by Kays and Crawford as

$$\frac{\delta_2}{xv} = 0.036 \, (Re_{xv})^{-0.2} \tag{2}$$

where xv is the streamwise coordinate measured from the virtual origin. For a given freestream velocity, the "best" virtual origin was obtained by application of a least squares approach to the differences between the momentum thicknesses determined from the measured sets of velocity profiles and the corresponding momentum thicknesses predicted by equation (2) for assumed virtual origins. The virtual origins determined in this manner were 5, 14, and 27 cm upstream of the nozzle exit for freestream velocities of 12, 27, and 43 m/s, respectively. Values of 35 and 43 cm were determined by extrapolation for freestream velocities of 58 and 67 m/s.

Measurements of skin friction coefficient distributions along the test surface were made for $U_\infty = 12$ and 43 m/s using the hot-wire method and $U_\infty = 12$, 27, 43, 58 and 67 m/s using the Preston tube method. Both these techniques are discussed in Appendix III.

Figure 6 shows the local skin friction coefficient distributions in the THTTF determined by hot-wire anemometry compared with the Schultz-Grunow expression with a ±10% range indicated. The scatter in the skin friction coefficient data determined with hot-wire anemometry fall essentially within the ±10% bands about the accepted correlation. This is especially encouraging, since this is the sole technique used in this research program to determine skin friction coefficients in rough surface flows. It also serves as a verification check on the estimated 10 to 12% uncertainty in C_f from the hot-wire method.

Skin friction coefficients determined by the Preston tube method are shown in Figure 7 compared with equation (1) and the ±10% bands. A composite plot of the skin friction data determined by both techniques is given in Figure 8. This figure shows that essentially all of the present data agrees with the well accepted Schultz-Grunow expression within the ±10% band. Therefore, it can be concluded that the local skin friction coefficient data from the THTTF is in substantial agreement with the definitive skin friction correlation and that the facility and measurement techniques are performing correctly for skin friction measurements.

The momentum thickness (δ_2) of a boundary layer accounts for the upstream history of the flow to a considerable degree. Thus, skin friction data from the THTTF are also compared with an accepted skin friction correlation based on the δ_2-Reynolds number. For zero pressure gradient, incompressible flow over smooth flat plates, Kays and Crawford recommend

$$C_f/2 = 0.0125(Re_{\delta_2})^{-0.25} \qquad (3)$$

Figure 9 shows the local skin friction coefficient distributions determined by hot-wire anemometry versus the δ_2-Reynolds number computed from the measured momentum thickness at each profile station and also presents equation (3) with a ±10% range indicated. Skin friction coefficients determined by the Preston tube method are shown versus the δ_2-Reynolds number in Figure 10 along with equation (3) and the ±10% bands. Fewer Preston tube determined skin friction coefficients are shown in Figure 10 than in Figure 7 because Preston tube measurements were made at more locations than were velocity profiles from which momentum thicknesses were determined.

A composite plot of the skin friction data as determined by both methods is given in Figure 11. Inspection of this figure shows that essentially all of the data agrees with equation (3) within a ±10% band. This comparison provides additional confidence in the skin friction measurements.

3.4 BOUNDARY LAYER PROFILE DATA

Boundary layer profiles of mean velocity and turbulence quantities were also measured for comparison with "standard" smooth wall results. Boundary layer mean velocity profiles taken with the horizontal hot-wire over test plate 19 ($x = 1.88$ m) for freestream velocities of 12 and 43 m/s are shown in Figure 12 plotted in u/U_∞ vs y/δ coordinates. These profiles are plotted in Figure 13 in inner region coordinates (u^+ vs y^+) and are compared with the usual smooth surface law of the wall expression

$$u^+ = 2.44 \ln y^+ + 5.0 \tag{4}$$

The friction velocity used in u^+ and y^+ was that determined by the hot-wire method.

Profiles of the axial direction turbulence fluctuations were measured with a horizontal hot-wire at 6 stations spaced 40.6 cm apart along the length of the test section as discussed in Appendix II. These profiles at plates 15, 19, and 23 for $U_\infty = 12$ m/s are shown in Figure 14 in inner region coordinates and are compared with curves representing the axial turbulence data of Klebanoff 1955 [32] and Laufer 1954 [33]. Figure 15 shows the corresponding profiles for $U_\infty = 43$ m/s. The data shown in these two figures collapse fairly well in the inner region and follow the trend of the data of Klebanoff and Laufer.

These same profiles for $U_\infty = 12$ m/s are shown versus y/δ in Figure 16. The data follow the trend of Klebanoff's data, represented by the solid curve. In the outer portion of the boundary layer, the axial turbulence fluctuations in the THTTF are greater than those of Klebanoff since his tunnel had a lower freestream turbulence intensity (0.02% for $U_\infty = 9$ m/s and 0.04% for $U_\infty = 31$ m/s). Corresponding comparisons are shown in Figure 17 for $U_\infty = 43$ m/s. The nondimensional axial turbulence distributions in the THTTF at 12 and 43 m/s are almost identical except in the lower 5% of the boundary layer. The horizontal hot-wire length was greater than 100 wall units (ν/u^*) at the higher freestream velocities. Thus, as discussed by Ligrani and Bradshaw 1987 [34], the hot-wire used in this study was unable to accurately resolve the axial turbulence very near the surface at higher freestream velocities.

The profiles of all three turbulence fluctuating quantities ($(\overline{u'^2})^{1/2}/u^*$, $(\overline{v'^2})^{1/2}/u^*$, $(\overline{w'^2})^{1/2}/u^*$) were measured at plate 11 for $U_\infty = 12$ m/s by traversing the boundary layer with a horizontal hot-wire probe and a 45° slant hot-wire probe as described in Appendix II. These data are shown in Figure 18 and compared with solid curves representing the data of Klebanoff. The profile of the Reynolds shear stress at the same position and conditions is shown in Figure 19 and compared with a solid curve which represents the Reynolds shear stress data of Klebanoff. The Reynolds shear stress data taken on the THTTF are in general agreement with the curve representing Klebanoff's data.

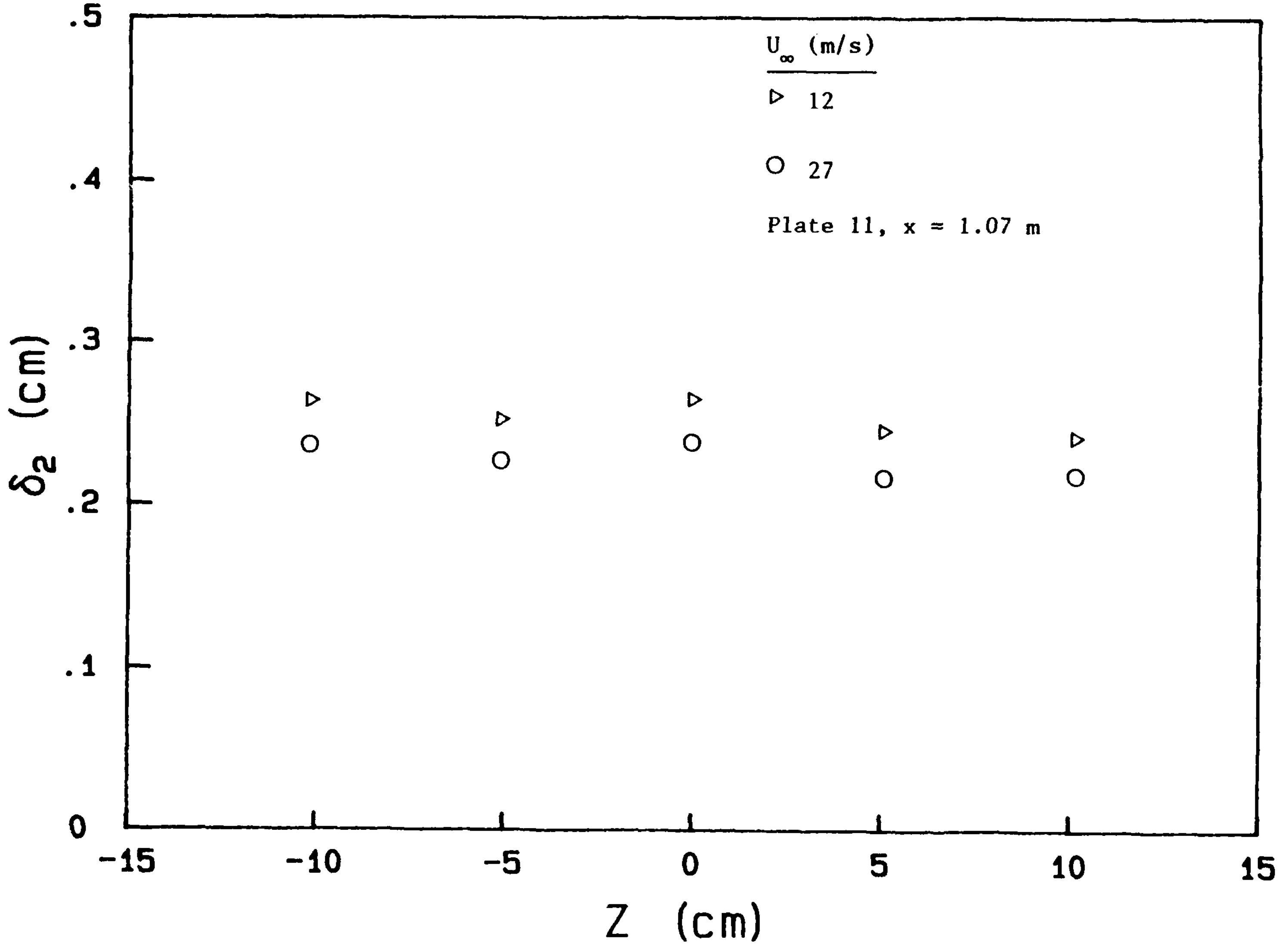

Figure 5. Momentum Thickness Distributions Measured Transversely Across the Tunnel at Plate 11.

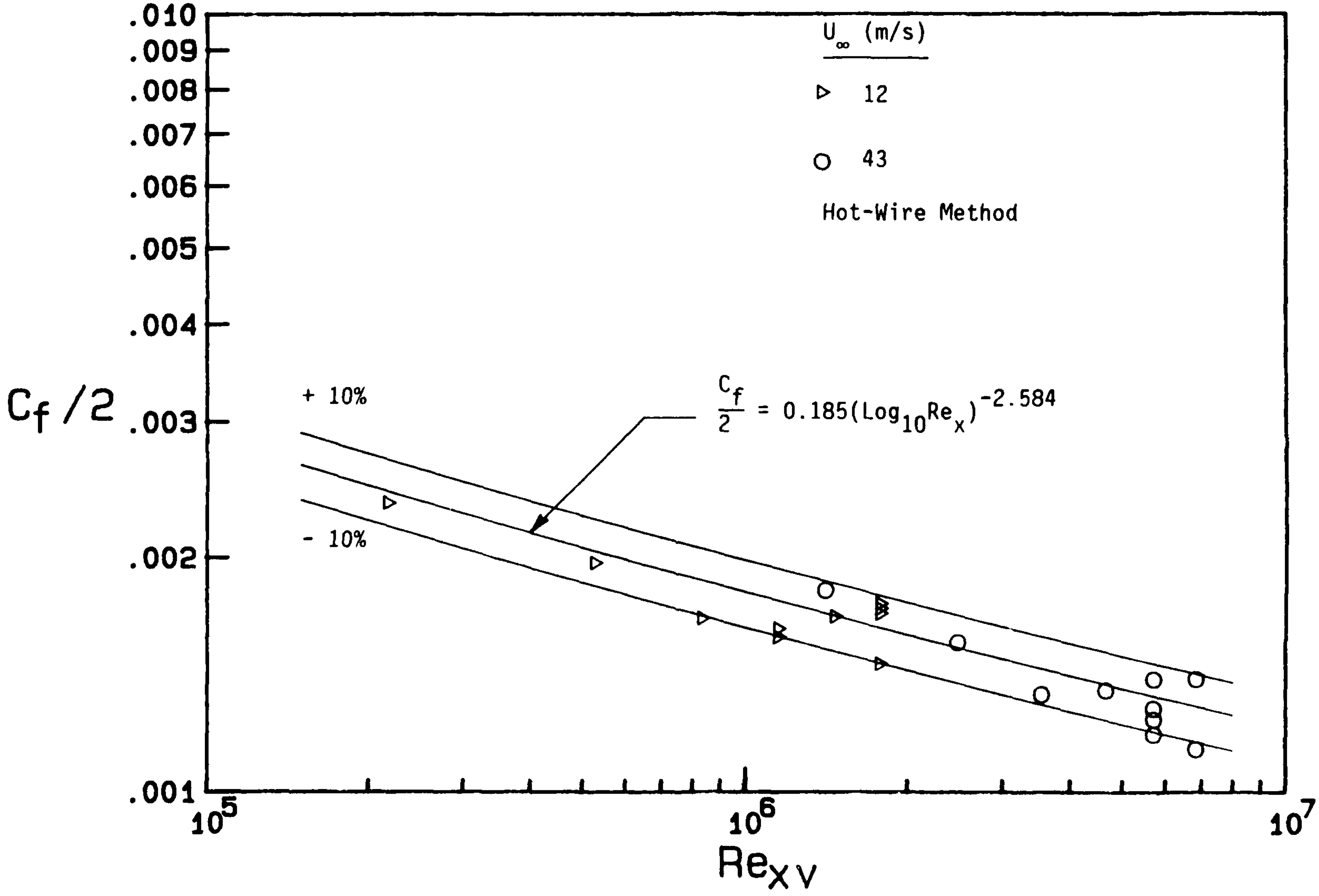

Figure 6. Skin Friction Distribution Determined by the Hot-Wire Method Compared with the Correlation of Schultz-Grunow (1941).

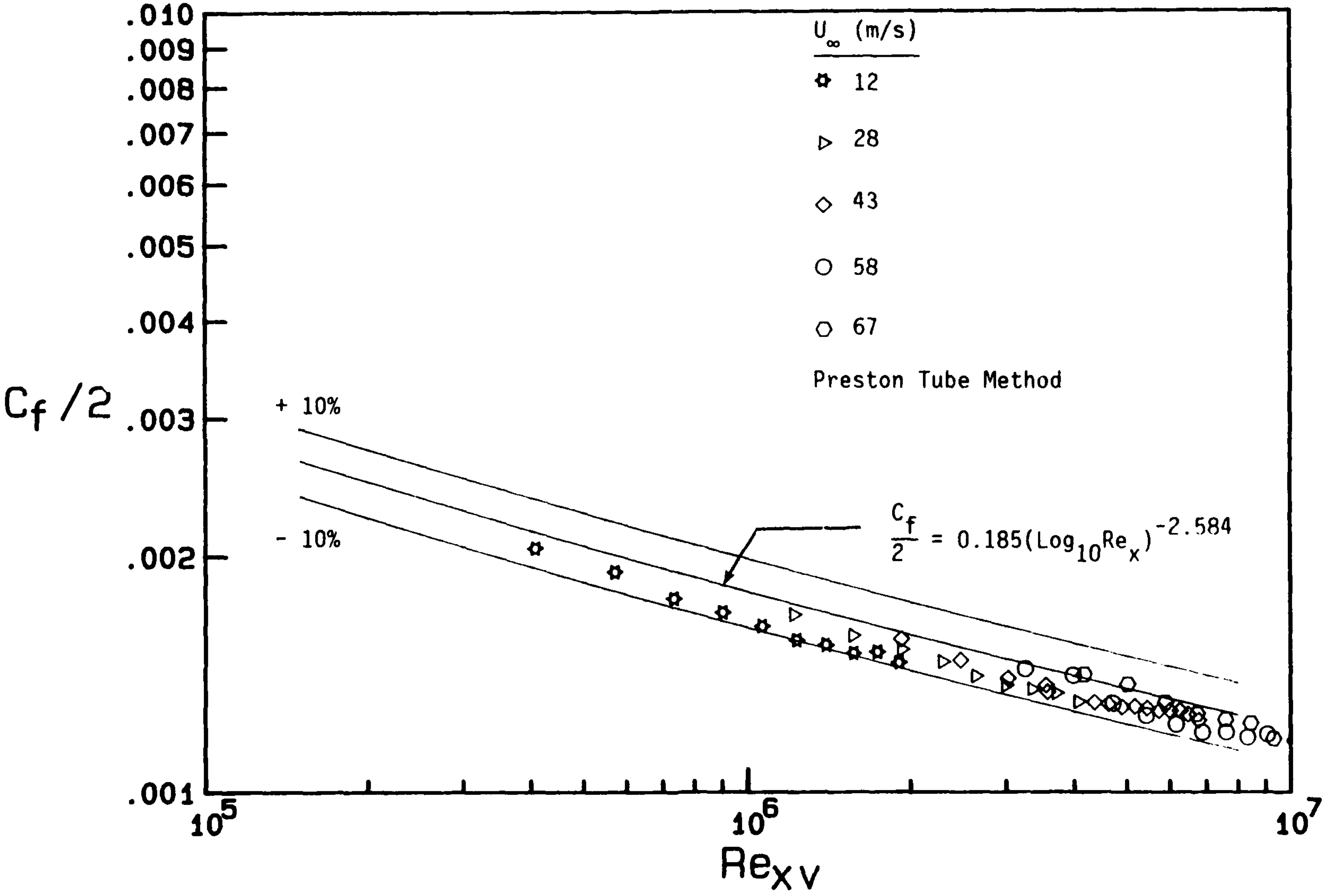

Figure 7. Skin Friction Distribution Determined by the Preston Tube Method Compared with the Correlation of Schultz-Grunow (1941).

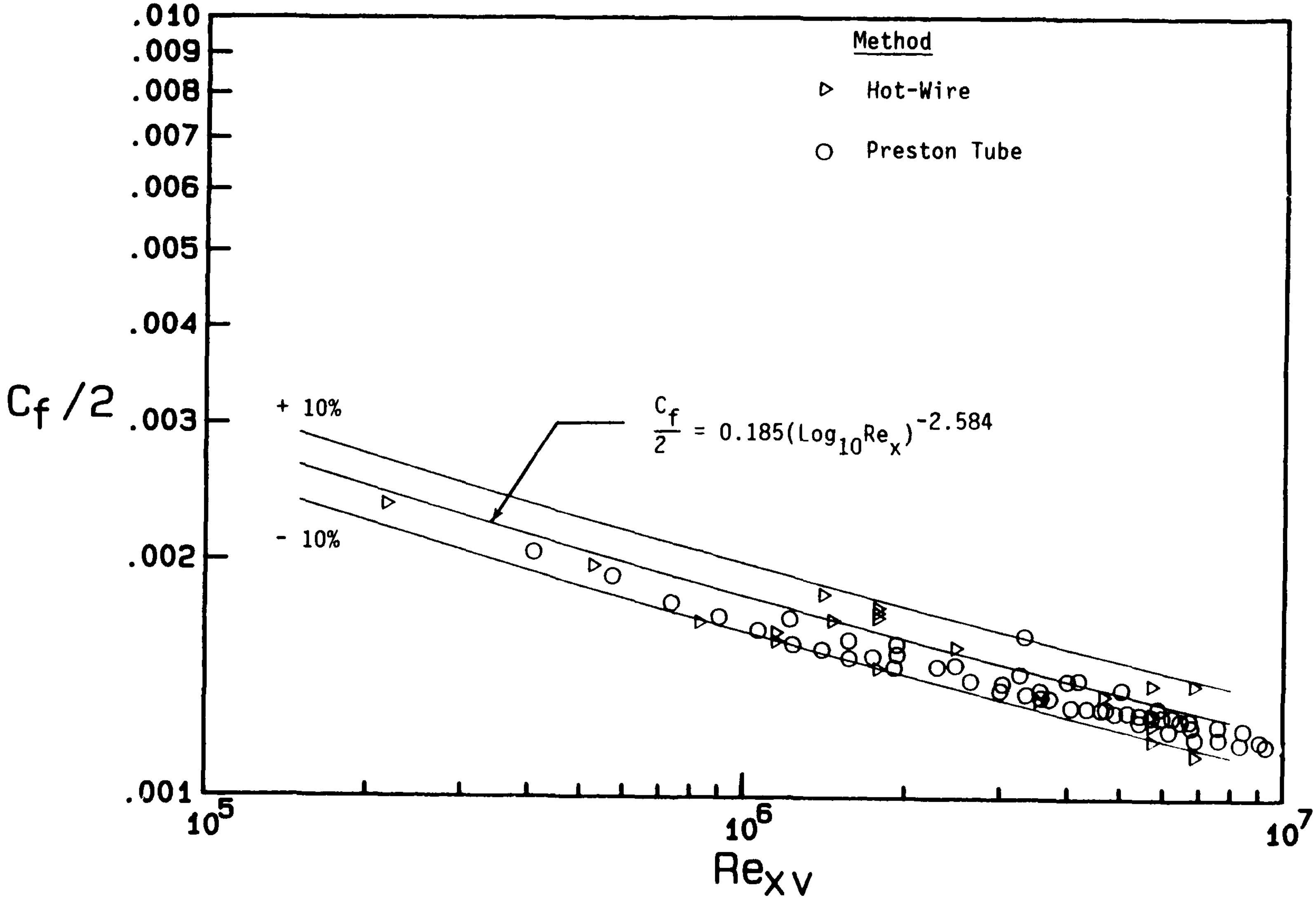

Figure 8. Composite Plot of Skin Friction Coefficient Distributions.

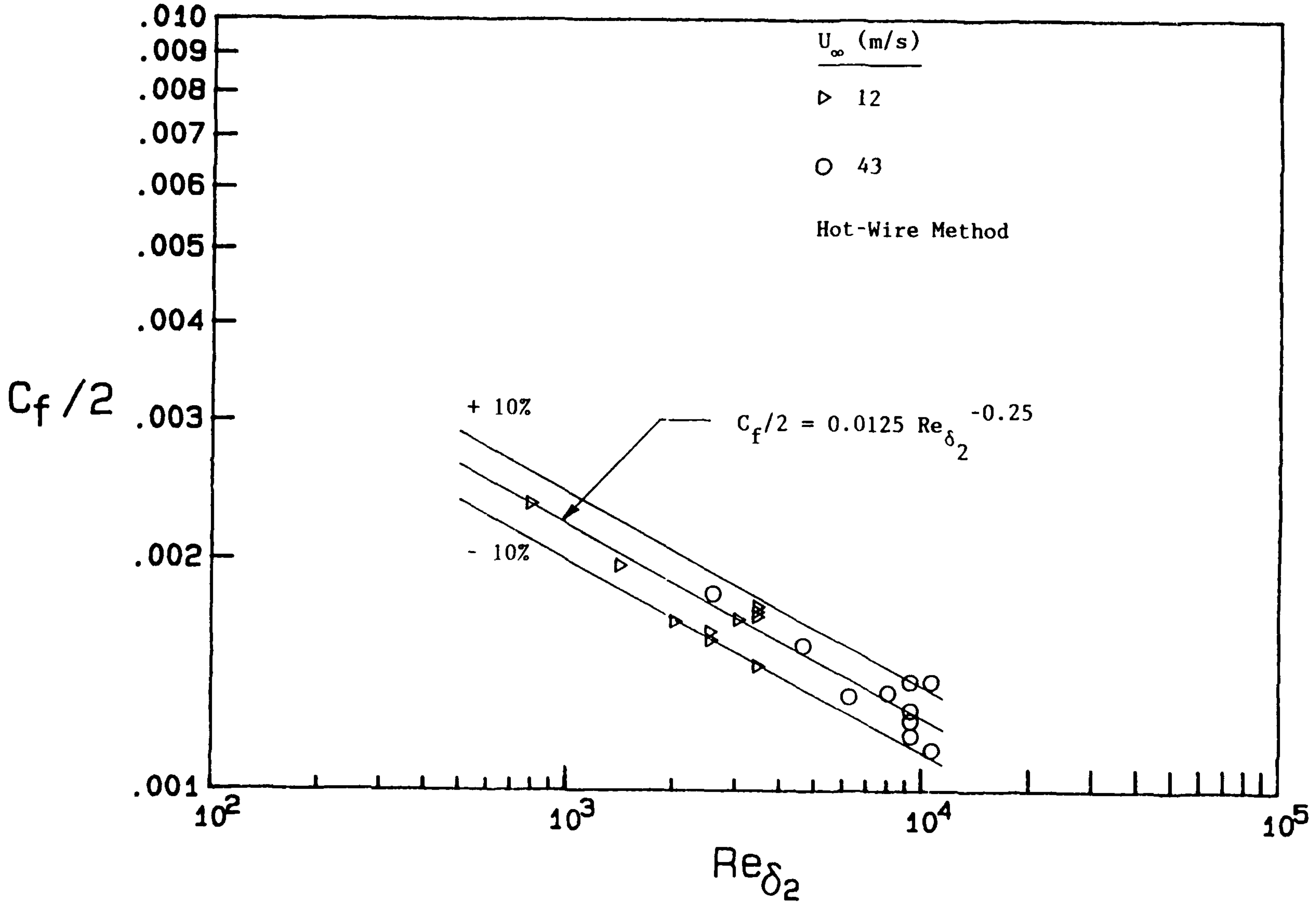

Figure 9. Skin Friction Distribution Determined by the Hot-Wire Method Compared with the Momentum Thickness Reynolds Number Correlation of Kays and Crawford (1980).

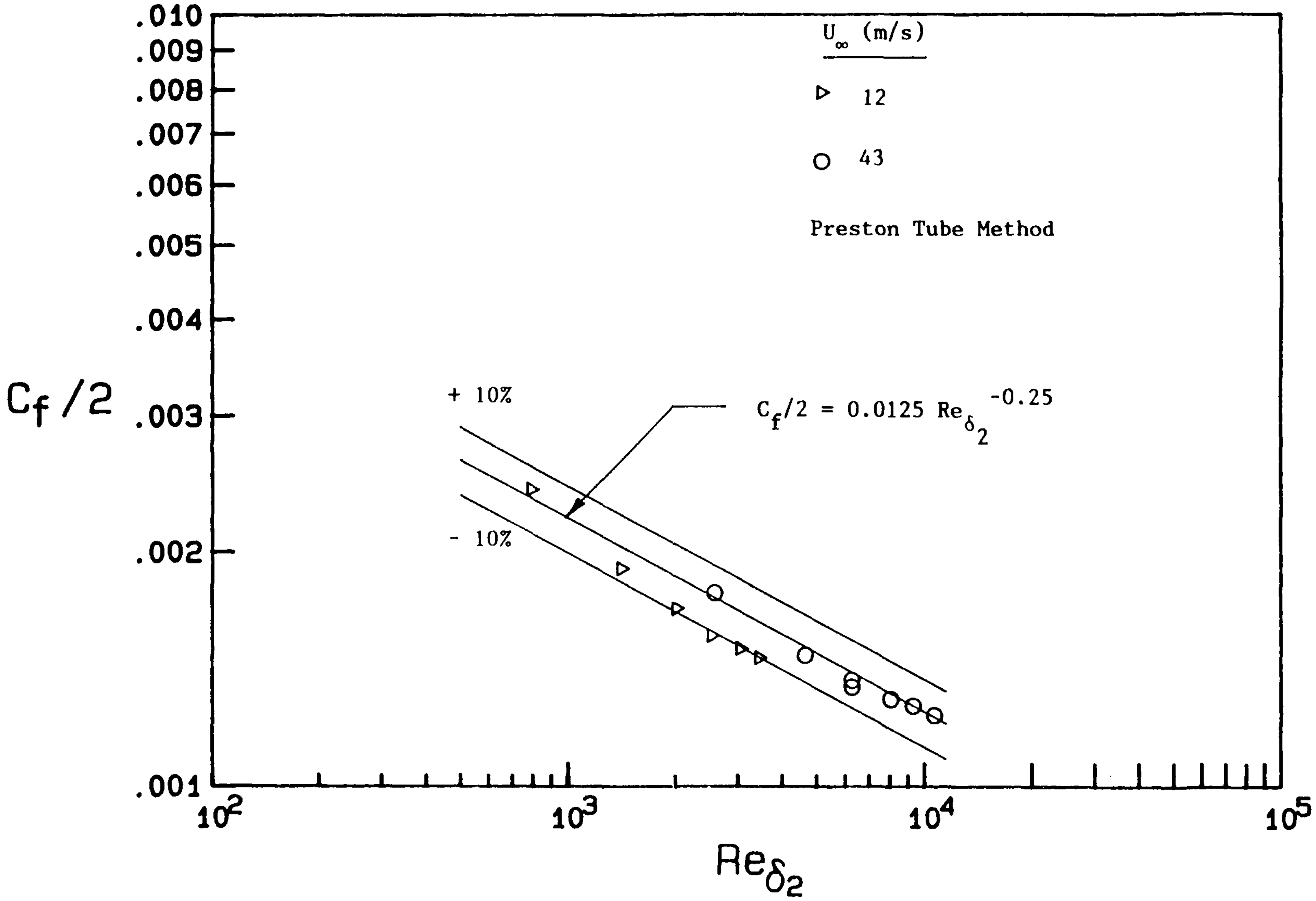

Figure 10. Skin Friction Distribution Determined by the Preston Tube Method Compared with the Momentum Thickness Reynolds Number Correlation of Kays and Crawford (1980).

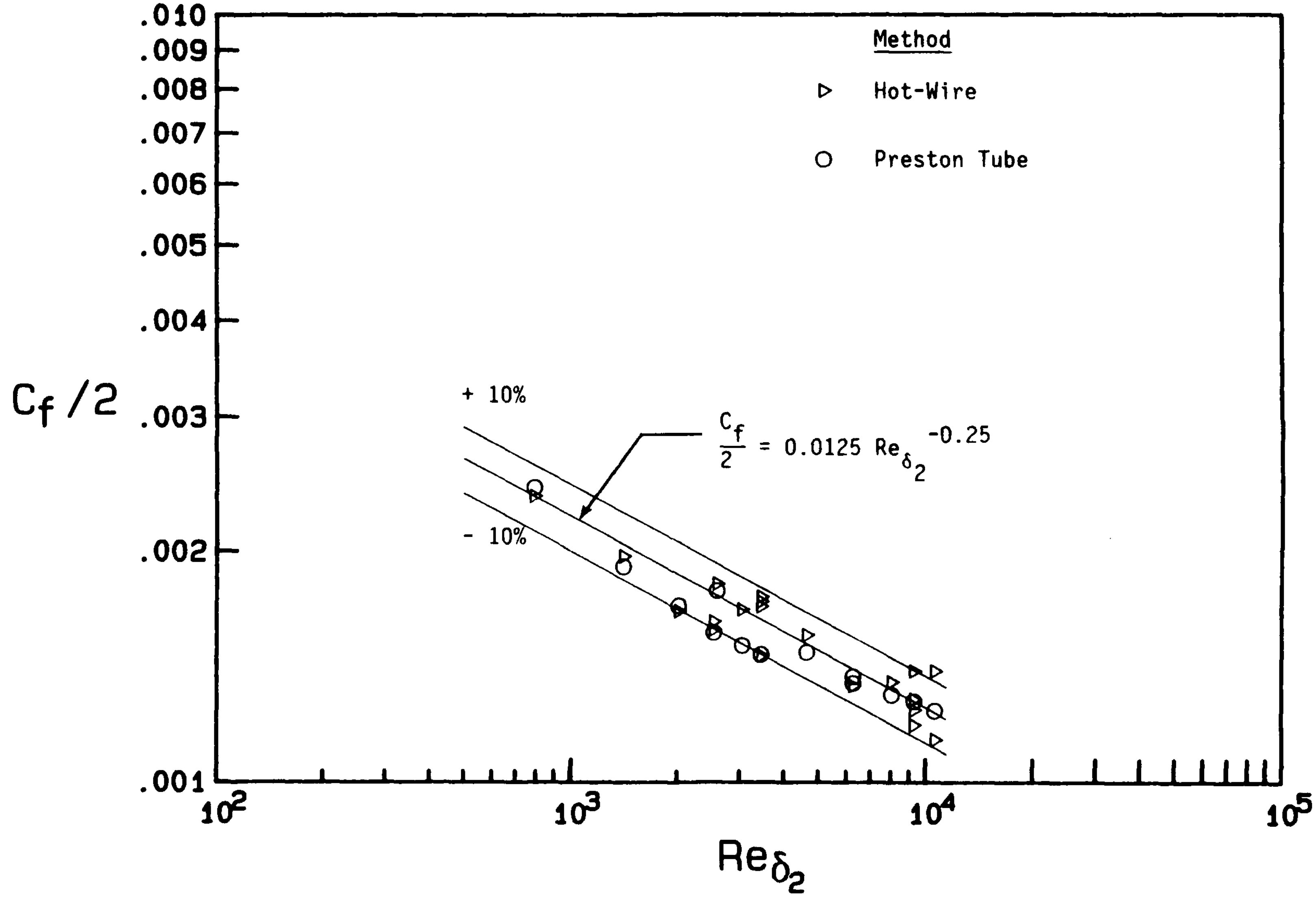

Figure 11. Composite Plot of Skin Friction Coefficient Distributions.

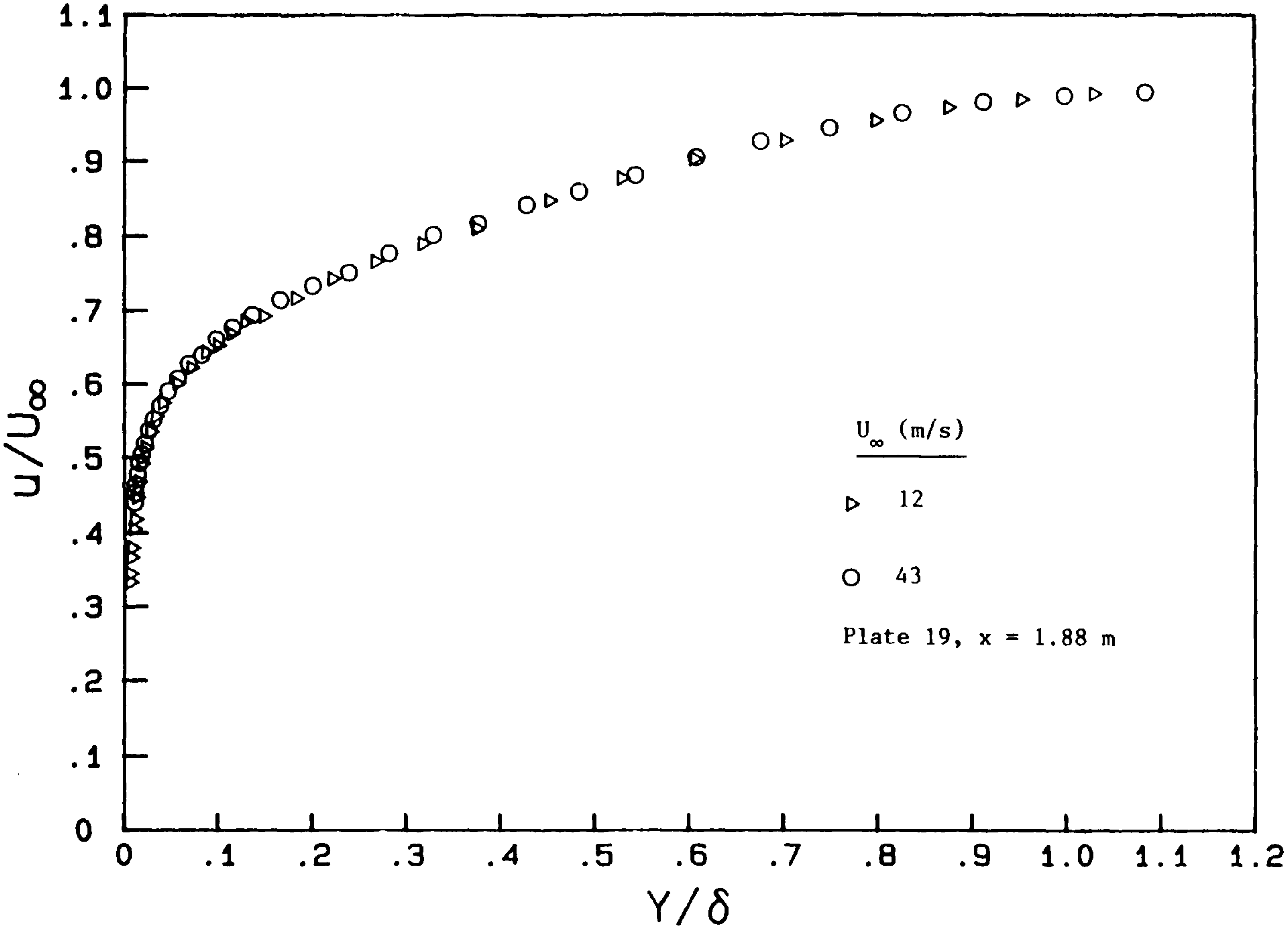

Figure 12. Comparison of Mean Velocity Profiles at Plate 19 for Nominal Freestream Velocities of 12 and 43 m/s.

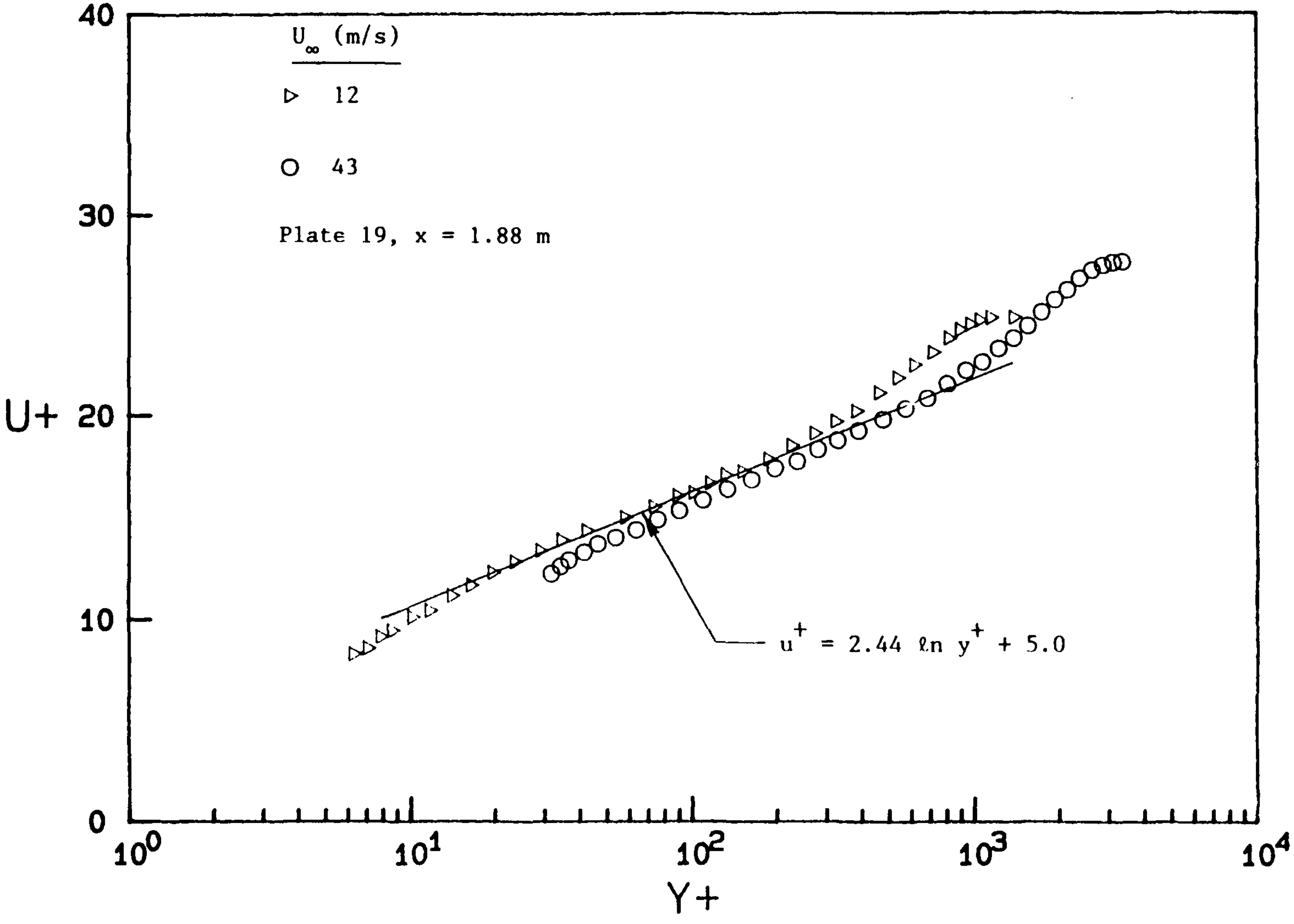

Figure 13. Mean Velocity Profiles at Plate 19 for Freestream Velocities of 12 and 43 m/s Compared with the Law of the Wall.

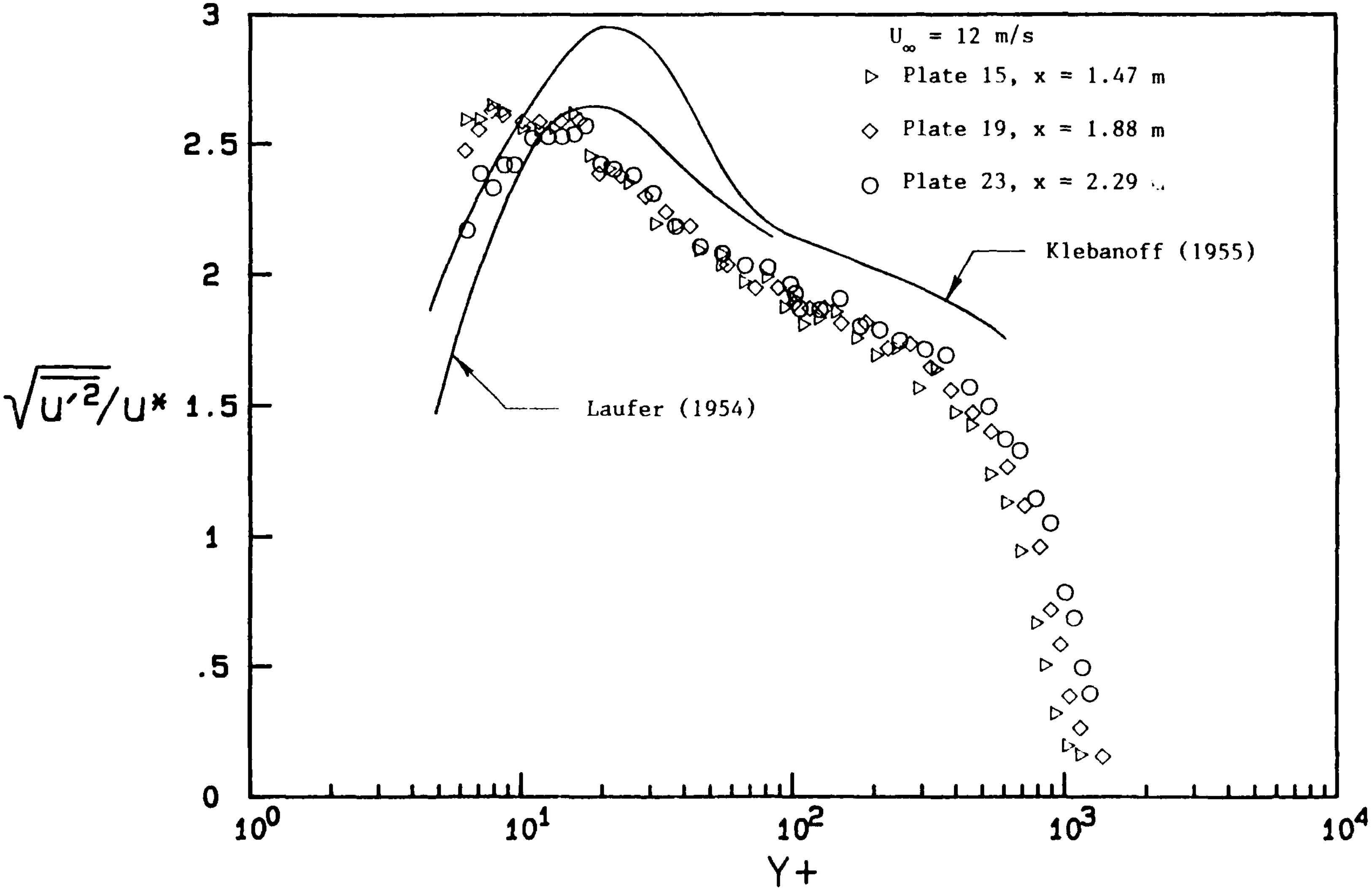

Figure 14. Axial Turbulence Intensity Profiles vs y^+ for a Nominal Freestream Velocity of 12 m/s Compared with the Data of Klebanoff (1955) and Laufer (1954).

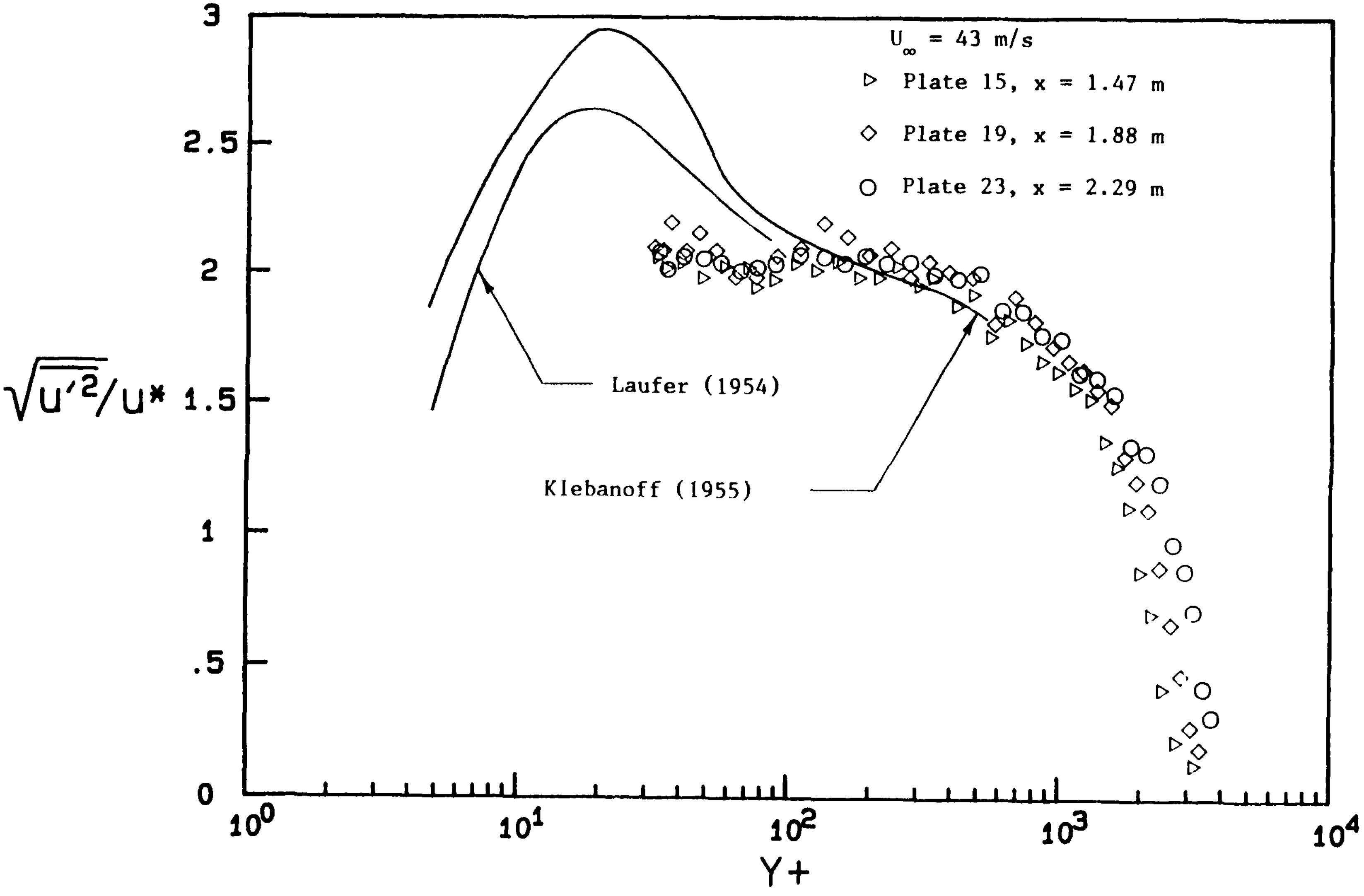

Figure 15. Axial Turbulence Intensity Profiles vs y^+ for a Nominal Freestream Velocity of 43 m/s Compared with the Data of Klebanoff (1955) and Laufer (1954).

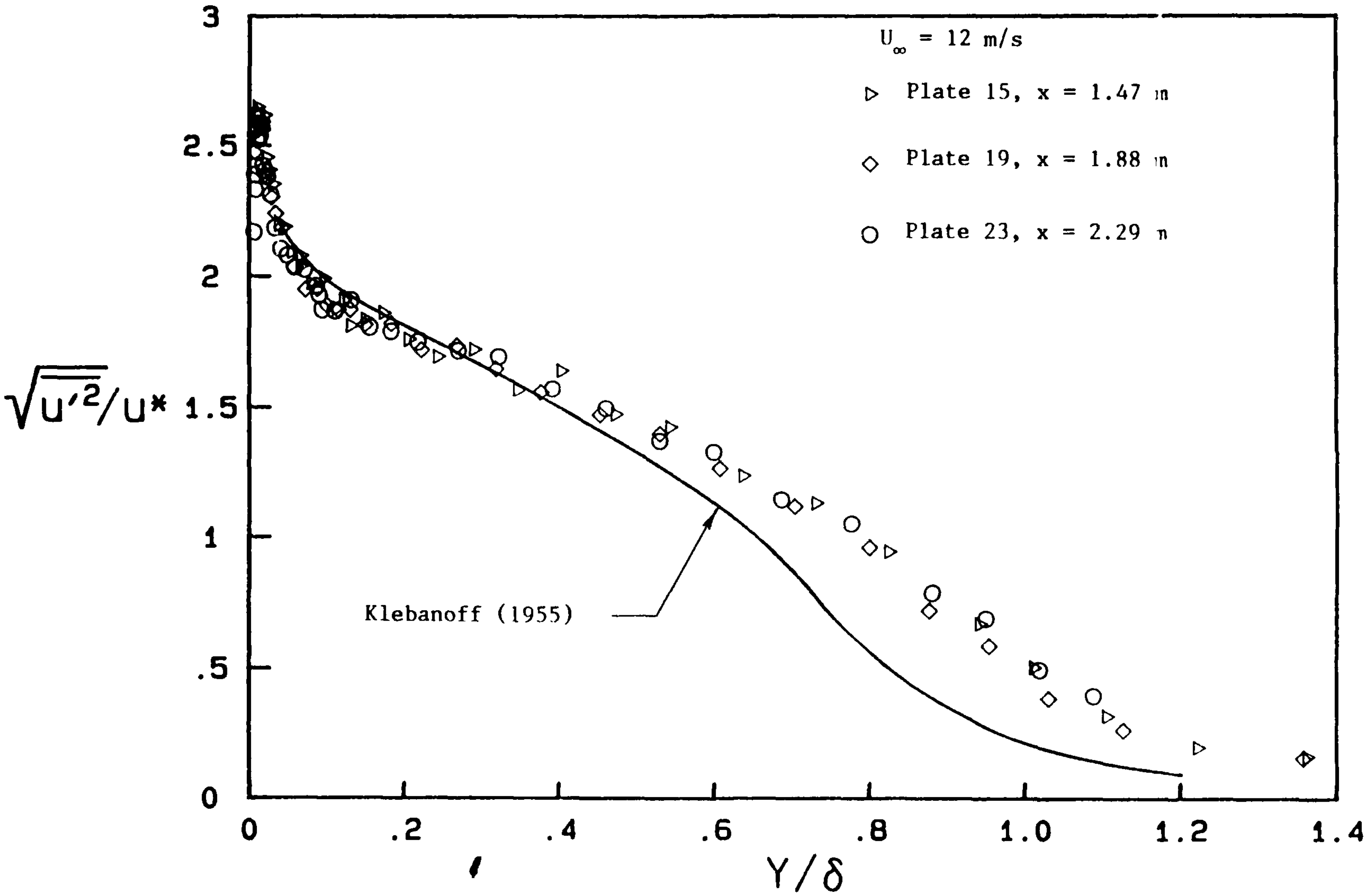

Figure 16. Axial Turbulence Intensity Profiles vs. y/δ for a Nominal Freestream Velocity of 12 m/s Compared with the Data of Klebanoff (1955).

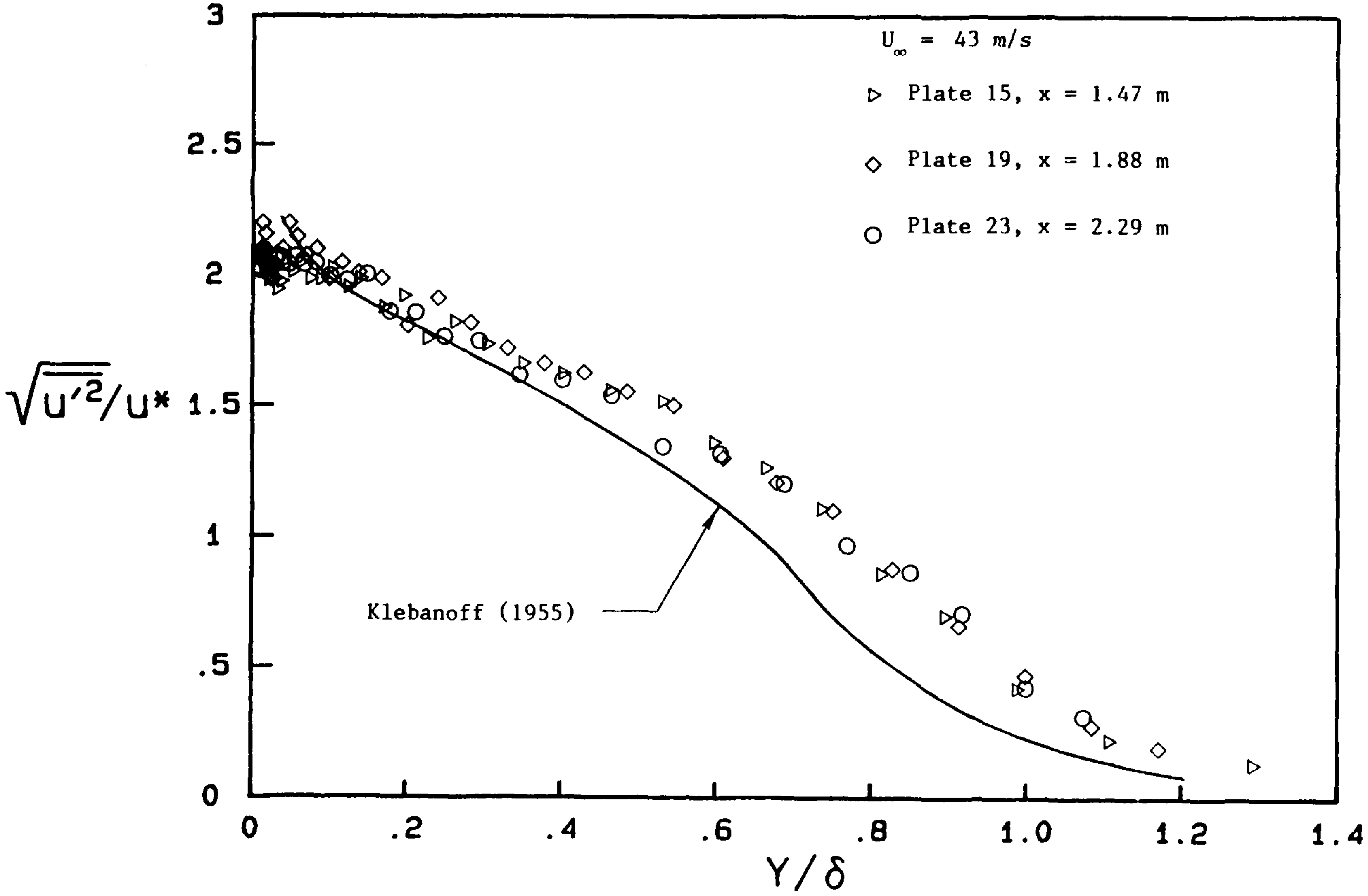

Figure 17. Axial Turbulence Intensity Profiles vs y/δ for a Nominal Freestream Velocity of 43 m/s Compared with the Data of Klebanoff (1955).

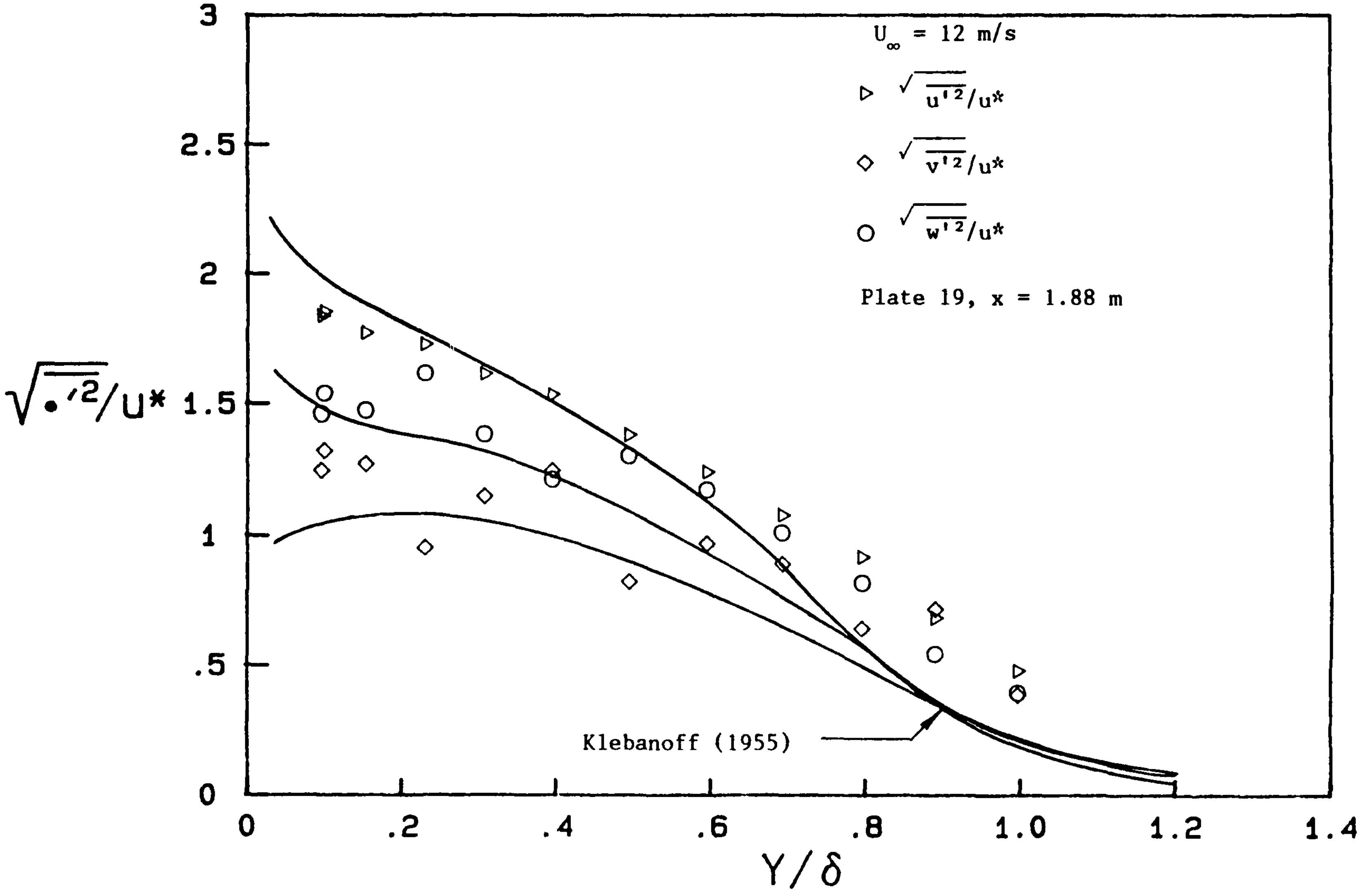

Figure 18. Profiles of All Three Turbulence Intensity Components at Plate 19 for a Nominal Freestream Velocity of 12 m/s Compared with the Data of Klebanoff (1955).

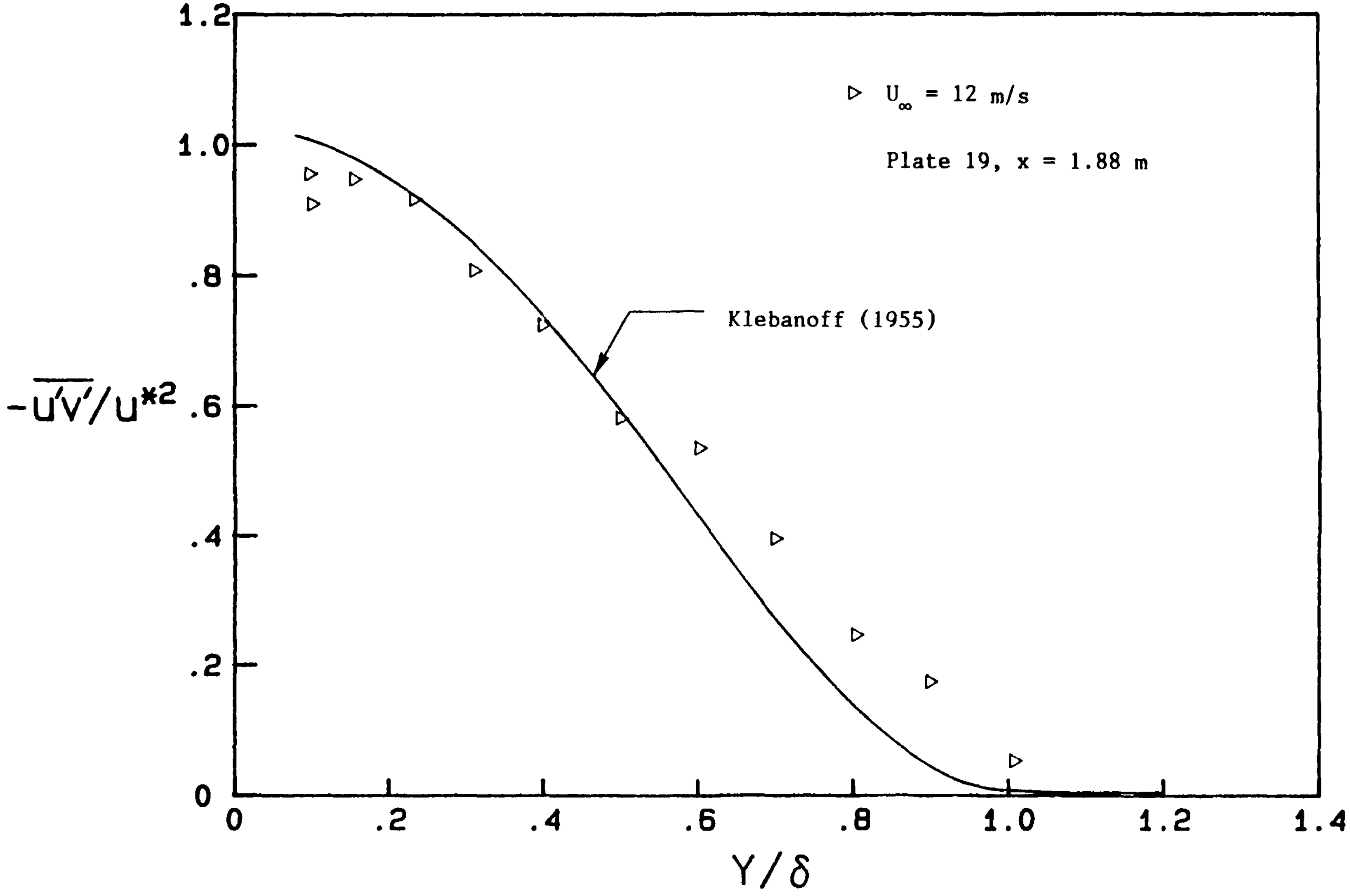

Figure 19. Profile of Reynolds Shear Stress at Plate 19 for a Nominal Freestream Velocity of 12 m/s Compared with the Data of Klebanoff (1955).

SECTION 4

SMOOTH WALL QUALIFICATION: HEAT TRANSFER

The primary objective of this section is to present the smooth wall Stanton number measurements from the THTTF, compare them with previously published data from accepted sources, and verify the fitness of the test rig and the correctness of the instrumentation, data acquisition system and data reduction procedures used in obtaining the Stanton number data and the estimates of its uncertainty. All comparisons and data presented in this section are for zero pressure gradient, constant wall temperature, incompressible boundary layer flow over smooth flat plates.

4.1 STANTON NUMBER RESULTS

Stanton numbers were determined from energy balances on each test plate, as described in detail in Appendix I. The THTTF data are presented using a definition of the Stanton number which is based on the difference between the wall temperature and the freestream total temperature. Other data with which comparisons are made are based on a definition of the Stanton number which uses the difference between the wall temperature and the freestream recovery temperature. This difference in Stanton number definitions is negligible in the comparisons made because the differences in the total and recovery temperatures are numerically insignificant for the range of air velocities considered by the previous experimenters.

The definitive data sets for zero pressure gradient, constant wall temperature, incompressible turbulent boundary layer flow over smooth flat plates are those of Reynolds, Kays and Kline 1958 [24]. In fact, these are the only widely referenced data for the conditions of interest and serve as the basis for all heat transfer correlations for these conditions. They are the only data quoted, for example, by Kays and Crawford 1980 [31] and Rohsenow and Hartnett 1973 [35]. Their experimental apparatus consisted of 24 individually heated copper plates. The plate dimensions were 6.4 cm long in the flow direction by approximately 84 cm wide. This gave a total surface length of 1.5 m. This test surface was placed in a 2.3 m diameter free-jet wind tunnel with freestream turbulence intensity of between 2 and 5 percent, depending on the freestream velocity. Stanton numbers were determined by measuring the power input to each plate, the plate temperatures, and the freestream recovery temperature and correcting for heat losses.

Figure 20 shows a plot of this data (with no variable property correction) along with the correlation

$$St = 0.185(\log_{10}Re_x)^{-2.584}(Pr)^{-0.4} \qquad (5)$$

and ±5 percent bands. A Prandtl number of 0.713 was used in the correlation, which is based on the analogy $StPr^{0.4} = C_f/2$ and uses the Schultz-Grunow expression (equation (1)) for $C_f/2$. Most of the data scatter within the ±5 percent range. These data represent 8 individual runs with freestream velocities ranging from 14 m/s to 39 m/s and with Re_x up to 3.5 million.

Other smooth wall data sets chosen for comparision are from a series of experiments at Stanford University. These data sets are from Moffat 1967 [25], Kearney 1970 [26] and Orlando 1974 [27]. These experiments were mainly concerned with the effects of transpiration on heat transfer in the turbulent boundary layer. Their surface was porous to allow transpiration and had an rms roughness of 5 micrometers, which proved to be aerodynamically smooth at the low velocities used in the experiments. Each of the workers took baseline non-transpired data to qualify the experimental apparatus, and it is this data which is of interest. All of these experiments were conducted on a test facility very similar to the THTTF. The test surface consisted of 24 individually heated plates. Each plate was 10.2 cm long by 45.7 cm wide, resulting in a 2.4 m long test bed. The nominal freestream turbulence was 0.7 percent. Stanton numbers were determined by measuring the plate temperatures and freestream recovery temperature and the power input to each plate and correcting for heat losses. Seven data sets have been selected to represent the early, mid and late time periods of the series. Figure 21 shows a plot of the data along with equation (5) and the ±5 percent bands. Inspection of the figure reveals that the data all scatter within the ±5 percent bands. These data represent freestream velocities from 7 m/s to 13.4 m/s and with Re_x up to about 2 million.

The comparisons in Figures 20 and 21 demonstrate that equation (5) is a reasonable representation of the existing smooth wall, constant temperature, zero pressure gradient Stanton number data and that the data scatter within approximately ±5 percent about this correlation. Therefore, if the THTTF data with their associated uncertainties of about 2 to 5% are within the ±5 percent interval about equation (5), it can be concluded that a successful comparison has been achieved at the Nth order replication level (Moffat 1988 [36], Coleman and Steele 1989 [37]) and that the qualification has been proven.

As discussed in detail in Appendix I, a detailed uncertainty analysis of the determination of Stanton numbers using the THTTF was made during the design and construction phase of the test facility. This analysis showed that the precision limits in the measurements were negligible relative to the bias limits. This meant that replications of Stanton number at a given experimental set point (U_∞) should show negligible scatter, since any significant errors were estimated to be bias errors that would be the same in all replications.

This was found to be the case for runs with $U_\infty = 27, 43, 58$ and 67 m/s as Figures 22-25 illustrate. The Stanton number results for two runs are plotted in each instance, and it is apparent that the estimate of zero precision limit (no scatter) is a reasonable one. Such a conclusion cannot be drawn for the $U_\infty = 12$ m/s condition, however. This is shown in Figure 26, in which the results of eight separate Stanton number runs at $U_\infty = 12$ m/s are shown. The data clearly indicate a run-to-run scatter which cannot be termed negligible.

Investigation showed that at low freestream velocities--$U_\infty \lesssim 12$ m/s for the smooth wall tests and $U_\infty \lesssim 6$ m/s for the rough wall tests--the heat transfer coefficients are relatively low and the time constant of the THTTF is thus increased. At these conditions the time constant of the THTTF is large enough so that the relatively long period variations in facility line voltage to the test plate heater circuits and in the temperature of the incoming make-up water for the heat exchanger loop affect the ability to hold a tight steady state condition. These annoyances could be overcome with additional expenditures for power conditioning equipment and a water chiller system; however, the observed run-to-run scatter in St results is within acceptable limits. Observations of the St results for the nine runs shown in Figure 26 and also three $U_\infty = 6$ m/s runs with a rough wall produced a 95% confidence estimate of a precision limit in St of about 3% for these conditions. This is present because of system unsteadiness and not because of measurement uncertainties. For the $U_\infty = 12$ m/s smooth wall data, therefore, there is a 3% precision limit contribution combined by root-sum-square with the estimated bias limit to obtain the overall uncertainty in St.

Shown in Figure 27 are the St data from one replication at each freestream velocity plotted along with the 95% confidence uncertainty interval for representative data points. These are compared with equation (5) and its ±5% interval, and the comparison shows the excellent agreement which is obtained. The data and the associated uncertainty bands everywhere overlap the correlation with its associated ±5% interval. This comparison validates the qualification of the THTTF for Stanton number measurements.

The present data sets extend to a larger Reynolds number than the previous data ($Re_x = 1 \times 10^7$ versus 3.5×10^6) and over a larger range of freestream velocities. An extensive survey of the literature revealed no flat plate Stanton number data for x-Reynolds numbers above 3.5 million for incompressible flows. In the present work the experimental Stanton number range has been essentially tripled up to x-Reynolds numbers of 10 million. It can be seen that equation (5) represents the data well over the entire range.

4.2 TEMPERATURE PROFILE COMPARISON

Mean temperature profiles were measured by traversing the boundary layer with a thermocouple probe as discussed in Appendix II. The maximum variation in the freestream temperature in the THTTF from any one temperature profile location to any other temperature profile location was less than 0.16°C. Previous studies have shown that temperature profiles along smooth flat plates of constant temperature in a zero pressure gradient, turbulent flow agree with the law of the wall for a thermal boundary layer as given by Kays and Crawford

$$T^+ = 2.195 \ln y^+ + 13.2 \Pr - 5.66 \qquad (6)$$

Figure 28 shows the temperature profiles at plate 19 for $U_\infty = 12$ and 43 m/s plotted in T^+ vs. y^+ coordinates along with equation (6). The data show good agreement with the temperature "law of the wall."

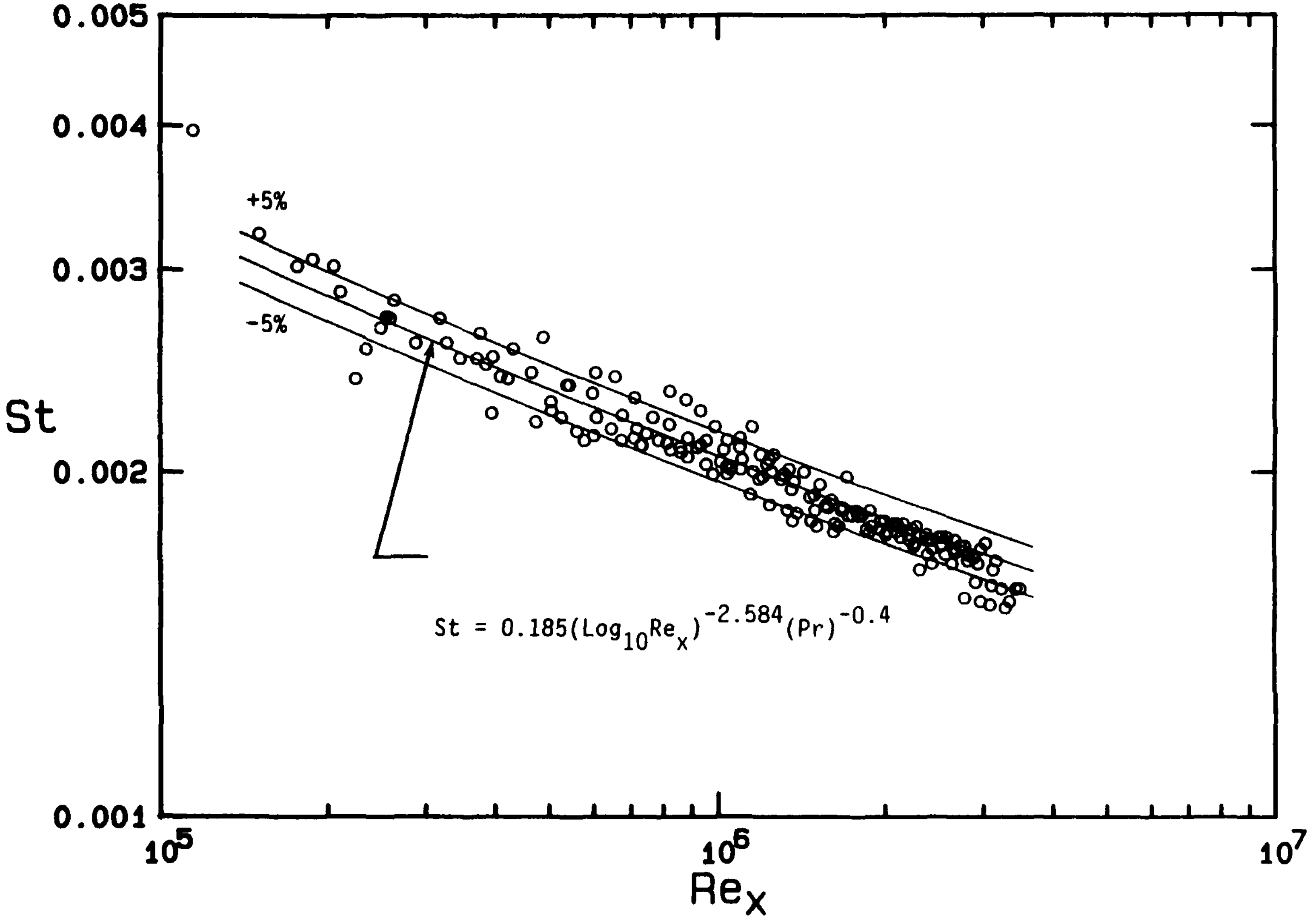

Figure 20. Stanton Number Data of Reynolds, Kays and Kline (1958) Compared with the x-Reynolds Number Correlation (equation (5)).

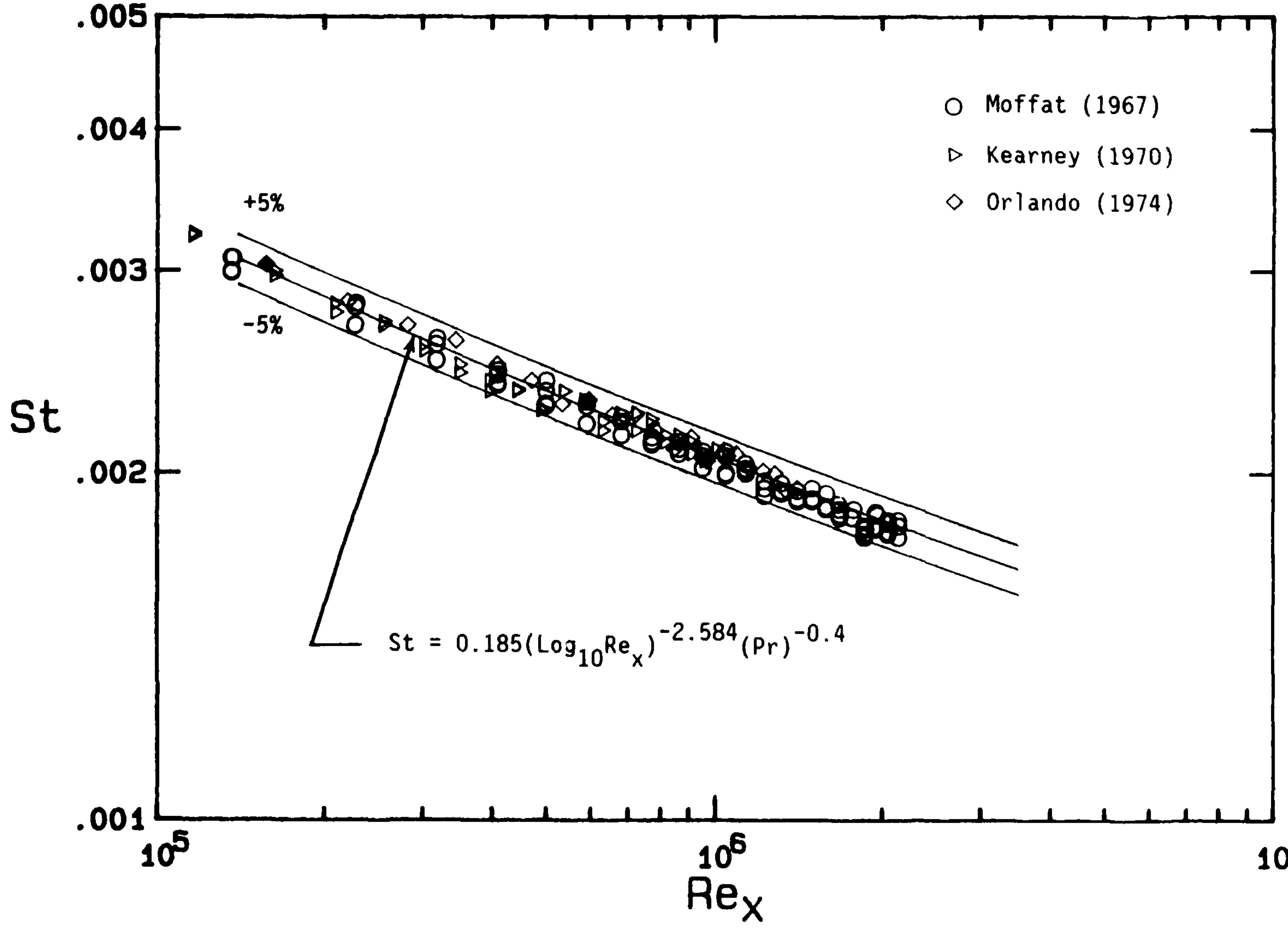

Figure 21. Stanton Number Data of Moffat (1967), Kearney (1970) and Orlando (1974) Compared with the x-Reynolds Number Correlation (equation (5)).

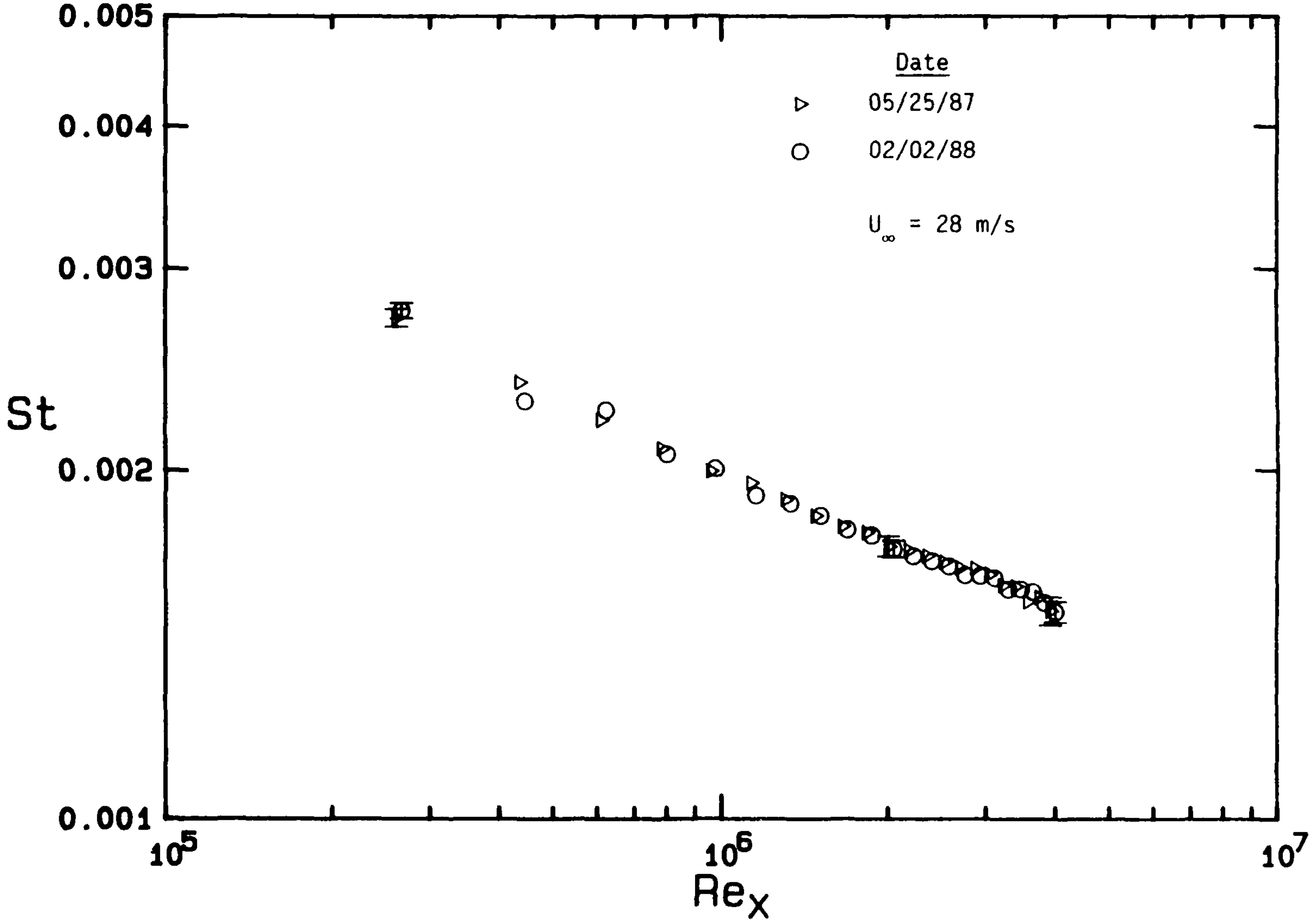

Figure 22. Comparison of Stanton Number Replications for U_∞ = 28 m/s.

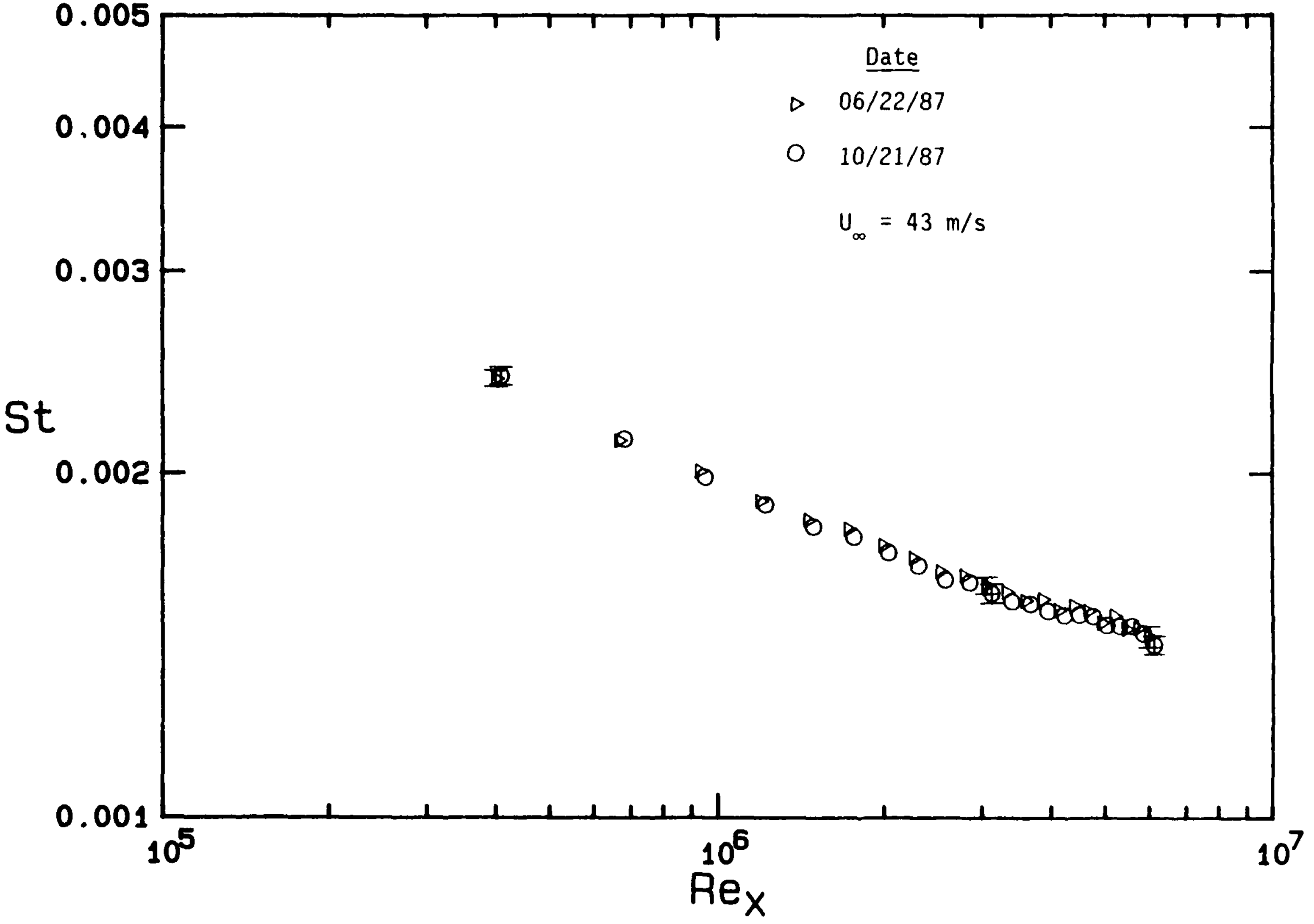

Figure 23. Comparison of Stanton Number Replications for U_∞ = 43 m/s.

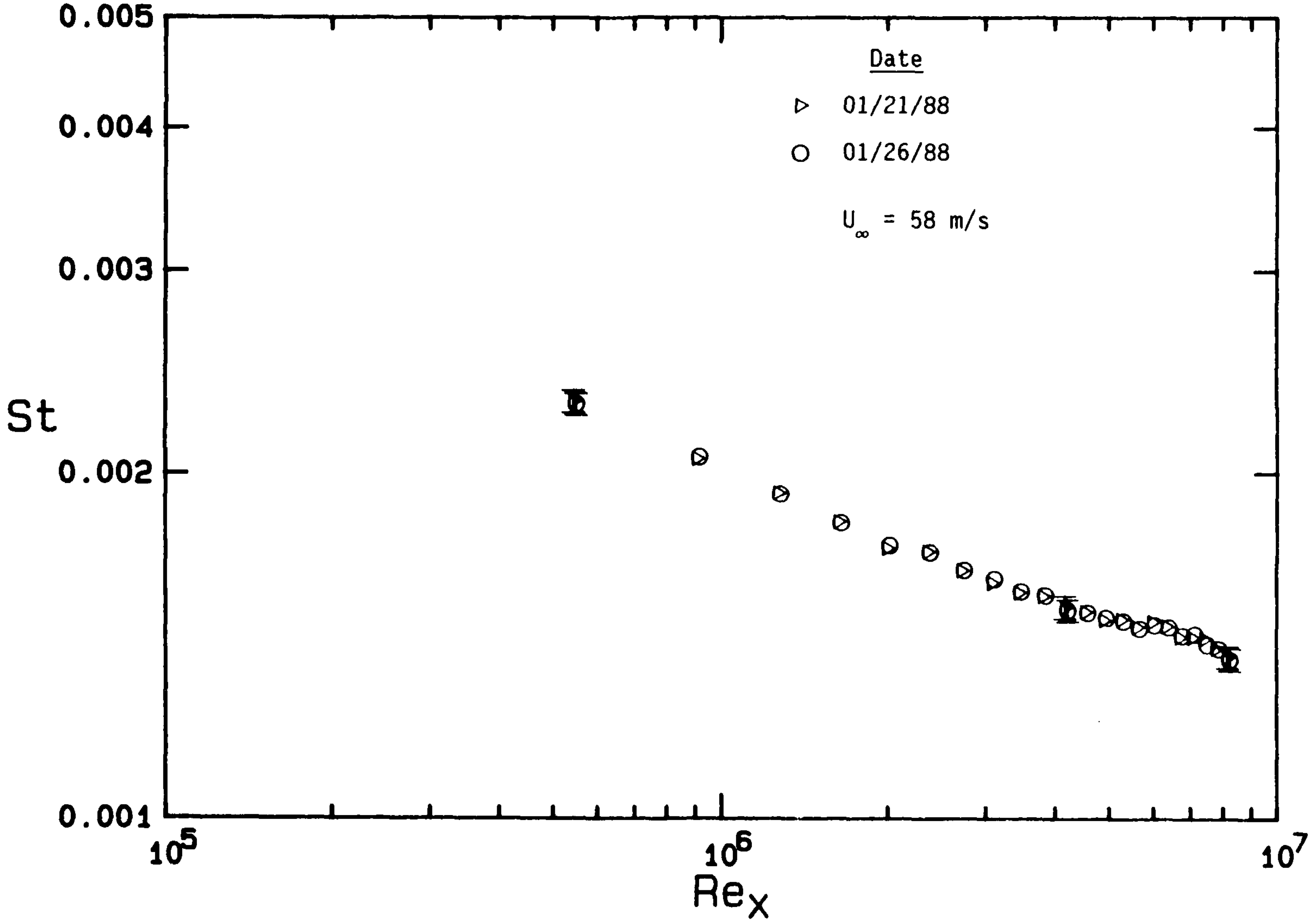

Figure 24. Comparison of Stanton Number Replications for U_∞ = 58 m/s

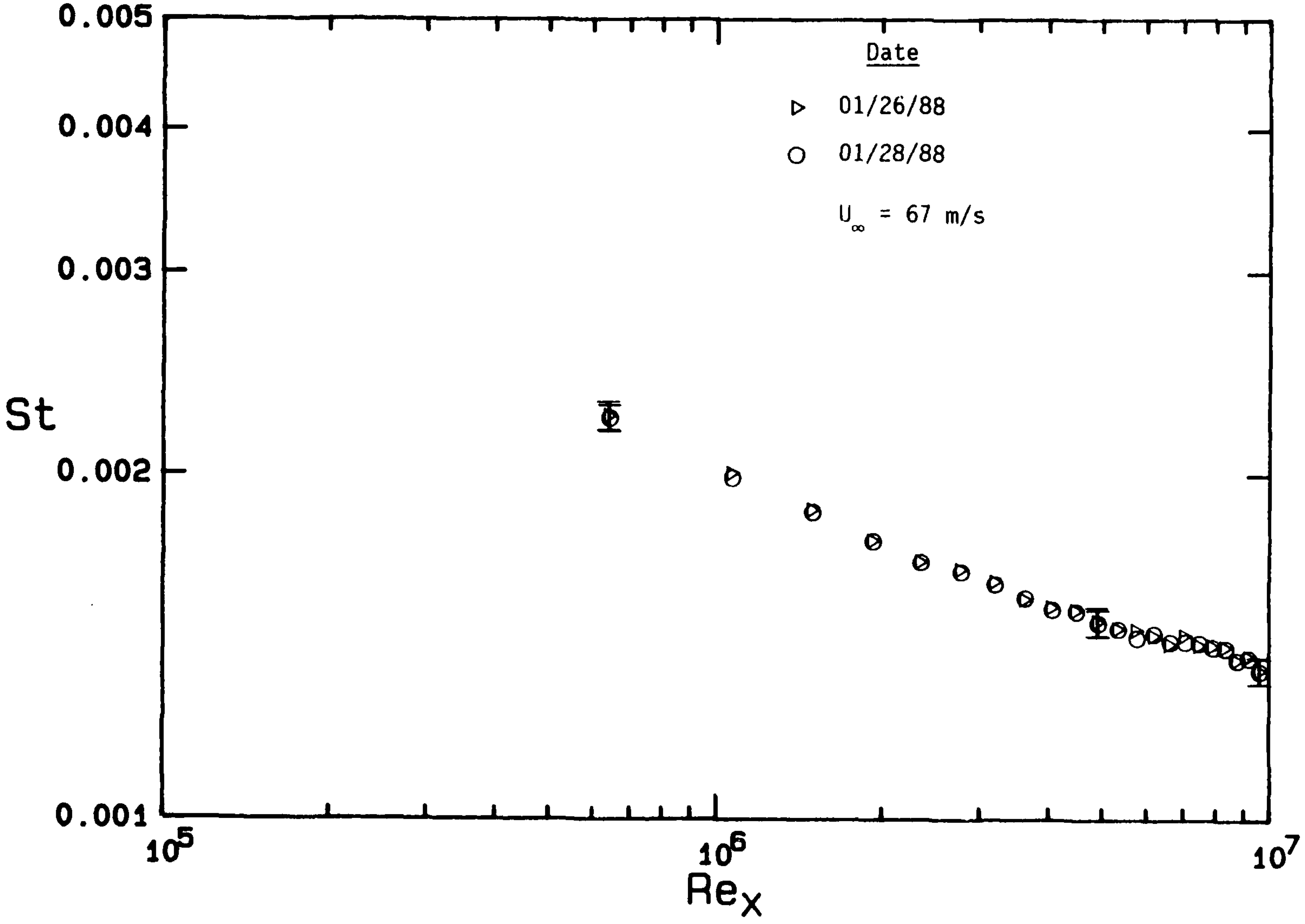

Figure 25. Comparison of Stanton Number Replications for U_∞ = 67 m/s.

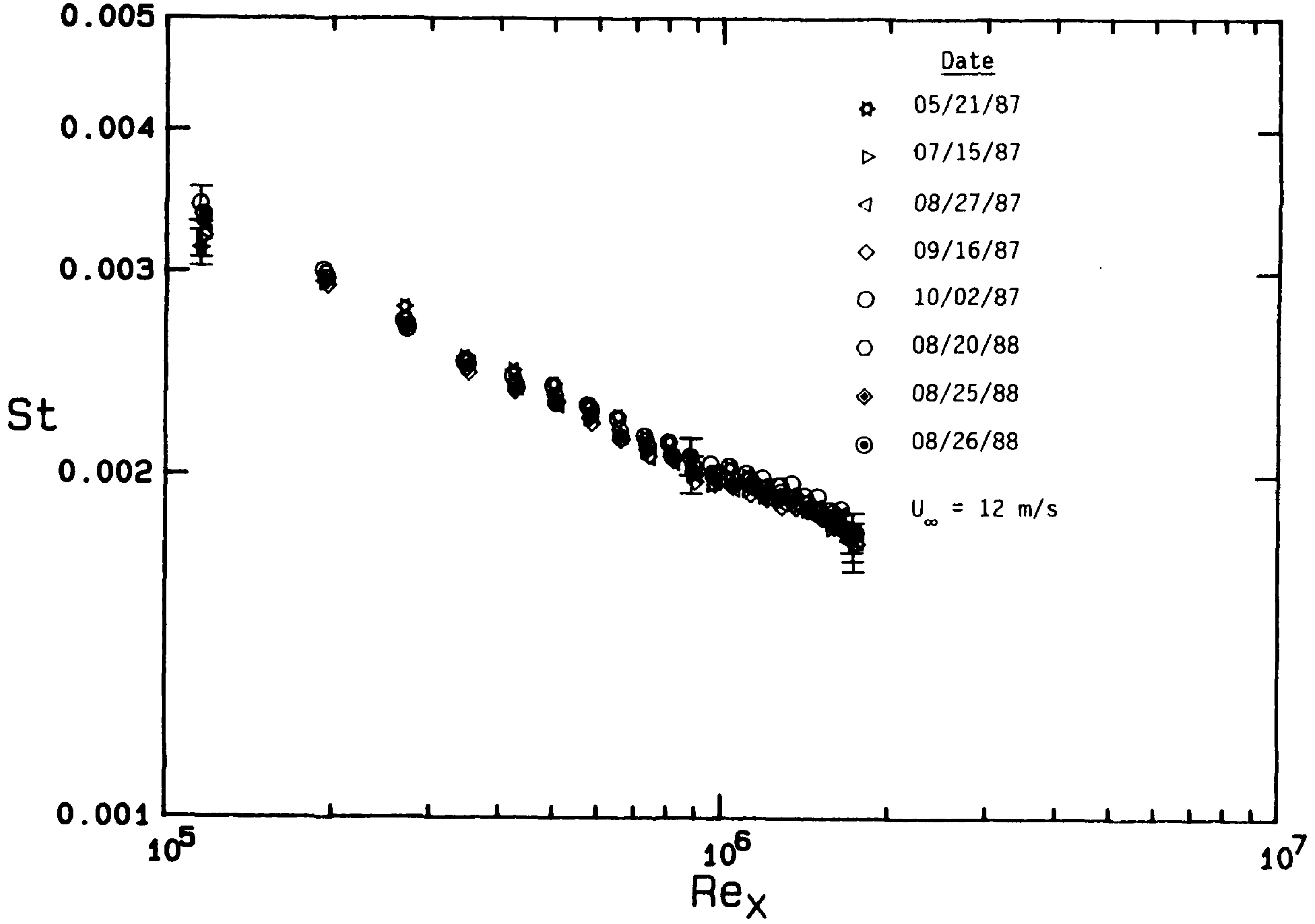

Figure 26. Comparison of Stanton Number Replications for U_∞ = 12 m/s.

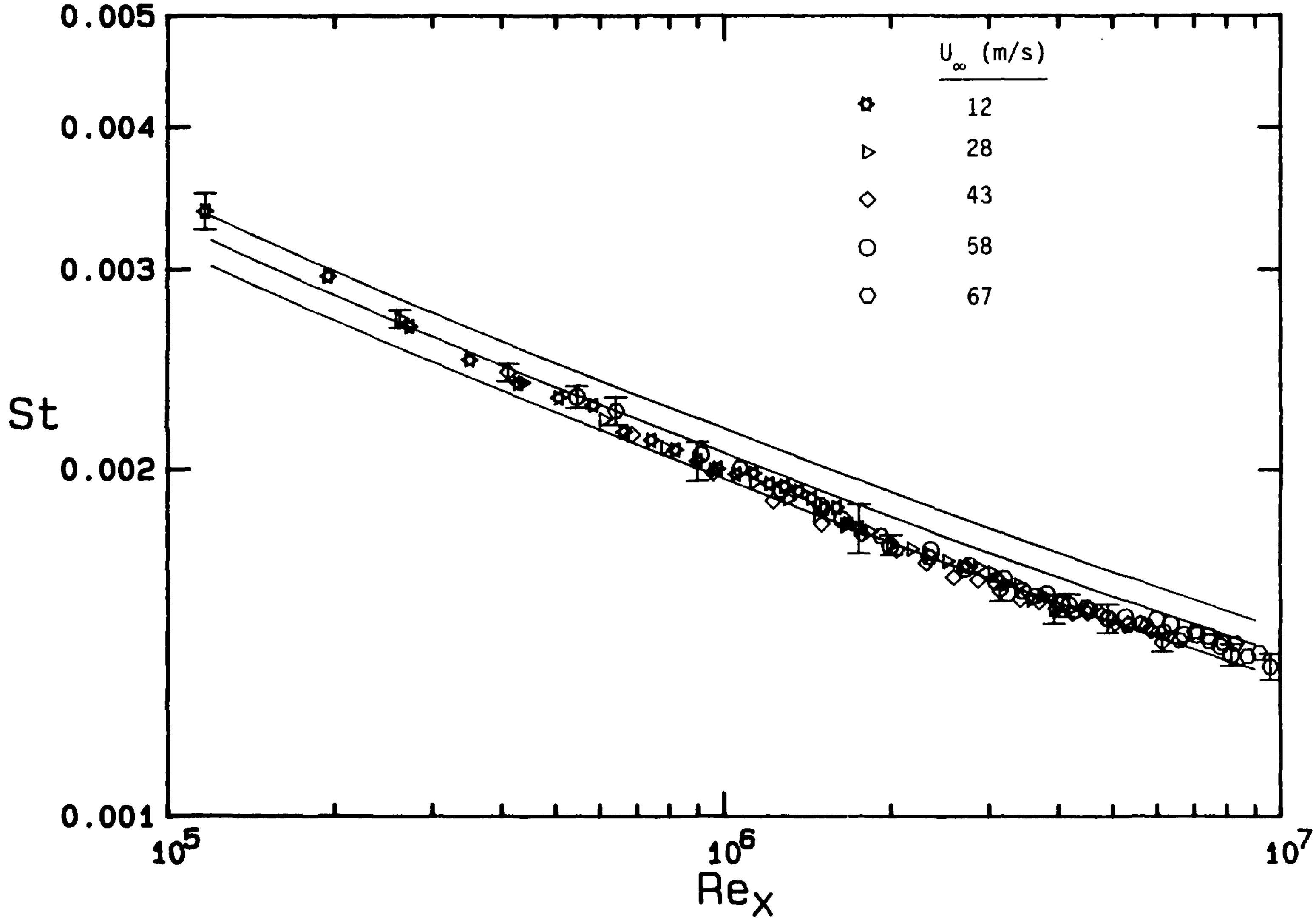

Figure 27. Comparison of the THTTF Smooth Wall Stanton Number Data with the x-Reynolds Number Correlation (equation (5)).

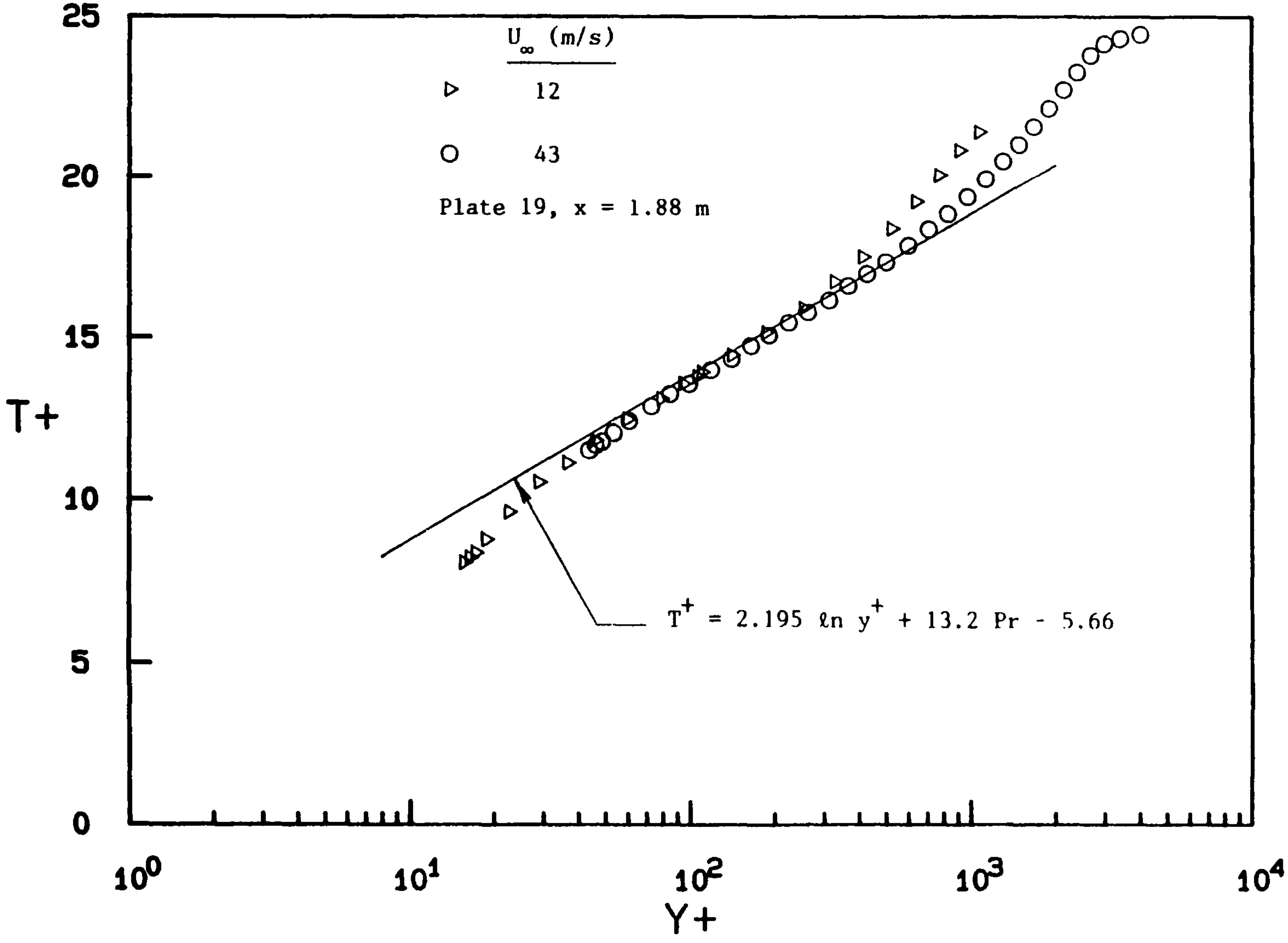

Figure 28. Temperature Profiles at Plate 19 for Freestream Velocities of 12 and 43 m/s Compared with the Law of the Wall.

SECTION 5

ADDITIONAL SMOOTH WALL HEAT TRANSFER RESULTS

In addition to the constant wall temperature qualification data presented in the preceding sections, data were obtained for several other thermal boundary conditions. During the search of the literature for qualification data, only one systematic experimental study of the effect of thermal boundary condition was found (Reynolds, Kays, and Kline 1958 [24]). That work was limited to x-Reynolds numbers less than 3,500,000. Since the THTTF is able to achieve x-Reynolds numbers of 10,000,000, the data reported in this section were taken to add to the existing data and to extend the x-Reynolds number range to 10,000,000. In addition to the constant wall temperature, five thermal boundary conditions were considered: (1) constant heat flux, (2) step wall temperature, (3) step wall heat flux, (4) linear wall temperature variation (ramp down), and (5) bi-linear wall temperature variation (ramp down then ramp up).

The two most basic thermal boundary conditions are those of constant wall temperature and constant heat flux. These two cases are very good approximations for many real heat transfer problems, are relatively easy to construct in the laboratory, and allow ready solution of the boundary layer equations. Therefore, they are often used in test cases for theoretical heat transfer computations.

The step wall temperature case is one of the fundamental problems of convective heat transfer. Under the assumptions of incompressible flow with constant fluid properties, the momentum and energy equations become uncoupled, and the energy equation becomes linear. Therefore, the problem of heat transfer in the boundary layer with arbitrary thermal boundary condition becomes amenable to solution by superposition. The simplest boundary condition for which the solution can serve as a kernel function for superposition is the step wall temperature case. Thus, superposition integral methods can be formulated based on the step wall temperature results to predict the heat transfer (Stanton number) for arbitrary wall temperature or heat flux.

In the following, the theory of heat transfer in the turbulent incompressible smooth wall boundary layer is briefly reviewed and the experimental results are presented, discussed, and compared.

5.1 THEORY

The theoretical treatment of heat transfer in turbulent incompressible smooth flat plate boundary layer flow is mature and well documented (Cebeci and Bradshaw 1984 [38], and Kays and Crawford 1980 [31]). Here the theory is divided into 3 subtopics: analogies, solutions to the integral boundary layer equations, and numerical solutions of the time averaged differential boundary layer equations.

5.1.1 Analogies

Reynolds analogy (Reynolds 1894 [39]) was one of the first theoretical treatments of turbulent heat transfer. For the case of constant freestream velocity and temperature, constant wall temperature, and $Pr = 1$, the similarity between the x-momentum equation and the energy equation yields

$$St = C_f/2 \tag{7}$$

The restrictions on equation (7) prohibit its wide application. Particularly troublesome is the requirement that $Pr = 1$. The two most famous extensions of the analogy for Pr of order 1 or greater are the one of Von Karman 1939 [40] and the one of Colburn 1933 [41].

Von Karman derived his analogy by integrating the thermal and velocity laws-of-the-wall in a three layer model to yield

$$\frac{1}{St} = \frac{2}{C_f} + 5\left[\frac{2}{C_f}\right]^{1/2}\{Pr - 1 + \ln[1 + 5(Pr - 1)/6]\} \qquad (8)$$

Kays and Crawford 1980 [31] have shown that equation (8) can be approximated very well for gases ($0.5 < Pr < 1$) by

$$St\ Pr^{0.4} = C_f/2 \qquad (9)$$

Colburn based his analogy completely on dimensional analysis and empirical considerations. His analogy is

$$St\ Pr^{0.66} = C_f/2 \qquad (10)$$

Although equation (10) was first determined by Colburn purely from empirical considerations, it has been deduced from turbulent scaling laws for $Pr > 1$ (Bejan 1984 [42] and Arpaci and Larsen 1984 [43]).

Other analogies can be derived from the velocity and temperature laws-of-the-wall (Kader and Yaglom 1972 [44], for example). All of these analogies are still limited to the constant wall temperature boundary condition. However, this limitation is often not stressed and the analogies are often compared with constant heat flux experiments.

5.1.2 Integral Equations

For the integral analysis, we assume constant freestream velocity and temperature and a constant property fluid flow over a smooth flat plate. For arbitrary wall temperature or heat flux, we follow the procedure of Reynolds, Kays and Kline 1958 [24] as presented by Kays and Crawford 1980 [31]. The procedure is to use the solution of the integral boundary layer equations for the step wall temperature with an unheated starting length as the kernel function in a superposition integral. Using the 1/7 power law approximation of the velocity and temperature profiles, Reynolds, Kays, and Kline established that for an unheated starting length, ξ, the local heat transfer coefficient can be expressed as

$$St(\xi;x) = \frac{h(\xi;x)}{\rho U_\infty C_p} = St_t(x)[1 - (\xi/x)^{9/10}]^{-1/9} \qquad (11)$$

where $St_t(x)$ is the constant wall temperature Stanton number given by the analogy of choice from equations (7) - (10). The heat flux for a variable wall temperature, $T_w(x)$, is

$$q''_w(x) = \int_0^x h(\xi;x) \frac{d(T_w - T_\infty)}{d\xi} d\xi + \sum_{i=1}^{N} h(\xi_i;x)\Delta(T_{w,i} - T_\infty) \qquad (12)$$

where $\Delta(T_{w,i} - T_\infty)$ is the i'th finite step in wall temperature, N is the number of steps, and the ξ_i are the locations of the steps.

For a piecewise linear wall temperature with a finite number of steps

$$T_w - T_\infty = \sum_{j=1}^{M} m_j(x - a_j) + \sum_{j=1}^{M} b_i \qquad (13)$$

application of equation (12) with equation (11) yields

$$St(x) = \frac{10xSt_t(x)}{9(T_w - T_\infty)} \sum_{j=1}^{M} m_j \, \beta_{r_j}(8/9,10/9)$$

$$+ \frac{St_t(x)}{T_w - T_\infty} \sum_{i=1}^{N} b_i[1 - (\xi_i/x)^{9/10}]^{-1/9} \qquad (14)$$

where $\beta_{r_j}(8/9,10/9)$ is the incomplete beta function with $r_j = 1 - (a_j/x)^{9/10}$

$$\beta_r(a,b) = \int_0^r z^{a-1}(1-z)^{b-1}\, dz \qquad (15)$$

For the step heat flux case with unheated length ϕ,

$$\frac{St}{St_t} = \frac{\Gamma(1/9)\ \Gamma(8/9)}{\beta_r(1/9,\ 10/9)} \tag{16}$$

with $r = 1 - (\phi/x)^{0.9}$

5.1.3 Differential Equations

The finite difference solution of the incompressible boundary layer equations is now routine for smooth wall cases. Cebeci and Bradshaw 1984 [38] present a complete discussion of these solutions. The solutions presented in this section are based on a mixing length turbulence model with van Driest damping and a constant turbulent Prandtl number, $Pr_t = 0.9$. For these computations, the BLACOMP code as verified by Gatlin 1983 [45] was used. The particular details of the solutions presented here can be found in Love et al. 1988 [46]. As was the case with the experimental data reduction, all fluid properties were assumed to be constant and were evaluated at the freestream static temperature.

5.2 EXPERIMENTAL RESULTS

Stanton number data were taken for both constant wall temperature and constant heat flux boundary conditions for nominal freestream velocities of 12, 27, 42, and 67 m/s. The experiments were conducted so that the constant heat flux cases had approximately the same wall temperature far from the boundary layer origin as the corresponding constant wall temperature cases. These data are compared with the analogies, the integral solutions, and the numerical solutions of the boundary layer equations. However, the primary comparison is the comparison of the data sets with each other.

Figure 29 presents a plot of St versus Re_x for the two boundary conditions (constant q''_w and T_w). The solid symbols are the results for the constant heat flux boundary condition and the open symbols are for the constant wall temperature boundary condition. The solid curve is the analogy of equation (9), $StPr^{0.4} = C_f/2$, where the skin friction coefficient is determined using the Schultz-Grunow 1941 [29] correlation

$$C_f/2 = 0.185[\mathrm{Log}_{10}(Re_x)\ ]^{-2.584} \tag{17}$$

The figure shows that the analogy fits the constant wall temperature data very well for the Reynolds number range (100,000 to 10,000,000). At the maximum deviation the correlation is about 5 percent too high. The dashed curve is based on the integral solution, equation (16), for the case of constant q''_w

$$St = \frac{\Gamma(1/9)\ \Gamma(8/9)}{\beta_1(1/9,10/9)} St_t = 1.043\ St_t \tag{18}$$

Far from the boundary layer origin, equation (18) agrees almost exactly with the data. For Reynolds numbers between 3,000,000 and 10,000,000, the constant wall heat flux data are consistently 4 to 5 percent greater than the constant wall temperature data. However, near the origin of the boundary layer the constant wall heat flux data are 10 to 15 percent above the constant wall temperature data.

The two boundary conditions are compared more directly in Figure 30. The ratio of constant wall heat flux to constant wall temperature Stanton numbers is plotted directly. The dashed curve represents the integral solution, equation (18), and the solid lines represent the numerical solutions of the boundary layer equations. For Reynolds numbers greater than 3,000,000, the data agree very closely with equation (18). But, for the low Reynolds numbers, the data indicate a ratio of 1.10 to 1.15 instead of 1.04. The numerical solutions agree with the data for all of the Reynolds numbers. The numerical solutions indicate a slight unit Reynolds number effect which is perhaps suggested by the data but not proven.

As previously discussed, the Reynolds analogies strictly apply only for the constant wall temperature boundary condition. However, they are also considered to apply approximately for the constant heat flux boundary condition. Constant wall heat flux data are often reported in terms of the Reynolds analogy factor, $2St/C_f$, (for example, Subramanian and Antonia 1981 [47], and Simonich and Bradshaw 1978 [48]). In Figure 31 the data are presented in analogy coordinates, $2St/C_f$, directly. Again the solid symbols are the constant q''_w results and the open symbols are the constant T_w results. The skin friction coefficients are the values measured with a Preston tube. The dashed lines are, as indicated, the Colburn analogy, $Pr^{-0.66}$, and the approximation of Von Karman's analogy, $Pr^{-0.4}$. The solid lines represent the results from the numerical solutions. The analogy factors for the constant T_w data are more or less constant for the whole Reynolds number range. The data scatter about the value of about 1.2 which is approximately halfway between the two analogies. The numerical solutions for the constant T_w case are in very good agreement with the data. They are practically constant at $2St/C_f = 1.18$ to 1.2 and show only a small unit Reynolds number effect. The analogy factors for the constant q''_w boundary condition show a Reynolds number dependence. The ratio decreases from about 1.4 at low Reynolds numbers to about 1.24 at the higher Reynolds numbers. The numerical solutions are in good agreement with the data and show a small unit Reynolds number effect. Simonich and Bradshaw 1978 [48] and Subramanian and Antonia 1981 [47] presented limited heat transfer data for turbulent boundary layers with constant q''_w boundary conditions. Simonich and Bradshaw found that $2St/C_f$ varied between 1.3 at low Reynolds numbers to 1.2 at $Re_x = 3,500,000$. Subramanian and Antonia found $2St/C_f$ to vary from 1.5 at low Re_x to 1.4 at $Re_x = 3,000,000$. These results are in substantial agreement with the present results.

For unheated starting length boundary conditions, Stanton number measurements were made at nominal freestream velocities of 28 m/s and 67 m/s. Three cases were run at each velocity for each boundary condition (step T_w and q''_w). The lengths of the unheated regions were chosen so that an appropriate spread in Reynolds numbers, Re_ϕ, was obtained. At $U_\infty = 28$ m/s, the unheated starting lengths were 0.3 m, 0.7 m, and 1.3 m. At $U_\infty = 67$ m/s, they were 0.5 m, 0.8 m, and 1.3 m.

Figure 32 shows a summary of the Stanton number data for a constant wall temperature boundary condition and the step T_w cases for $U_\infty = 28$ m/s and 67 m/s. The first heated plate is highlighted in each case by plotting its data as a solid symbol. Data from the last plate is not plotted for any case. The figure shows that a step in wall temperature has a large effect on the Stanton number in the heated region near the step. But as the thermal boundary layer develops, the Stanton numbers approach the results for the constant wall temperature boundary layers. The starting lengths were chosen so that the last case at $U_\infty = 28$ m/s and the first case at $U_\infty = 67$ m/s had approximately the same value of Re_ϕ. Based on the data of Reynolds et al., the results of these two cases should coincide when plotted as St versus Re_x. The figure shows that this is true for the present results.

Figure 33 shows a comparison of the results of the step T_w experiments with the integral solution in equation (11), dashed lines, and with the finite difference solutions, solid lines, for $U_\infty = 28$ m/s. Figure 34 shows the same comparison for $U_\infty = 67$ m/s. The results are presented in terms of St/St_t for a direct comparison with equation (11). The St_t data were used to normalize the St data, and the finite difference solutions for constant wall temperature, St_t, were used to normalize the finite difference solutions, St. The figures show that both the finite difference and integral solutions are in good agreement with the data in all cases. The integral solutions are consistently low by a small amount in the region of the step in wall temperature. From the comparisons in the figures, it can be concluded that equation (11) is still appropriate for values of $Re_x \rightarrow 10^7$.

Figure 35 shows a summary of the Stanton number data for a constant heat flux boundary condition and the step q''_w cases for $U_\infty = 28$ m/s and 67 m/s. The figure shows that as the thermal boundary layer develops, the unheated starting length Stanton numbers approach the results for the constant heat flux boundary condition. The first heated plate is highlighted in each case by plotting its data as a solid symbol. Data from the last plate is not plotted for any case.

Figure 36 shows a comparison of the results of the experiments with the integral solution in equation (16), dashed lines, and with the finite difference solutions, solid lines, for $U_\infty = 28$ m/s. Figure 37 shows the same comparison for $U_\infty = 67$ m/s. As before, the results are presented in terms of St/St_t for a direct comparison with equation (16). The figures show that the finite difference solutions are in very good agreement with the data in all cases. The integral solutions are also in reasonable agreement with the data, with the maximum difference between the data and the integral solutions being about 10 percent.

As examples of variable wall temperature boundary conditions, one linearly decreasing (ramp down) and two bi-linear (ramp down then ramp up) wall temperature distributions were used for experiments at freestream velocities of 28 and 67 m/s. The measured axial wall temperature distributions are shown in Figure 38. A discussion of the complete data set is given in Love et al. 1988 [46]. Only two sample cases are given here.

Figure 39 displays the data for the linear wall temperature distribution for a freestream velocity of 67 m/s. The dashed line represents the integral solutions of equation (14), and the solid line represents the numerical solutions. The solid symbols indicate the locations of changes in the slope of the wall temperature distribution. Figure 40 shows the same information for the bi-linear wall temperature distribution with 1.0°C temperature difference from plate to plate. Similar to the unheated starting length cases, the ratio St/St_t is used for a direct comparison with the results of the superposition integral. Although the numerical solutions predict a greater response to changes in the wall temperature, both the numerical and integral solutions are in reasonable agreement with the experimental data.

5.3 SUMMARY

This study extended the x-Reynolds number range of such data for incompressible smooth flat plate flows from a maximum of 3,500,000 to 10,000,000. As seen in Section 4, the Stanton numbers for constant T_w were in good agreement with the Von Karman analogy over the entire Reynolds number range when the skin friction coefficient given by the Schultz-Grunow correlation is used. Stanton numbers for the constant heat flux boundary condition were 5 to 15% higher than those for the constant wall temperature boundary condition. The constant wall temperature experiments yielded Reynolds analogy factor, $2St/C_f$, data which scattered about the constant 1.2. The analogy factor decreased from about 1.4 at lower Reynolds numbers to 1.2 downstream for the constant heat flux boundary condition. The numerical solutions were in good agreement with the data for both the constant wall temperature and constant heat flux cases.

The integral solutions and numerical solutions were in substantial agreement with the experimental Stanton number data for the constant wall temperature and constant heat flux boundary conditions with unheated starting lengths. The integral solutions and the numerical solutions gave good agreement with the experimental Stanton number data for the linear and bi-linear wall temperature distributions. The effect of a decreasing wall temperature in the flow direction was to lower the local Stanton number to less than the constant wall temperature Stanton number St_t. As the wall temperature increased in the flow direction, the local Stanton number became greater than St_t.

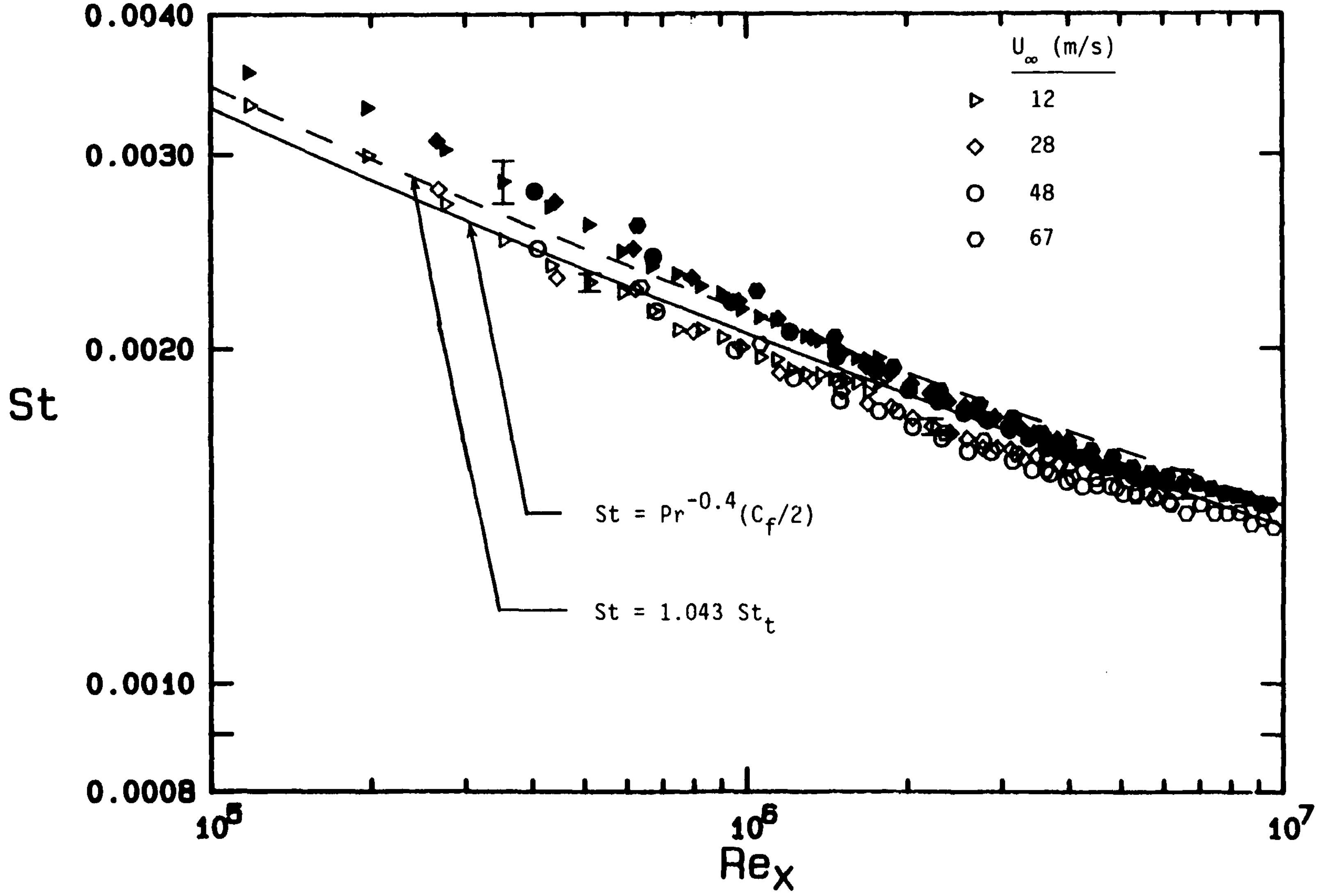

Figure 29. Stanton Number Results for Constant Wall Temperature (open symbols) and Constant Wall Heat Flux (solid symbols).

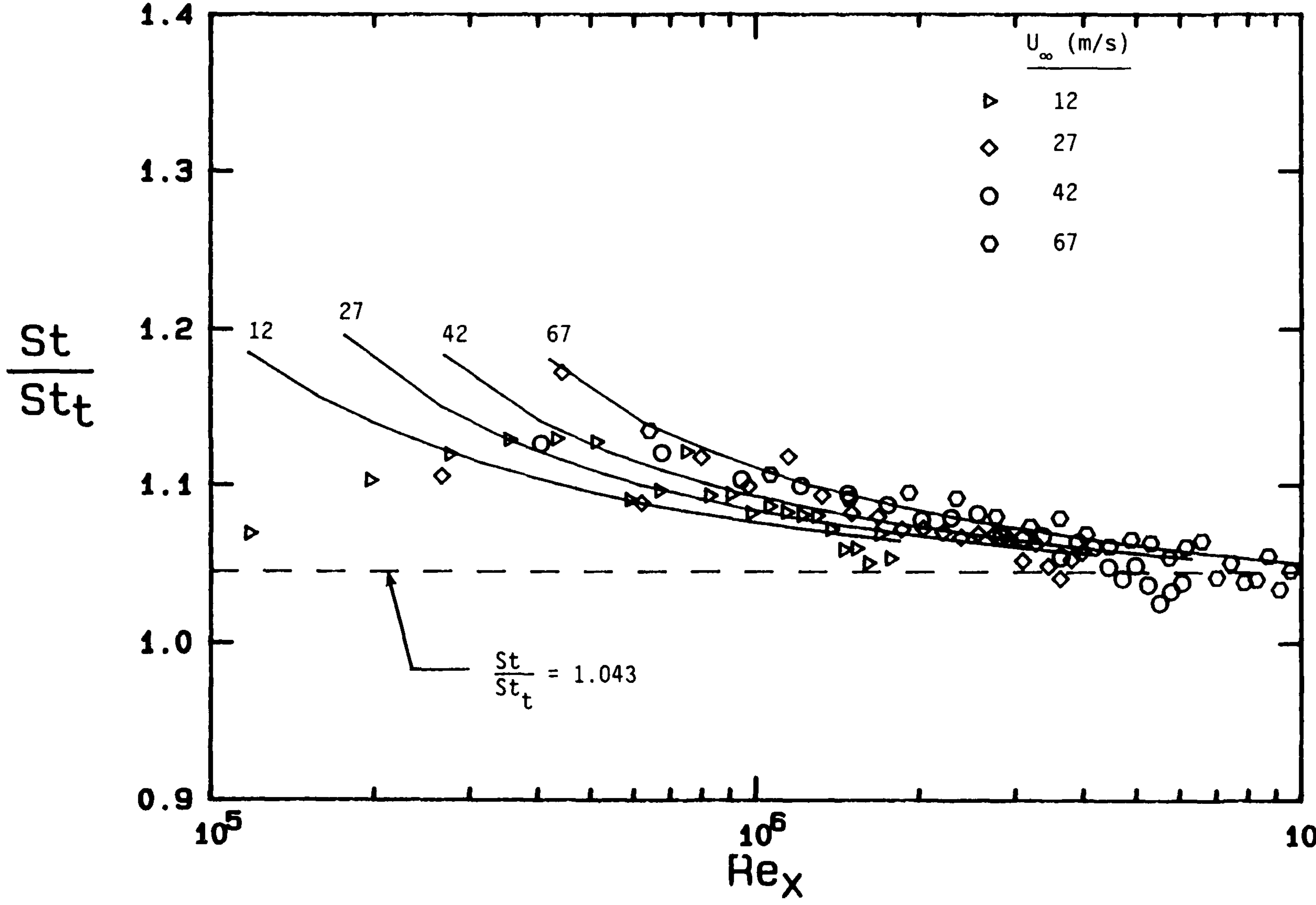

Figure 30. Direct Comparison of Constant Heat Flux and Constant Wall Temperature Thermal Boundary Conditions.

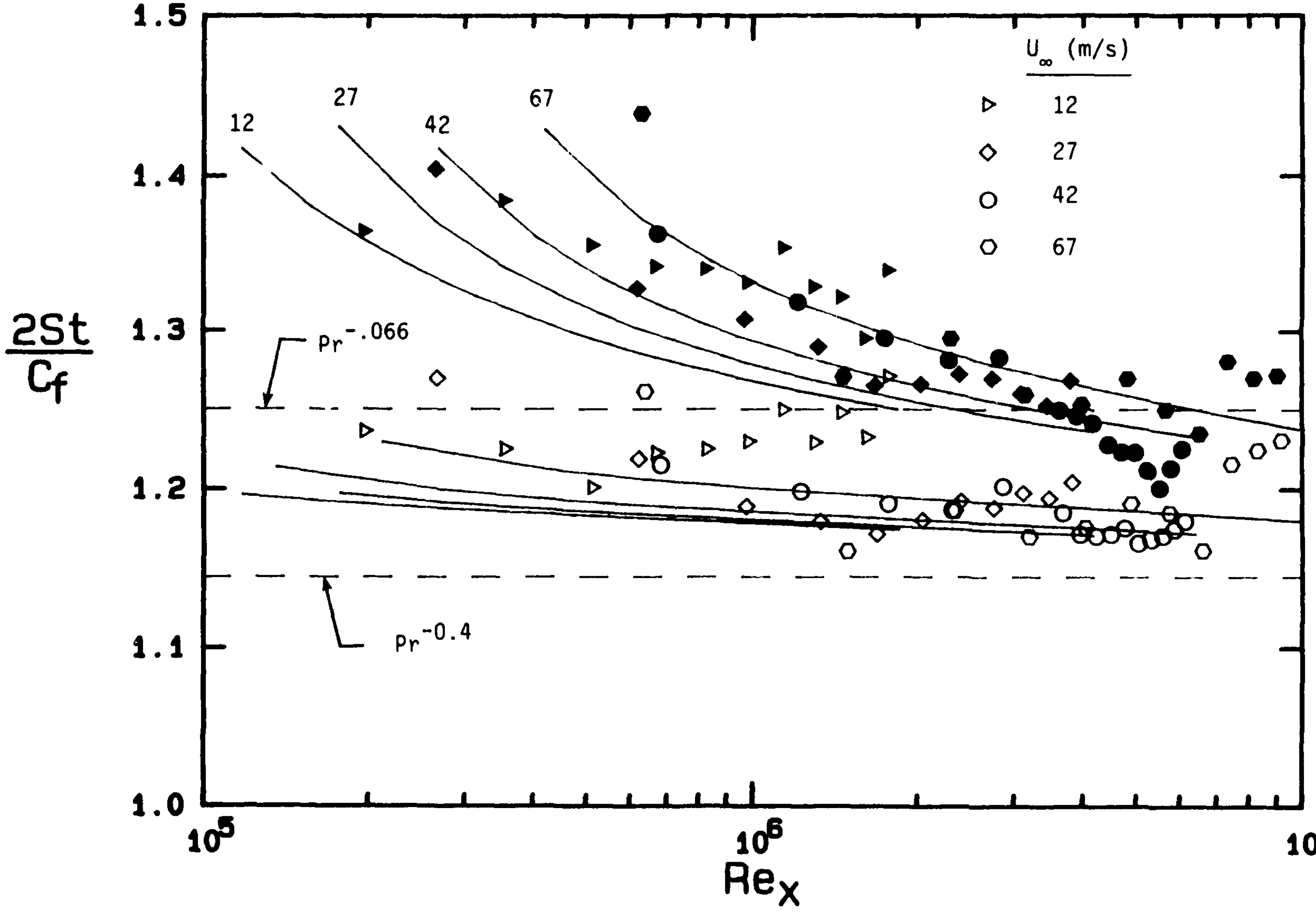

Figure 31. Comparison of the Reynolds Analogy Factor with the Analogies and with the Numerical Solutions; Open Symbols are Constant T_w and Solid Symbols are Constant q''_w.

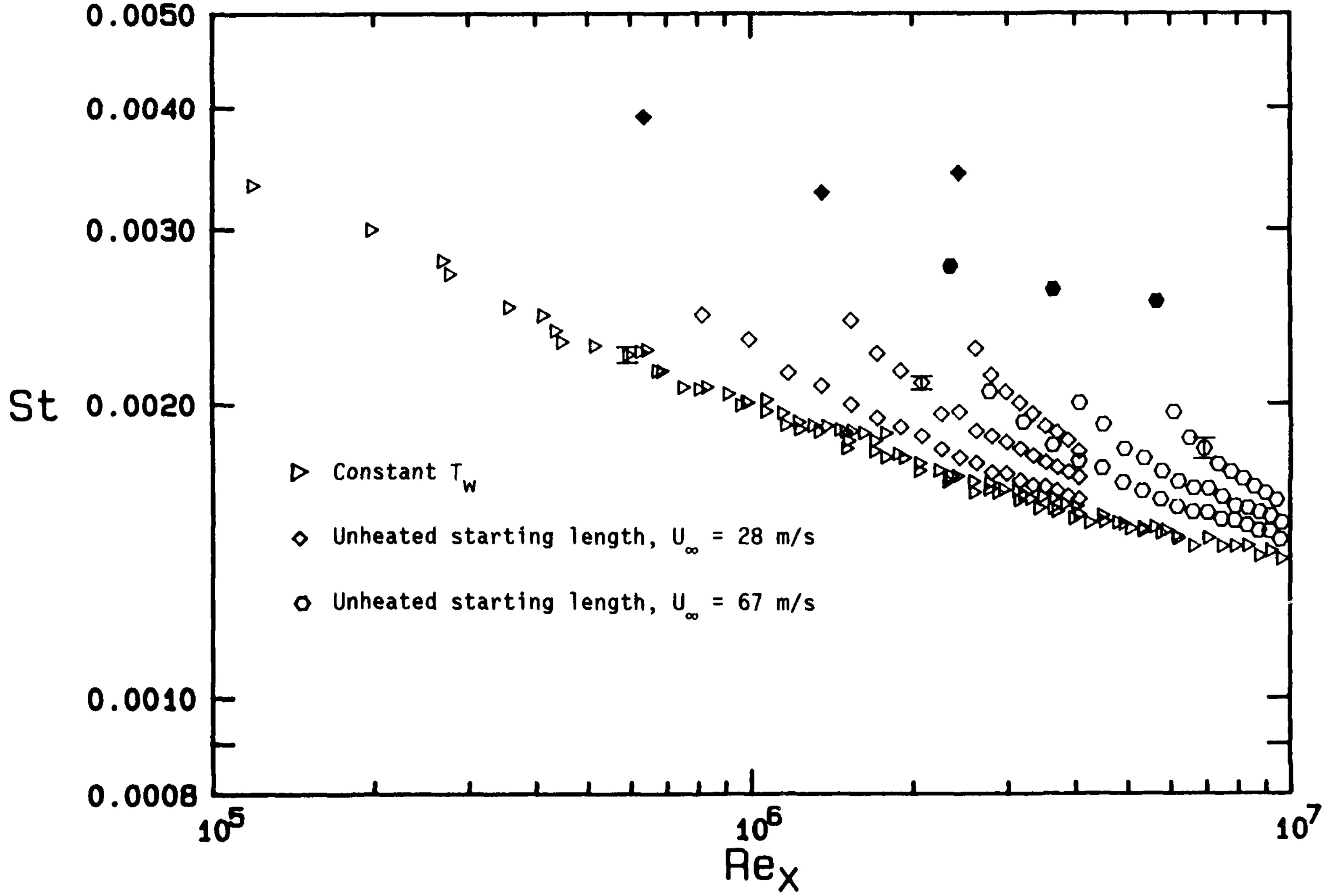

Figure 32. Stanton Numbers for Constant T_w with Unheated Starting Lengths. Filled Symbols Indicate First Heated Plate.

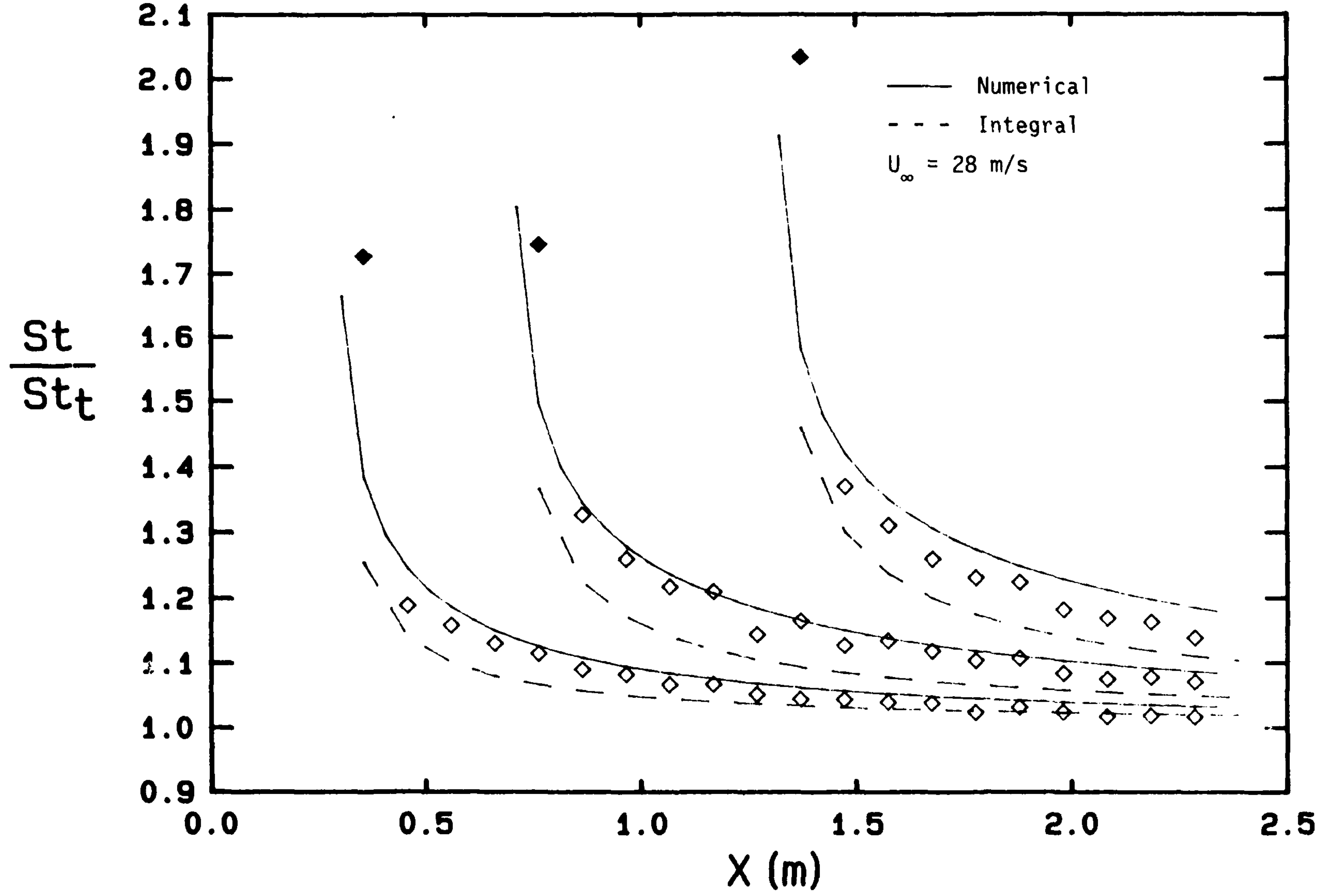

Figure 33. Comparison of the Results of the Step T_w Experiments with the Integral and Finite Difference Solutions.

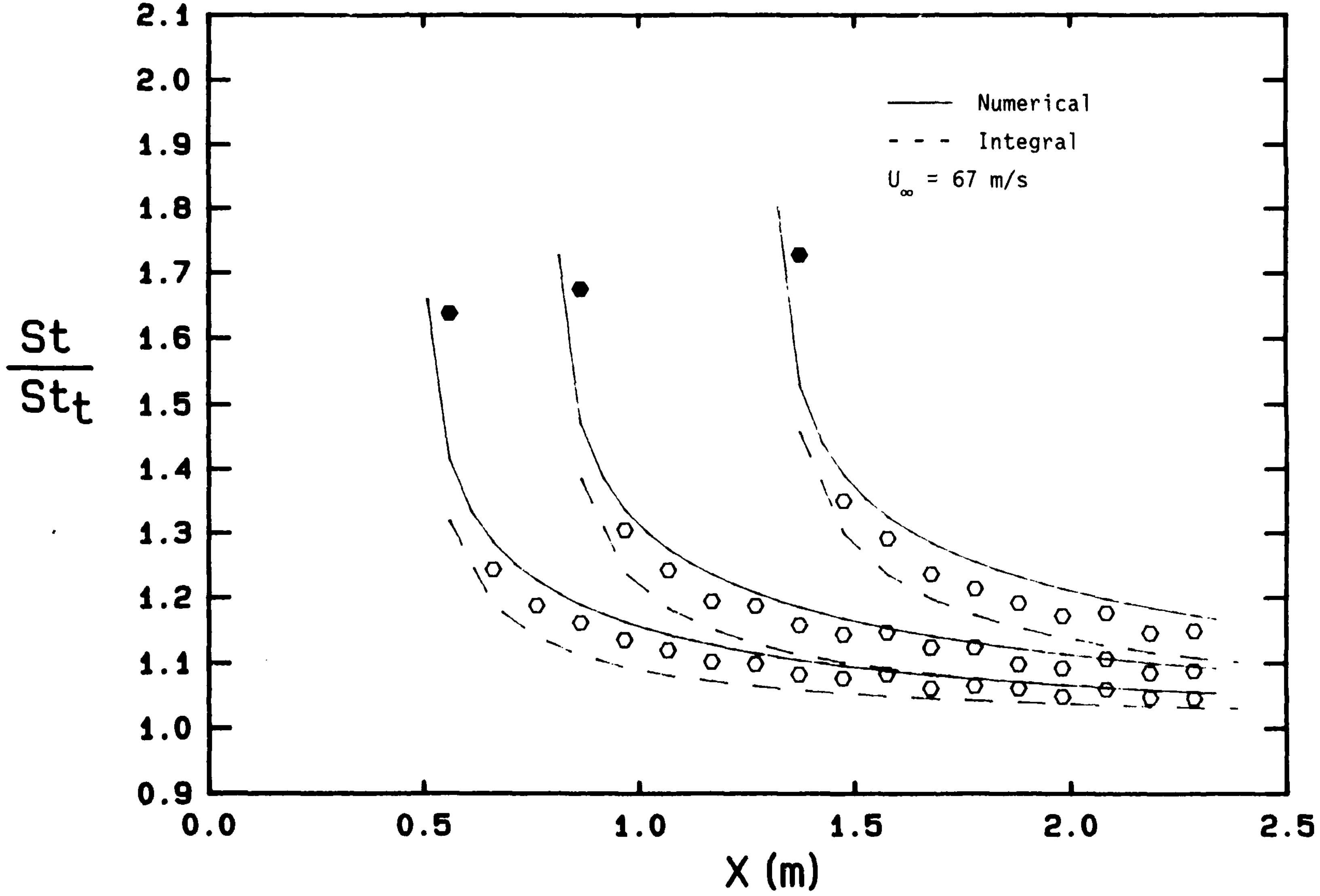

Figure 34. Comparison of the Results of the Step T_w Experiments with the Integral and Finite Difference Solutions.

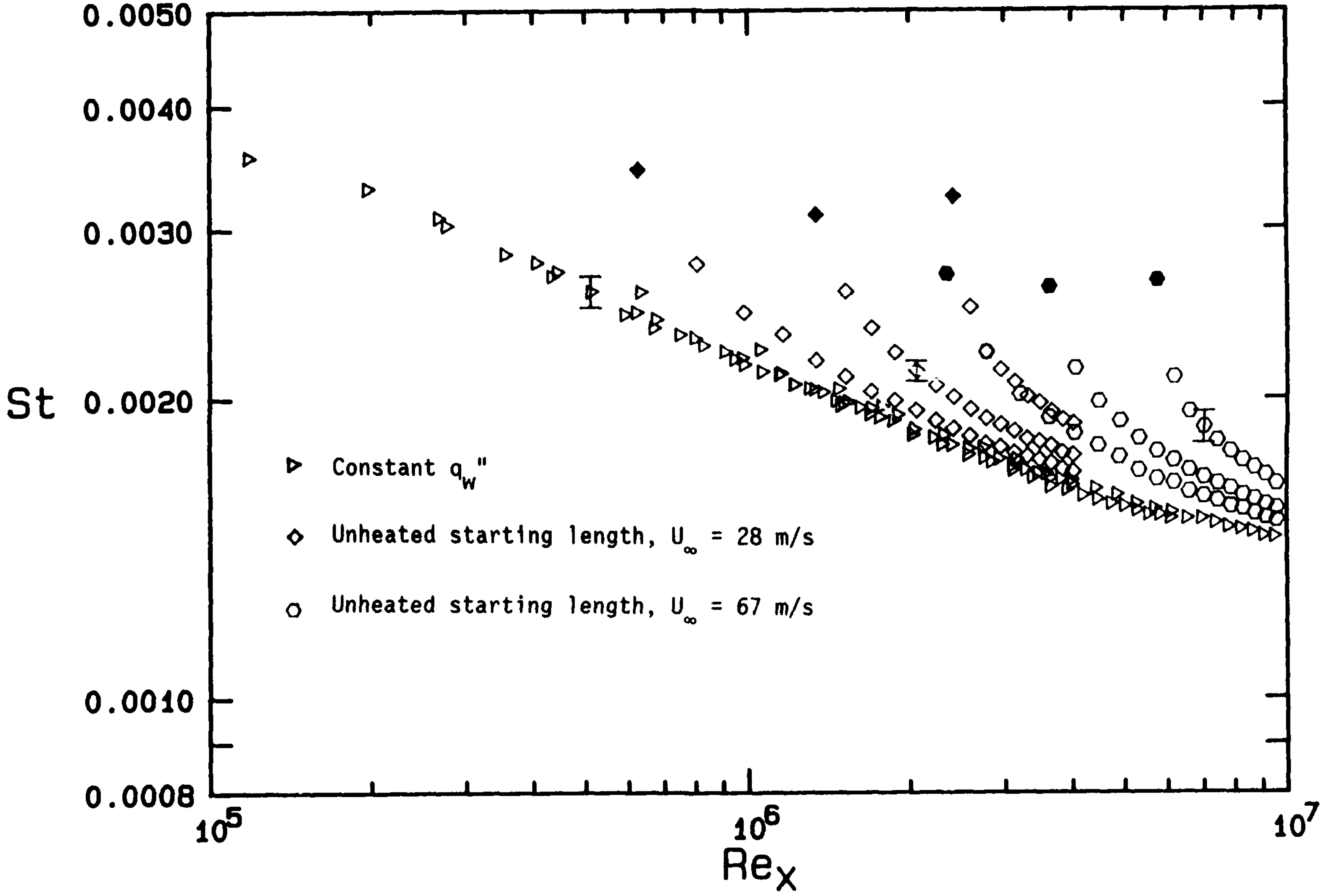

Figure 35. Stanton Numbers for Constant q_w'' with Unheated Starting Lengths. Filled Symbols Indicate First Heated Plate.

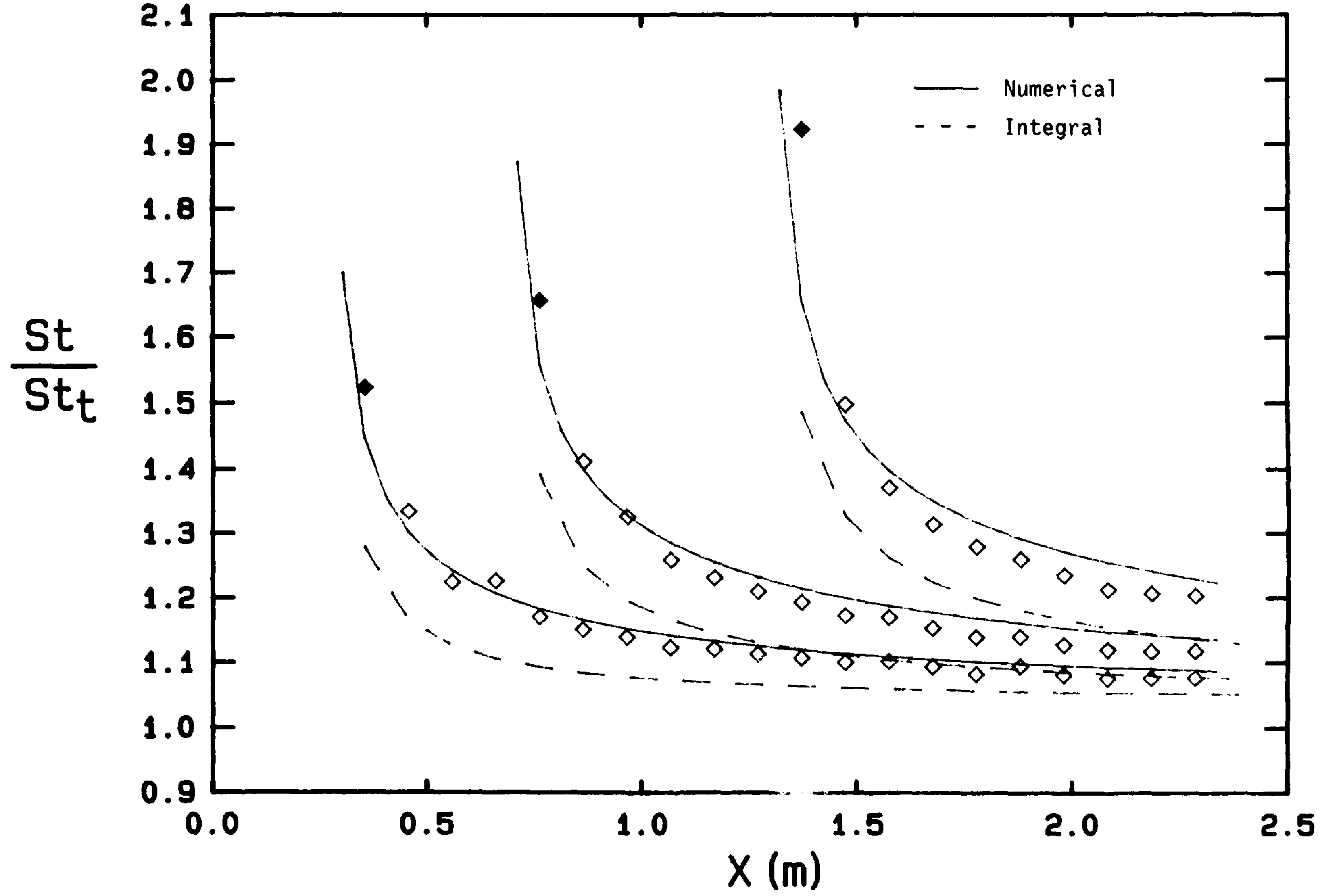

Figure 36. Comparison of Experimental Stanton Number Ratios for Constant q_w'' with Unheated Starting Lengths with Integral Solutions and Numerical Solutions--U_∞ = 67 m/s. Filled Symbols Indicate First Heated Plate.

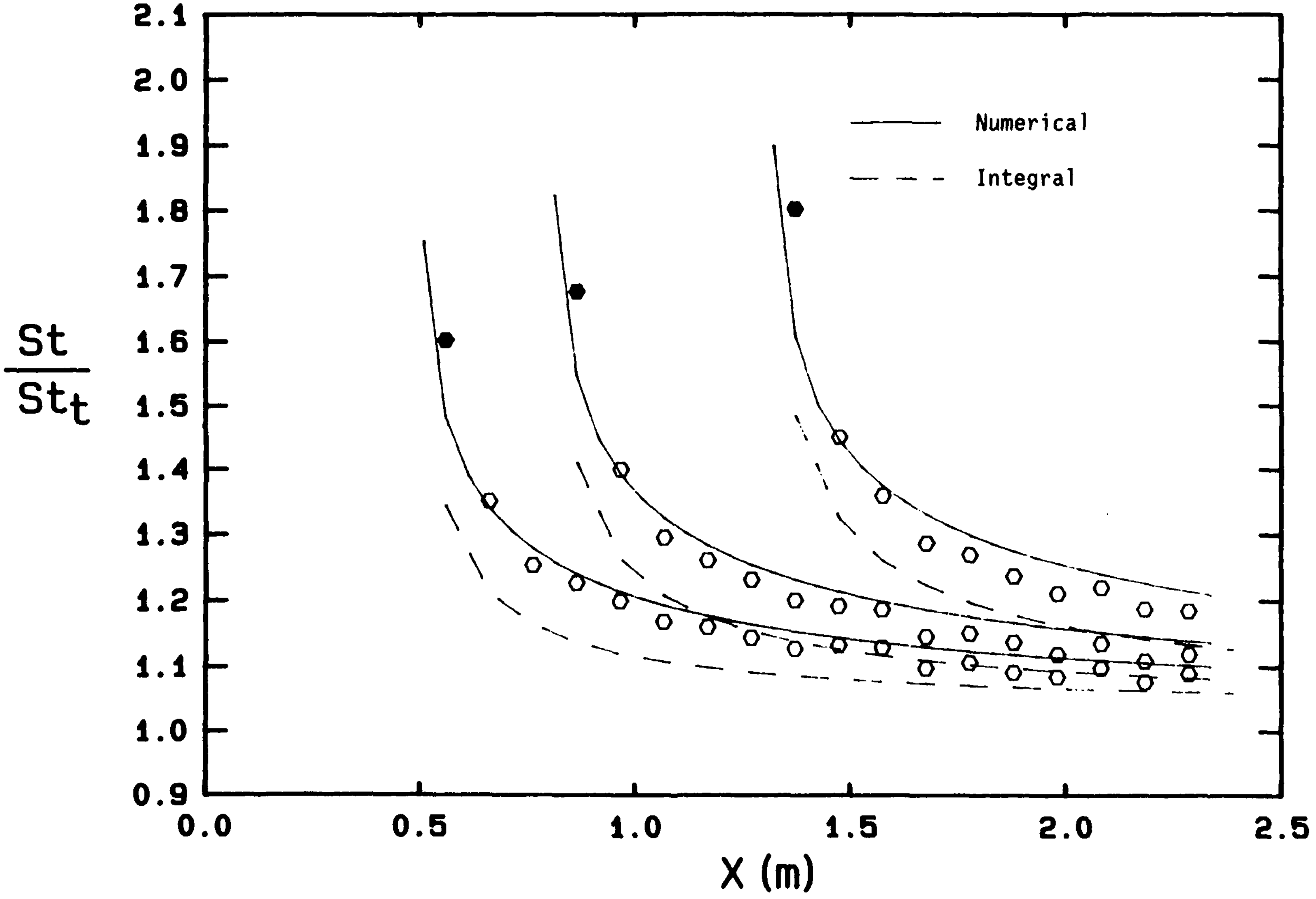

Figure 37. Comparison of Experimental Stanton Number Ratios for Constant q_w'' with Unheated Starting Lengths with Integral Solutions and Numerical Solutions--U_∞ = 67 m/s. Filled Symbols Indicate First Heated Plate.

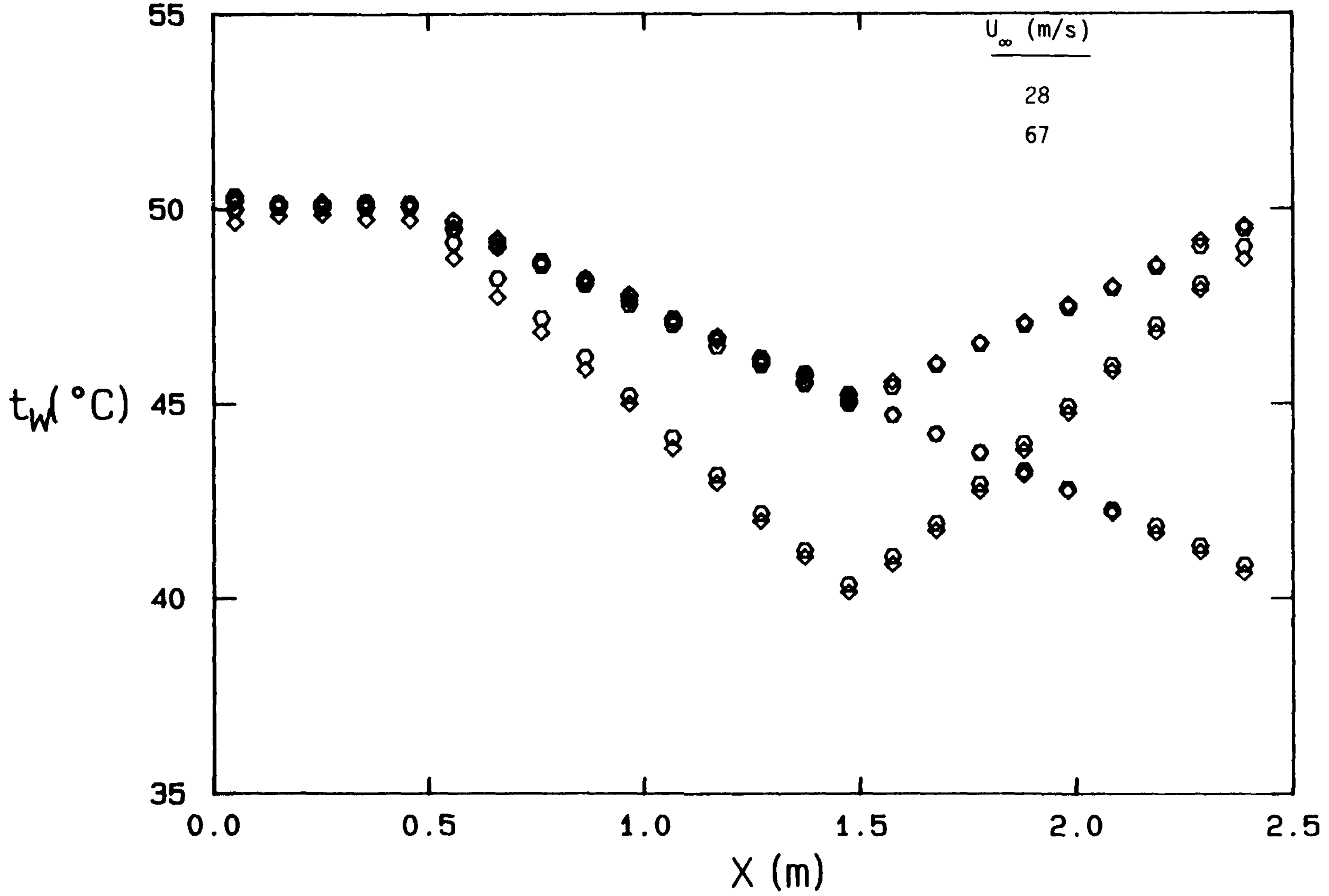

Figure 38. Experimental Linear and Bi-linear Wall Temperature Distributions.

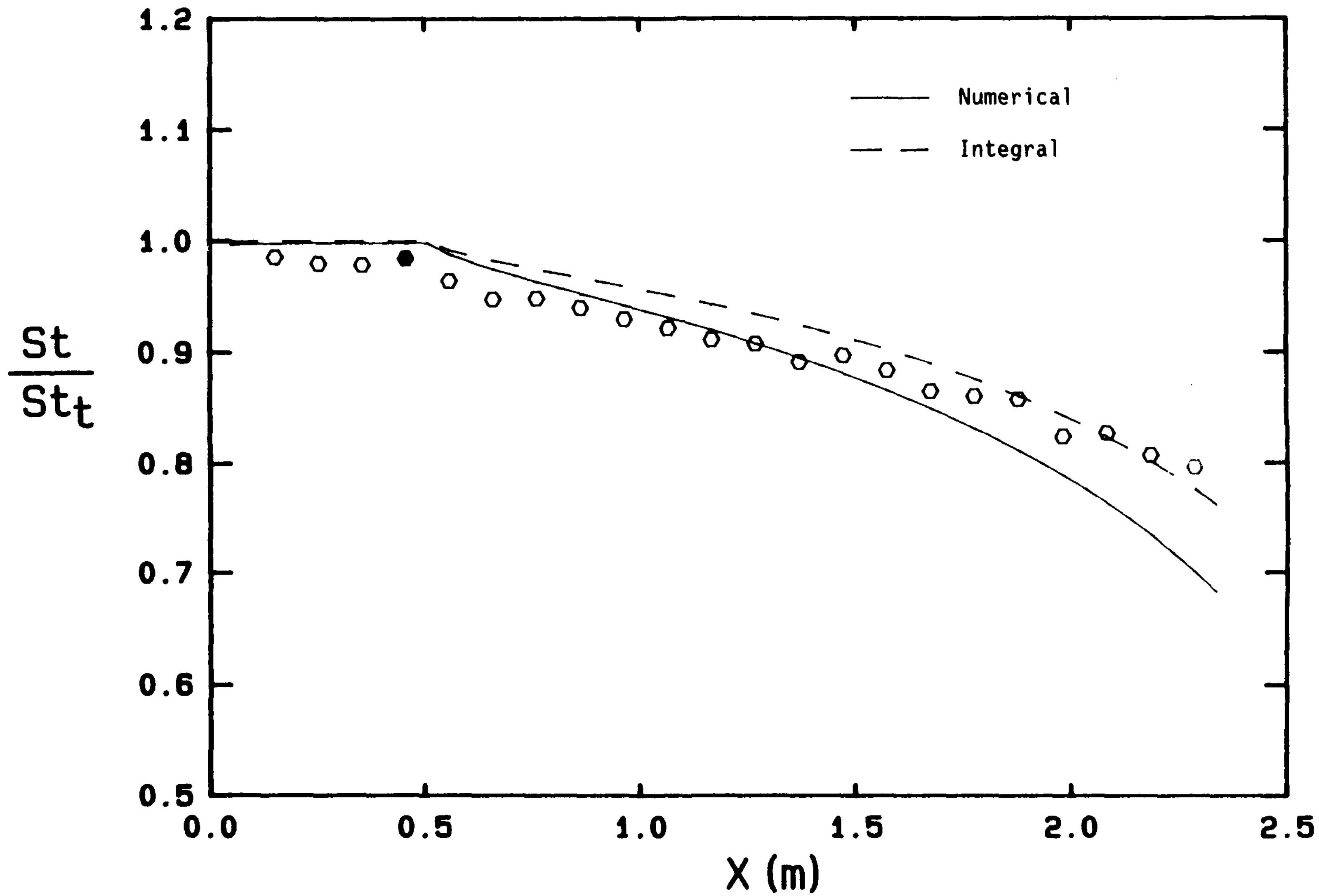

Figure 39. Comparison of Experimental Stanton Number Ratio for the Linear Wall Temperature Distribution with Integral and Numerical Solutions--U_∞ = 67 m/s. Filled Symbol Indicates Change in Slope of T_w.

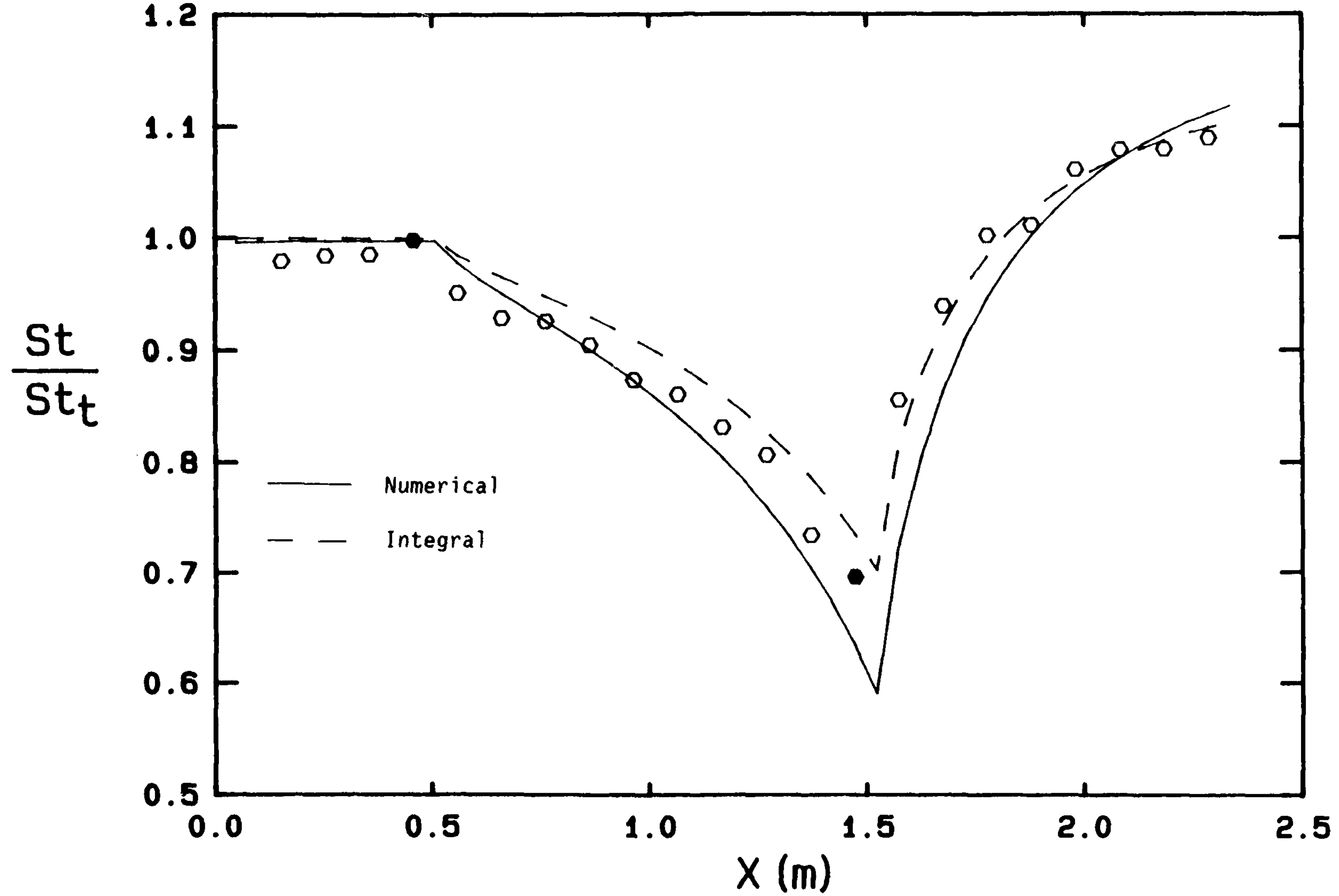

Figure 40. Comparison of Experimental Stanton Number Ratio for Bi-linear Wall Temperature Distribution with 1°C Plate to Plate Temperature Difference with Integral and Numberical Solutions--U_∞ = 67 m/s. Filled Symbol Indicates Change in Slope of T_w.

SECTION 6
ROUGH WALL RESULTS

Stanton number data have been obtained on one rough surface for freestream velocities of 6, 12, 28, 43, 58 and 67 m/s. This surface is the one roughened with 1.27 mm diameter hemispherical elements spaced 4 diameters apart in a staggered array as shown in Figure 41. In addition, skin friction coefficient distributions have been obtained at $U_\infty = 12$ and 58 m/s. Profiles of mean velocity, mean temperature, and the Reynolds stress quantities $\overline{u'^2}$, $\overline{v'^2}$, $\overline{w'^2}$, and $\overline{u'v'}$ have also been measured. These data are presented and discussed in this section along with a comparison with Stanton number and skin friction coefficient predictions made using the discrete element roughness model of Taylor, Coleman and Hodge 1984 [49].

6.1 REVIEW OF THE DISCRETE ELEMENT PREDICTION MODEL

The development and calibration of the discrete element prediction model has previously been described. Only an overview is given here. The basic idea of the discrete element approach is to treat the roughness as a collection of individual entities and to account for the blockage, form drag, and heat transfer on the elements. The discrete element model presented here is formulated for roughness elements with three-dimensional shapes (as opposed to transverse ribs, for example) for which the element cross-section can be approximated as circular at every height, y.

The differential equations including roughness effects are derived by applying the basic conservation statements for mass, momentum and energy to a control volume (CV) such as that shown in Figure 42. Upon incorporating the boundary layer assumptions, the continuity, momentum and energy equations for a steady (Reynolds-averaged), two-dimensional turbulent boundary layer are

$$\frac{\partial}{\partial x}(\rho\beta_x u) + \frac{\partial}{\partial y}(\rho\beta_y v) = 0 \tag{19}$$

and

$$\begin{aligned}
\beta_x\rho u \frac{\partial u}{\partial x} + \beta_y\rho v \frac{\partial u}{\partial y} = &- \frac{\partial}{\partial x}(\beta_x P) \\
&+ \frac{\partial}{\partial y}\left[\beta_y\left(\mu \frac{\partial u}{\partial y} - \overline{\rho u'v'}\right)\right] \\
&- \frac{1}{2}\rho C_D d(y) \frac{u^2}{L^2}
\end{aligned} \tag{20}$$

and

$$\begin{aligned}
\beta_x\rho u \frac{\partial H}{\partial x} + \beta_y\rho v \frac{\partial H}{\partial y} = &\frac{\partial}{\partial y}[\beta_y\{\frac{K}{C_p}\frac{\partial H}{\partial y} - \overline{\rho u'h'}]] \\
&+ u \frac{\partial}{\partial x}[\beta_x P] + \beta_y \frac{\partial u}{\partial y}[\mu \frac{\partial u}{\partial y} - \overline{\rho u'v'}] \\
&+ \frac{1}{2}\rho C_D \frac{d(y)}{L^2} u^3 \\
&+ \pi \frac{K Nu_d}{L^2}(T_R - T)
\end{aligned} \tag{21}$$

Examination of equations (20) and (21) shows that empirical models for $-\overline{\rho u'v'}$, $-\overline{\rho v'h'}$, and the roughness element drag coefficient C_D and Nusselt number Nu_d are necessary for closure.

The blockage parameters β_x and β_y and the element shape descriptor d(y) require no empirical fluid mechanics input as they are determined solely from the geometry of the rough surface. Taylor et al. 1984 [49] have shown for uniform three-dimensional roughness elements with circular cross-section that

$$\beta_x = \beta_y = 1 - \frac{\pi d^2}{4L^2} \tag{22}$$

The boundary conditions for the discrete element approach for rough wall flows are identical to those for smooth wall flows. The wall location ($y = 0$) is the smooth surface on which the roughness elements occur. At $y = 0$, $u = v = 0$ and $H = H_w$. As $y \to \infty$, $u \to U_\infty$ and $H \to H_\infty$.

The "wall shear stress" is defined as the sum of the shear and drag forces on the wall in the mean flow direction divided by the plan area of the wall. The corresponding skin friction coefficient is then

$$C_f = \frac{(\beta_y)_w \, \mu \left.\frac{\partial u}{\partial y}\right|_w + \frac{1}{2}\frac{1}{L^2}\int_0^\infty (\rho d C_D u^2)\, dy}{\frac{1}{2}\rho_\infty U^2_\infty} \tag{23}$$

and the Stanton Number is

$$St = \frac{-(\beta_y)_w \left.\frac{K}{C_p}\frac{\partial H}{\partial y}\right|_w + \frac{\pi}{L^2}\int_0^\infty [K Nu_d (T_R - T)]dy}{\rho_\infty U_\infty (H_w - H_{0,\infty})} \tag{24}$$

These definitions for C_f and St can be formulated from physical reasoning. However, they also arise naturally from equations (19) -(21) in the formulation of the integral boundary layer equations using the discrete element model.

In order to solve equations (19), (20) and (21), turbulence models for $-\overline{\rho u'v'}$ and $-\overline{\rho v'h'}$ and roughness models for C_D and Nu_d are required. Because of its wide acceptance and proven predictive capability for boundary layer flows over smooth surfaces, the Prandtl mixing length model with van Driest damping and a constant turbulent Prandtl number is used for turbulence closure. Thus

$$-\overline{\rho u'v'} = \rho \ell_m^2 \left(\frac{\partial u}{\partial y}\right)\left|\frac{\partial u}{\partial y}\right| \tag{25}$$

where

$$\ell_m = 0.40y[1 - \exp(-y^+/26)] \; ; \; \ell_m < 0.09\delta \qquad (26)$$

$$\ell_m = 0.09\delta; \text{ otherwise,} \qquad (27)$$

and

$$Pr_t = 0.9 \qquad (28)$$

The authors, as did Lin and Bywater 1980 [50], chose to formulate the C_D and Nu_d models as functions of the local element Reynolds number

$$Re_d = u(y)d(y)/\nu \qquad (29)$$

which includes roughness element size and shape information through d(y). The general shape of the drag coefficient and Nusselt number versus Reynolds number curves of Zukauskas 1972 [51] were used as starting points to determine the final expressions for C_D and Nu_d through comparison with calibration data sets from well-defined rough surfaces. As discussed in Taylor et al. 1984 [49], the model which gave the best overall agreement was

$$\left.\begin{array}{ll} \log C_D = -0.125 \log (Re_d) + 0.375 & Re_d < 6 \times 10^4 \\ C_D = 0.6 & Re_d \geq 6 \times 10^4 \end{array}\right\} \qquad (30)$$

$$\left.\begin{array}{ll} Nu_d = 2.475\, Re_d^{0.4} Pr^{0.36}; & Re_d < 100 \\ Nu_d = 1.043\, Re_d^{0.5} Pr^{0.37}; & 100 < Re_d < 1000 \\ Nu_d = 0.963\, Re_d^{0.6} Pr^{0.36}; & 1000 < Re_d < 200{,}000 \end{array}\right\} \qquad (31)$$

The C_D model has been tested for values of Re_d up to about 25,000 (Taylor, et al. 1984 [49]) and up to about 17,000 (Scaggs et al. 1988 [21]). The Nu_d model has been tested for values of Re_d up to about 1000 (Taylor et al. 1984 [49]) and has been extended up to about 2400 in this report.

6.2 HEAT TRANSFER RESULTS

One of the most important aspects of this research program is the development of boundary layer heat transfer data which can be used to formulate and refine predictive models. Stanton number results have been obtained for freestream velocities of 6, 12, 28, 43, 58, and 67 m/s on the rough surface composed of 1.27 mm diameter hemispheres spaced in a staggered array 4 diameters apart. In addition, mean temperature profiles have been obtained at $U_\infty = 12$ m/s.

Figure 43 shows a composite plot of the Stanton number data for this surface. The error bars on selected points indicate the uncertainties as computed using the techniques discussed in Appendix I. The curve represents smooth wall results as given by equation (5). Figure 44 shows the Stanton number data plotted versus Δ_2/k where Δ_2 is the enthalpy thickness and k is the roughness height. Pimenta 1975 [13] found that for the Stanford surface (1.27 mm diameter spheres packed in the most dense array), Stanton number data plotted in these coordinates fell on a single curve for boundary layers in the fully rough regime. Inspection of the figure shows that as the freestream velocity increases the data approach a single curve, with the data for $U_\infty = 58$ m/s and 67 m/s essentially coinciding. Based on this criteria the boundary layer on this surface would be considered to be in the transitionally rough regime for the lower freestream velocities and in the fully rough regime for $U_\infty = 58$ m/s and 67 m/s. More discussion of the transitionally rough and fully rough regimes will be given later when the measurements in the momentum boundary layer are discussed.

In Figures 45-50, the Stanton number data sets are compared with predictions made with the discrete element method discussed previously. That model was used without any modification; therefore, these computations are true predictions. For the lowest velocity, $U_\infty = 6$ m/s, the computations underpredict the data. For the intermediate velocities--12, 28, and 43 m/s--the predictions agree almost exactly with the data. For the higher velocities, $U_\infty = 58$ and 67 m/s, the computations overpredict the data, but only by about 5 to 8%.

Figure 51 shows a plot of a typical temperature profile for $U_\infty = 12$ m/s in T^+ versus y^+ coordinates. The symbols represent the measurements over the rough surface and the solid line represents the temperature "law-of-the-wall" for smooth surfaces

$$T^+ = 2.195 \ln y^+ + 13.2 \, Pr - 5.66 \qquad (32)$$

The comparison indicates, as expected, a downward shift in the temperature profile for the rough wall data.

6.3 FLUID DYNAMICS RESULTS

Fluid dynamics data have been obtained in the boundary layer for freestream velocities of 12 and 58 m/s. The data were obtained with the hot wire probes using the techniques discussed in Appendices II and III. The data include distributions of skin friction coefficient along the surface and profiles of mean velocity and Reynolds stress quantities.

Figure 52 shows a plot of skin friction coefficient versus Reynolds number based on momentum thickness, Re_{δ_2}, for $U_\infty = 12$ and 58 m/s. The error bars represent the estimated ± 10% uncertainty in C_f. The curves represent the predictions using the discrete element model and the smooth wall correlation, equation (3). Comparison of the data and predictions shows that the agreement is excellent, with the predictions agreeing with the data within the uncertainty. Such agreement is not surprising, since the roughness element drag coefficient model in the discrete element approach has been verified using a very wide range of data (Scaggs, Taylor and Coleman 1988 [21]).

Figure 53 shows a typical mean velocity profile in u^+ versus y^+ coordinates for $U_\infty = 12$ m/s. The symbols represent the data and the line represents the usual smooth wall "law-of-the-wall"

$$u^+ = 2.5 \ln y^+ + 5.5 \qquad (33)$$

As in the case of the temperature profile, the expected downward shift from the smooth wall case is observed.

In addition to the mean velocity profiles, measurements of profiles of the Reynolds stress quantities $\overline{u'^2}$, $\overline{v'^2}$, $\overline{w'^2}$, and $\overline{u'v'}$ were made. Figure 54 shows the profile of $(\overline{u'^2})^{1/2}/u^*$ versus y/δ for $U_\infty = 12$ m/s. The profile shows a behavior which is very similar to the profile over a smooth surface. Figure 55 shows a composite plot for all three Reynolds normal stress components. The behavior observed in these two figures indicates that the peak value of turbulent kinetic energy occurs very close to the wall. This is a strong indication that the boundary layer is in the transitionally rough regime, Pimenta 1975 [13]. Figure 56 shows the measured Reynolds shear stress profile, which behaves as expected. Figure 57 shows a plot of $(\overline{u'^2})^{1/2}/u^*$ versus y/δ for $U_\infty = 58$ m/s. The figure shows a profile that is typical of fully rough boundary layers, Pimenta 1975 [13]. The peak in the turbulence intensity has moved to a distance that is further from the wall and is much broader.

A measure of the state of the boundary layer flow (aerodynamically smooth, transitionally rough, or fully rough) which was proposed by Taylor et al. 1984 [49] is the ratio

$$R_\tau = \frac{\tau_r}{\tau_{tot}} \qquad (34)$$

where τ_r is the part of the apparent total surface shear stress, τ_{tot}, caused by the drag on the roughness elements as computed using the discrete element method. Scaggs et al. 1988 [21] suggested that values of R_τ between about 0.1 and 0.6 indicate a transitionally rough flow. For a freestream velocity of 12 m/s the computed values of R_τ are about 0.4, indicating a transitionally rough flow. For $U_\infty = 58$ and 67 m/s $R_\tau = 0.6$, indicating that these flows should be approaching fully rough behavior. These conclusions are consistent with the observations of the Stanton number data and the turbulence profiles.

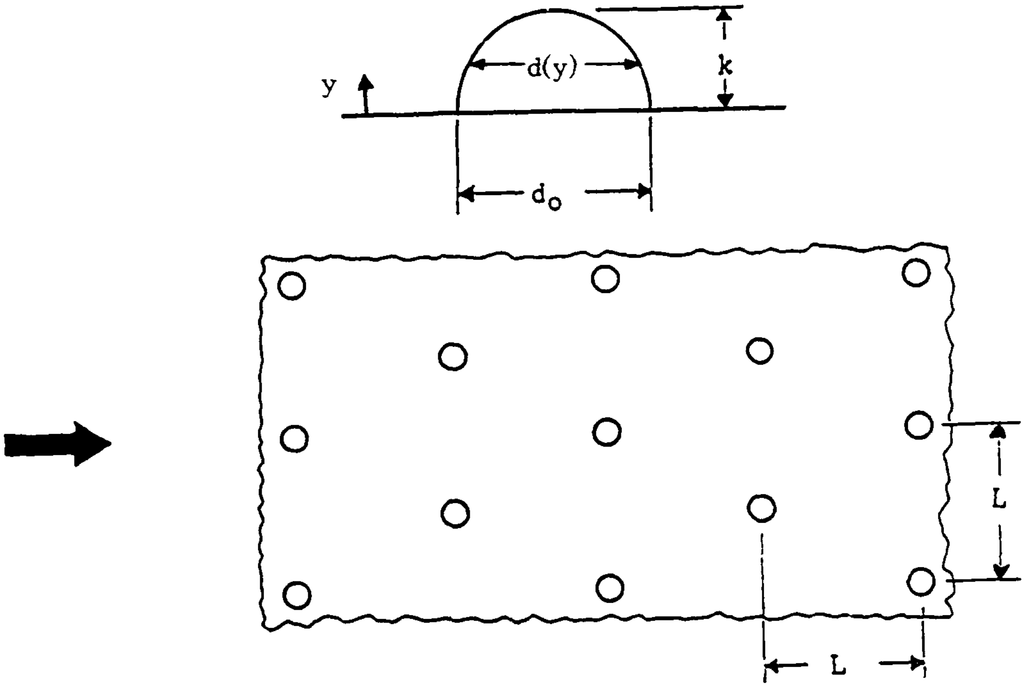

Figure 41. Surface Roughness Geometry.

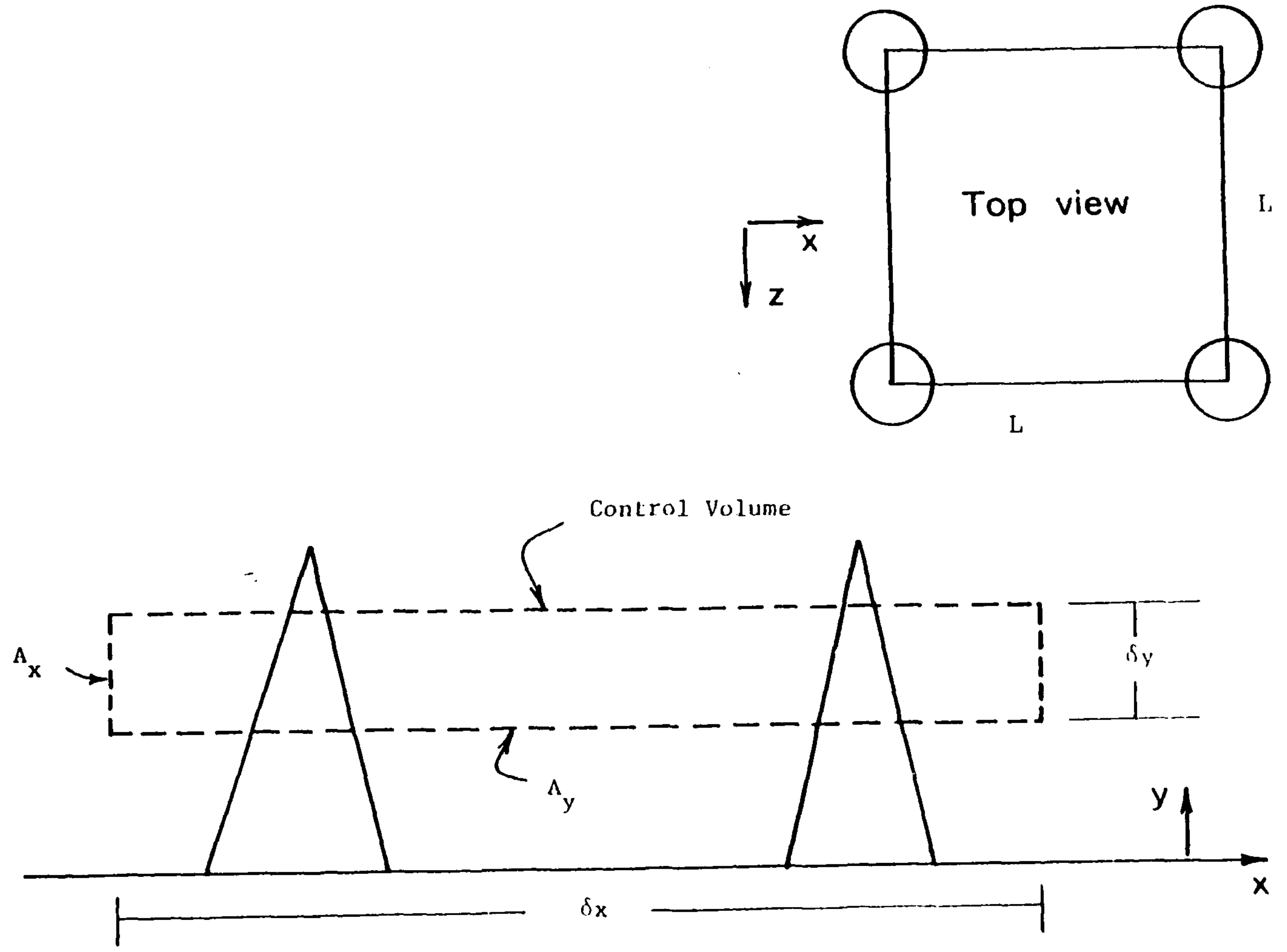
Top view
L
L
x
z
Control Volume
A_x
A_y
δy
y
x
δx

Figure 42. General Layout of Control Volume.

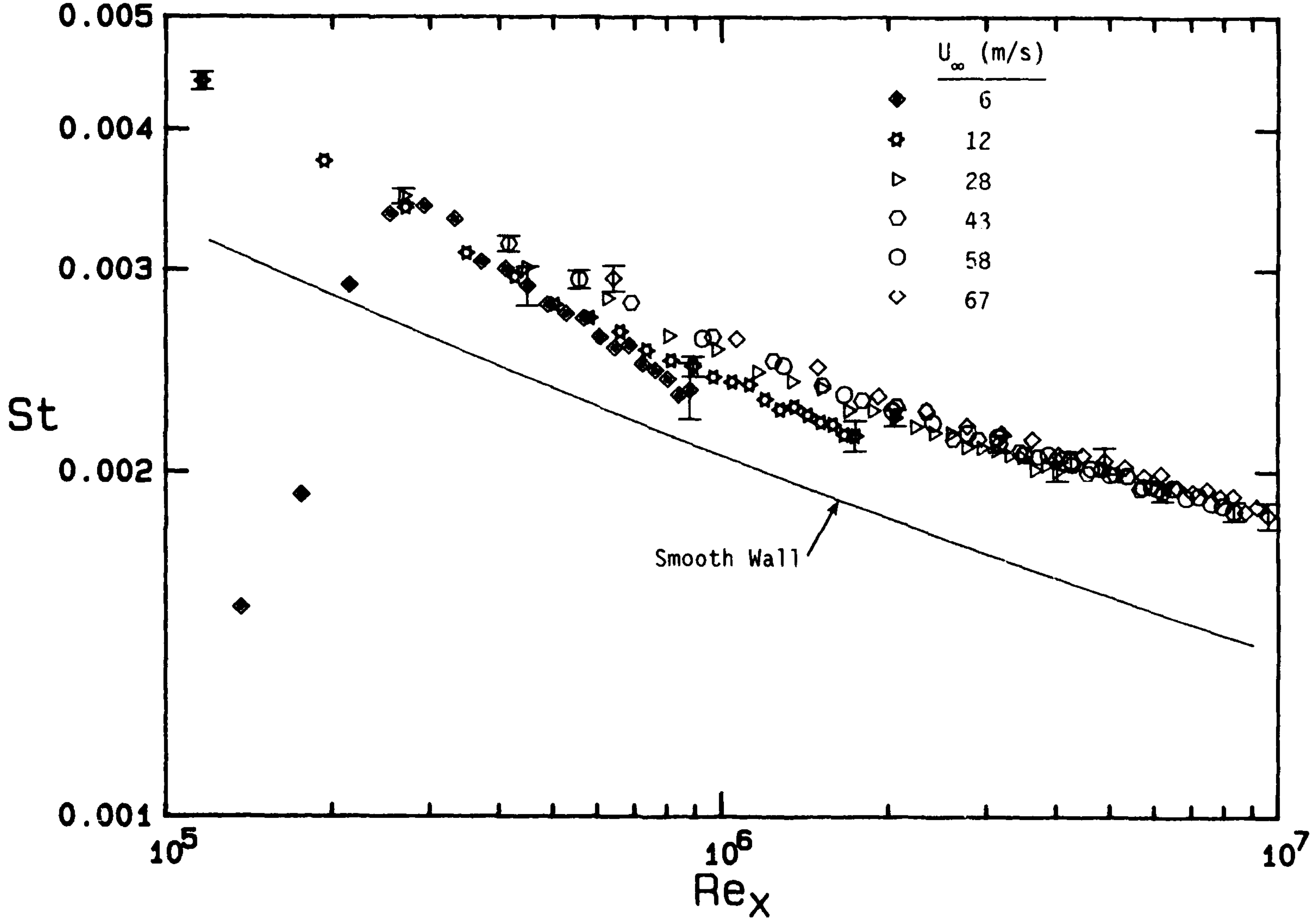

Figure 43. Composite Plot of Rough Wall Stanton Number Data vs. x-Reynolds Number.

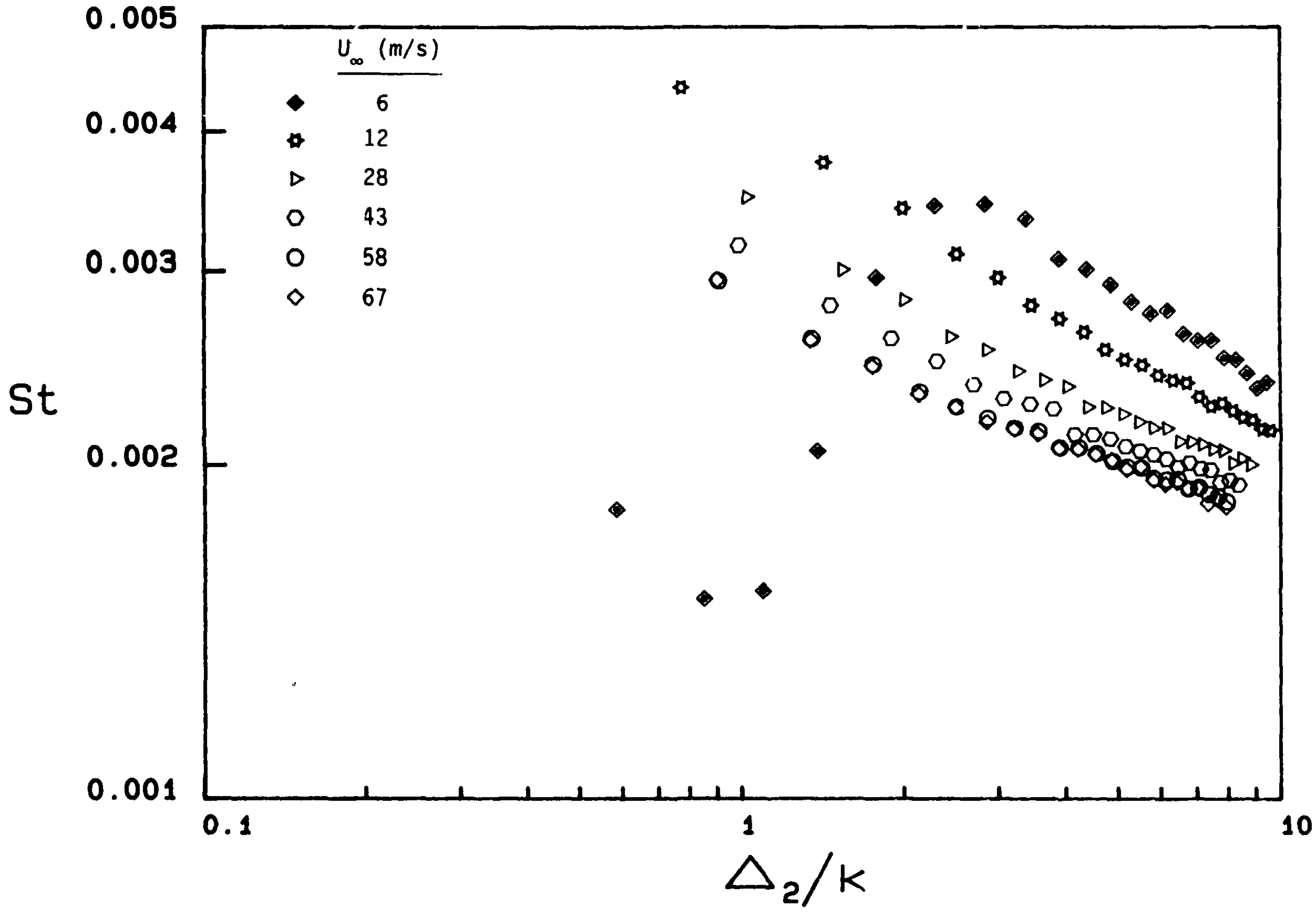

Figure 44. Composite Plot of Rough Wall Stanton Number Data vs. Enthalpy Thickness Normalized by the Roughness Element Height.

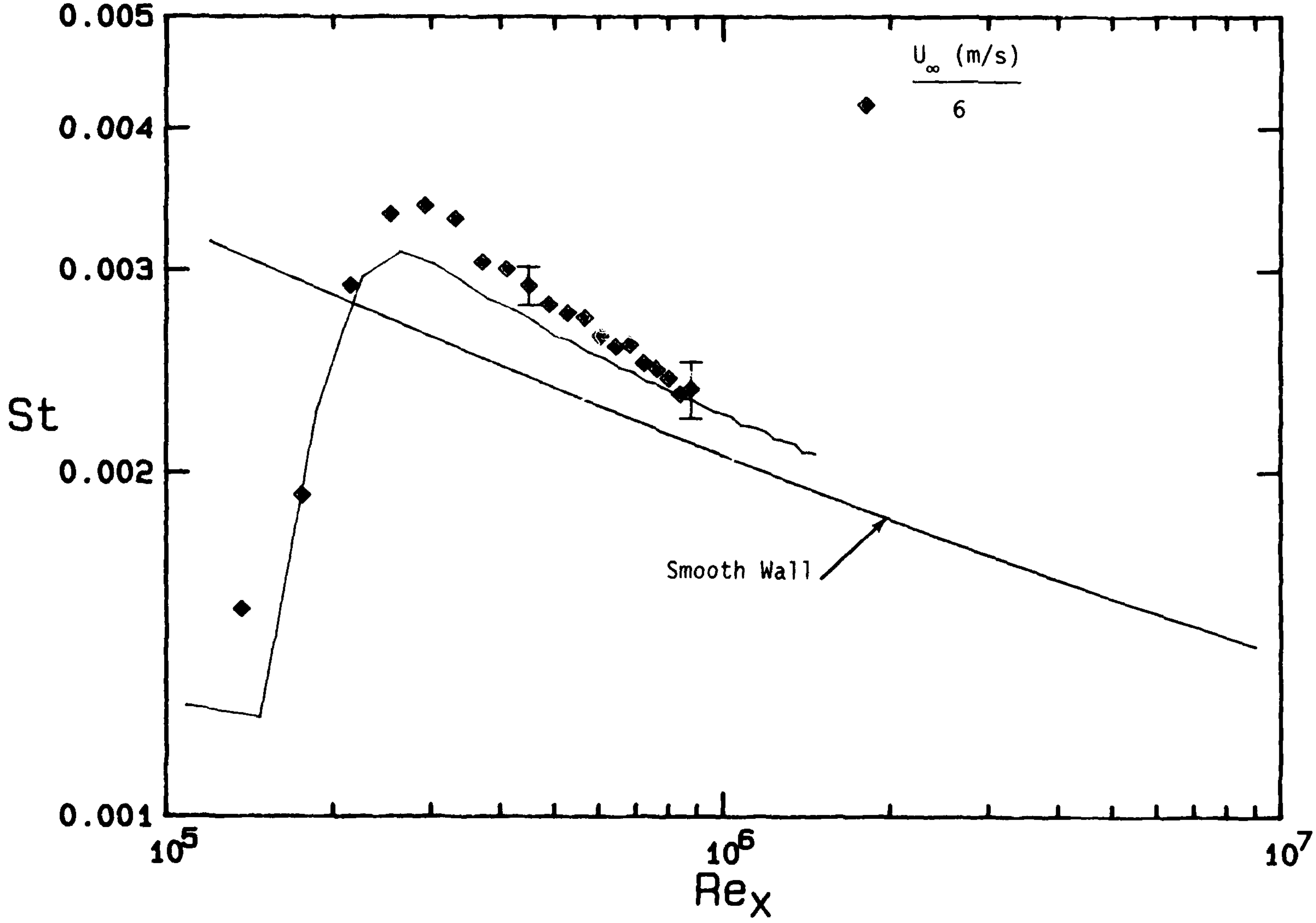

Figure 45. Rough Wall Stanton Number Data at a Freestream Velocity of 6 m/s Compared with the Prediction from the Discrete Element Method.

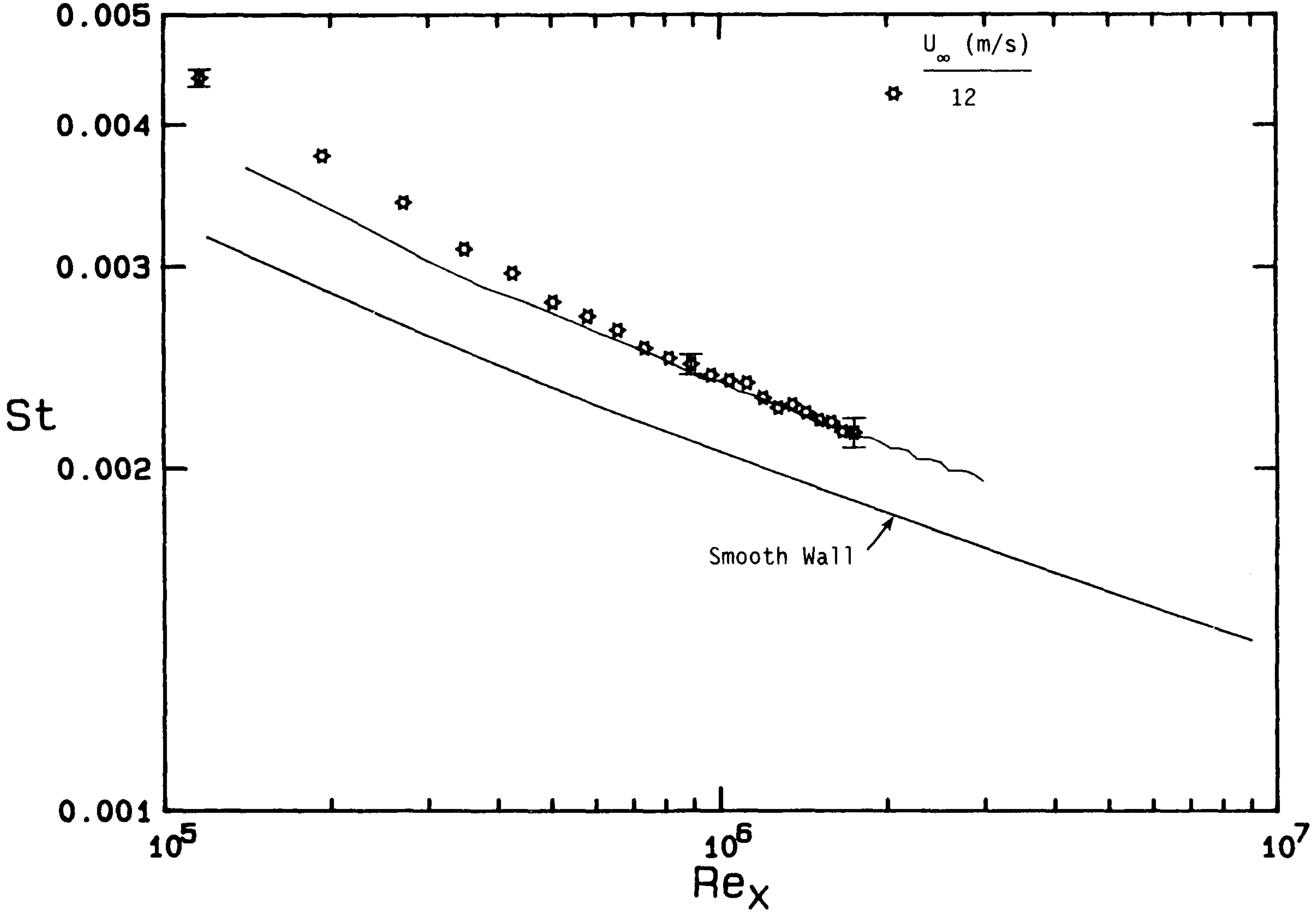

Figure 46. Rough Wall Stanton Number Data at a Freestream Velocity of 12 m/s Compared with the Prediction from the Discrete Element Method.

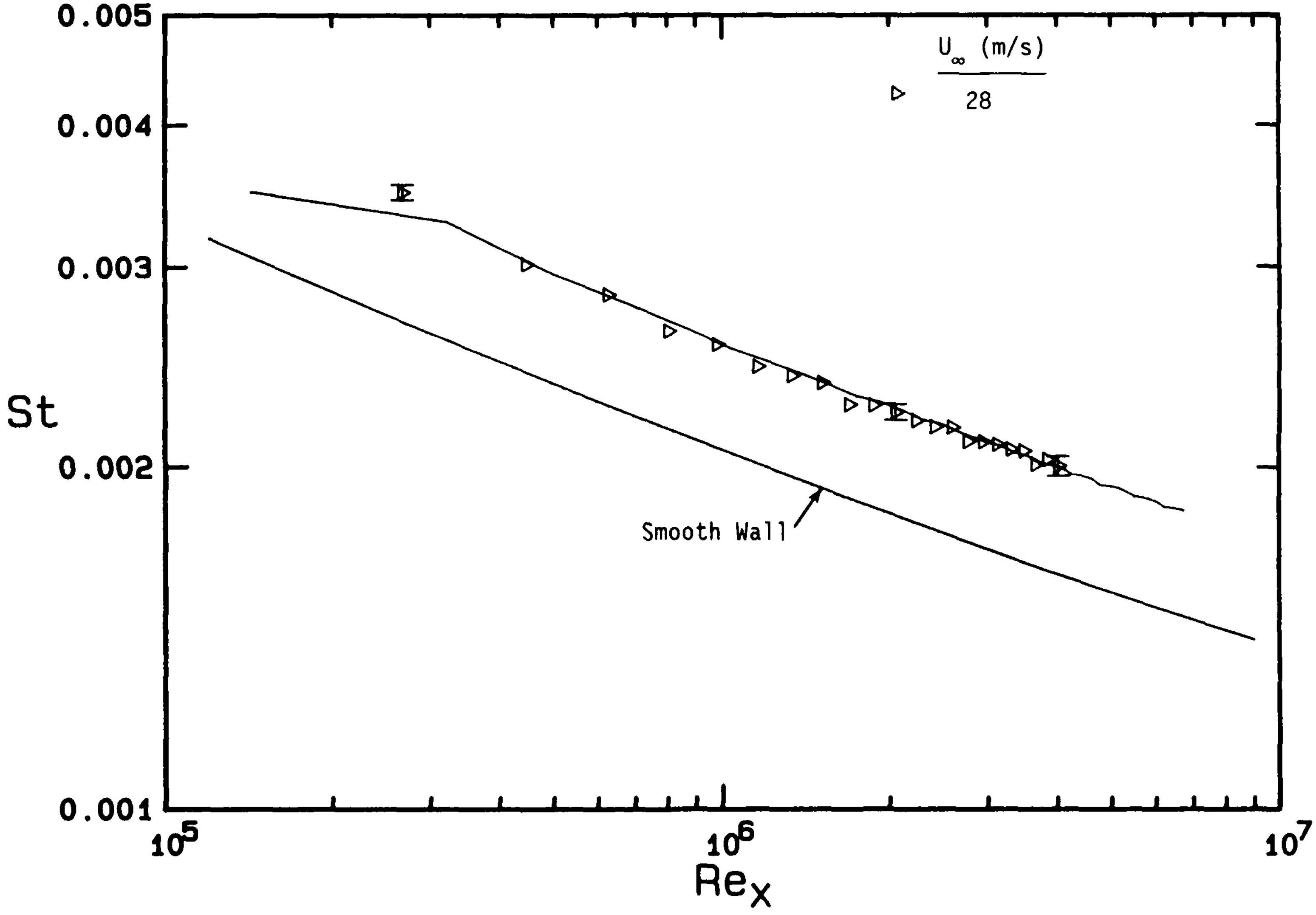

Figure 47. Rough Wall Stanton Number Data at a Freestream Velocity of 28 m/s Compared with the Prediction from the Discrete Element Method.

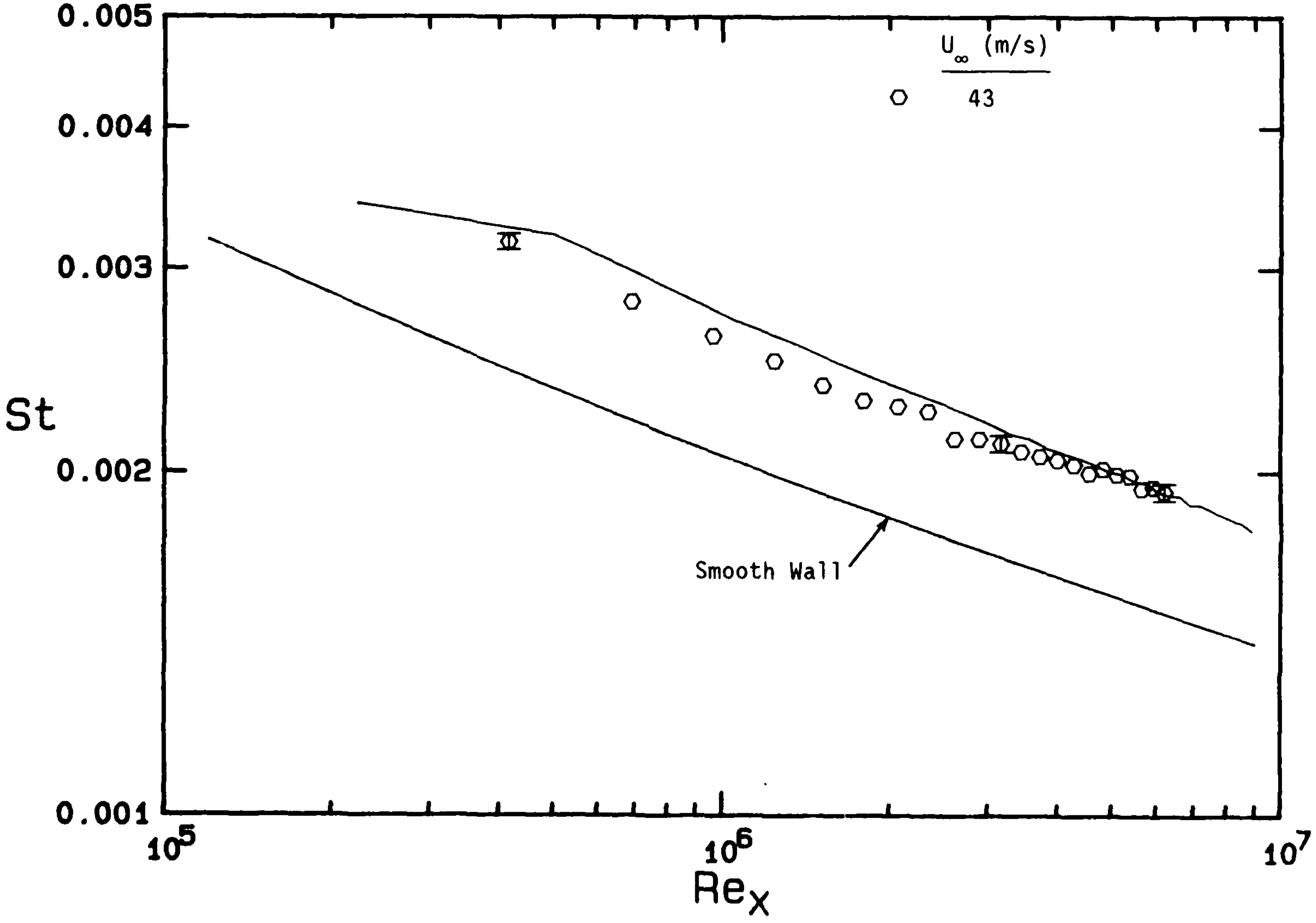

Figure 48. Rough Wall Stanton Number Data at a Freestream Velocity of 43 m/s Compared with the Prediction from the Discrete Element Method.

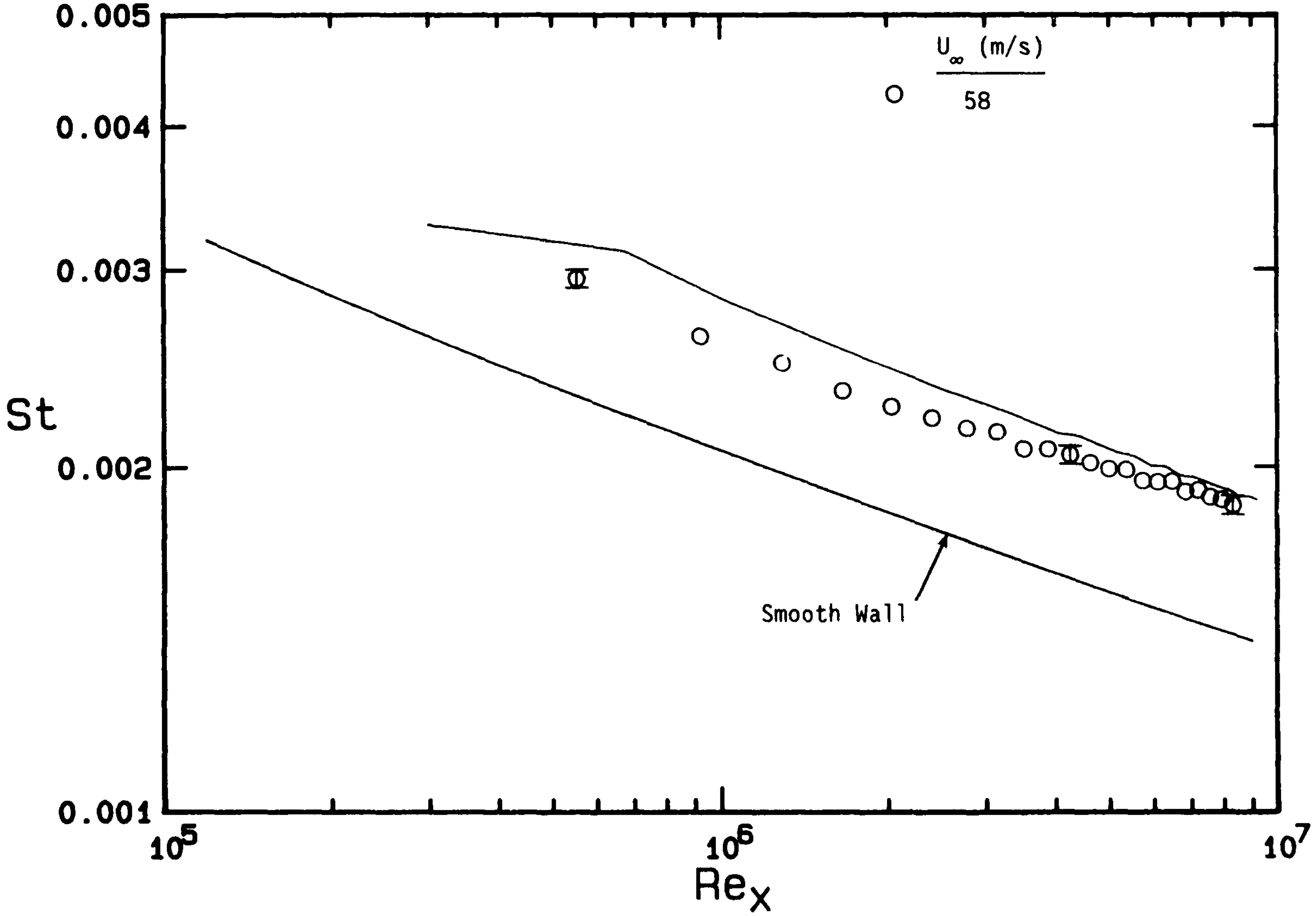

Figure 49. Rough Wall Stanton Number Data at a Freestream Velocity of 58 m/s Compared with the Prediction from the Discrete Element Method.

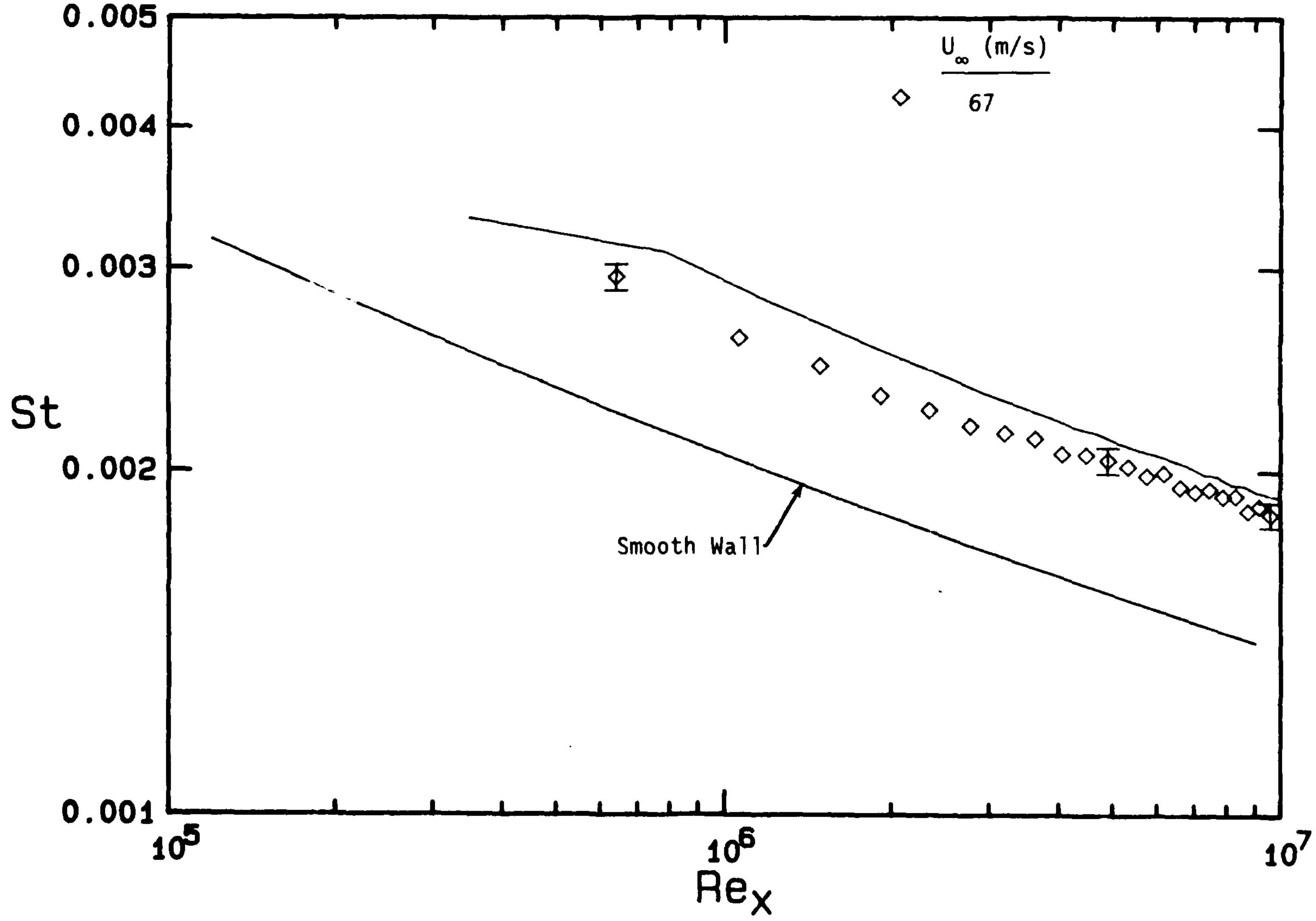

Figure 50. Rough Wall Stanton Number Data at a Freestream Velocity of 67 m/s Compared with the Prediction from the Discrete Element Method.

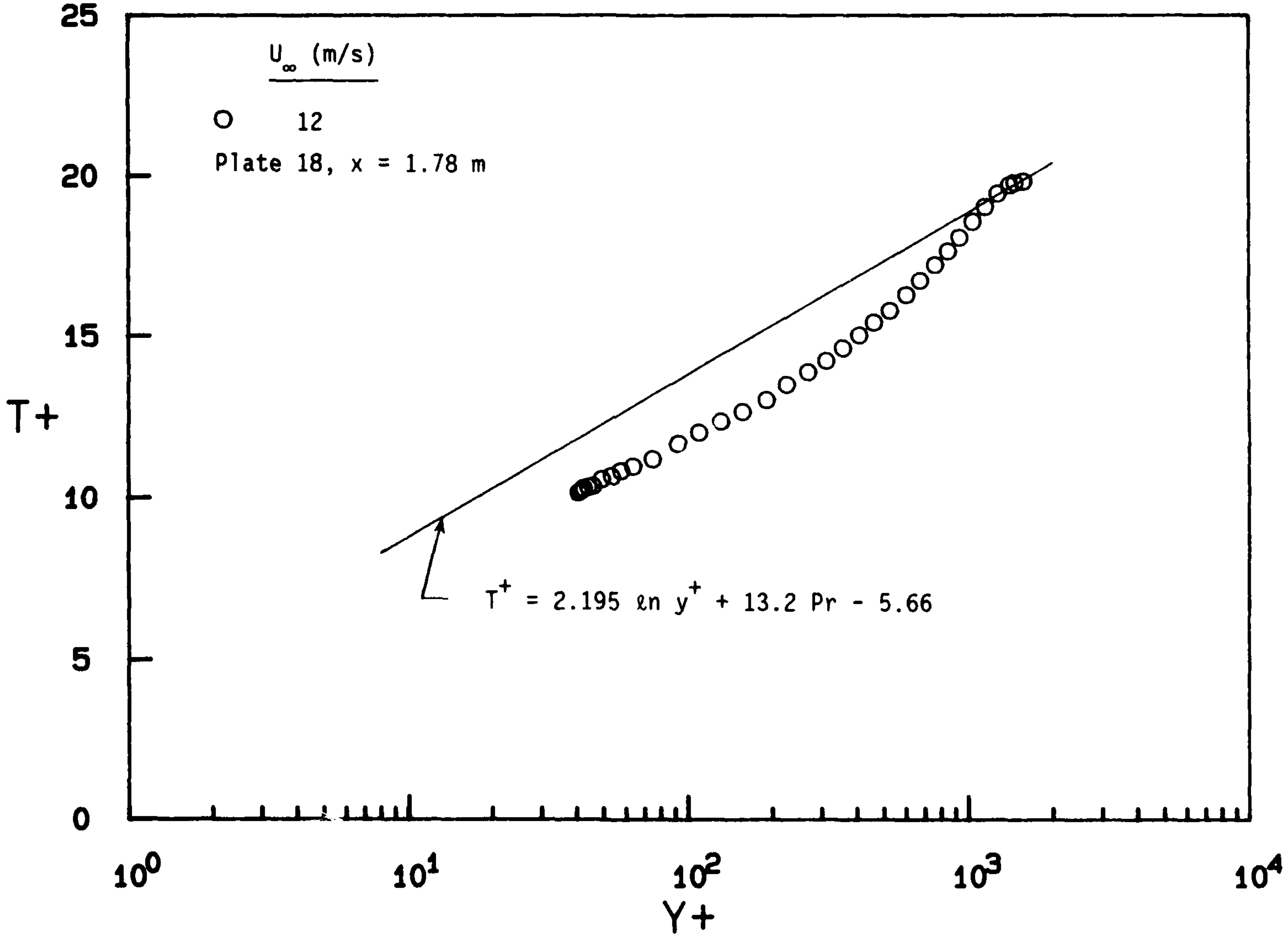

Figure 51. Rough Wall Temperature Profile Compared with the Smooth Wall Law of the Wall.

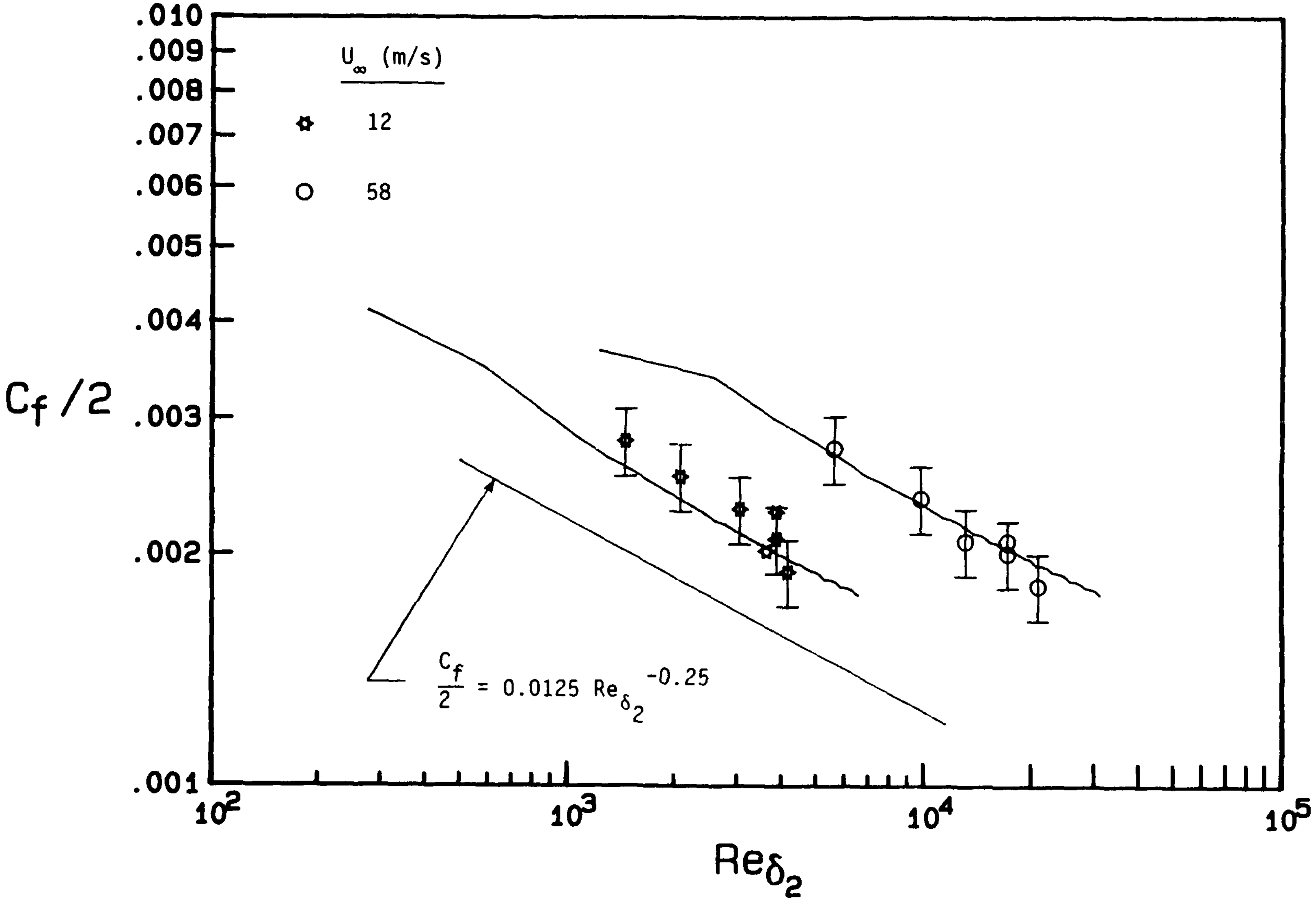

Figure 52. Rough Wall Skin Friction Coefficient Distributions Compared with Predictions from the Discrete Element Method.

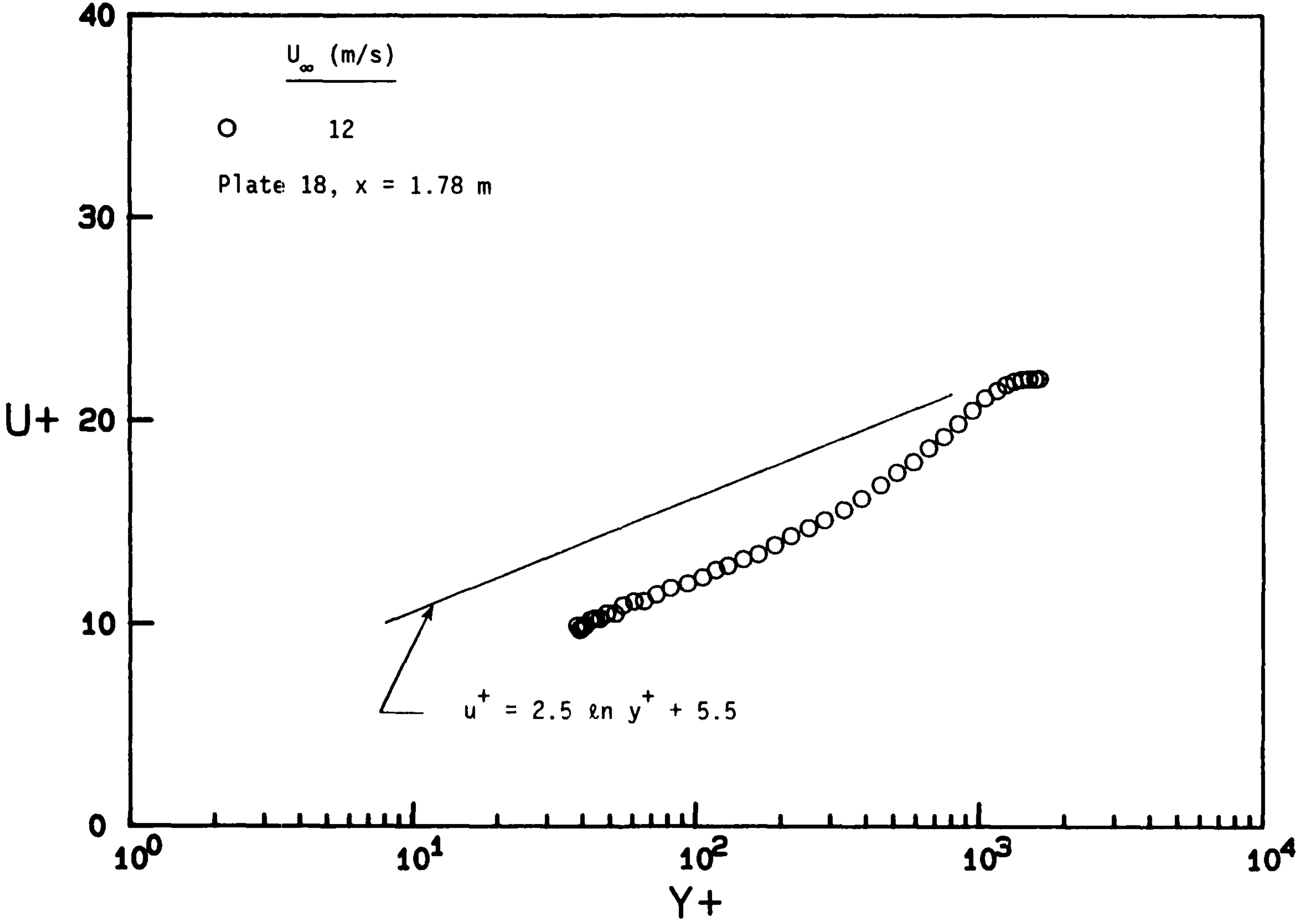

Figure 53. Rough Wall Velocity Profile Compared with the Smooth Wall Law of the Wall.

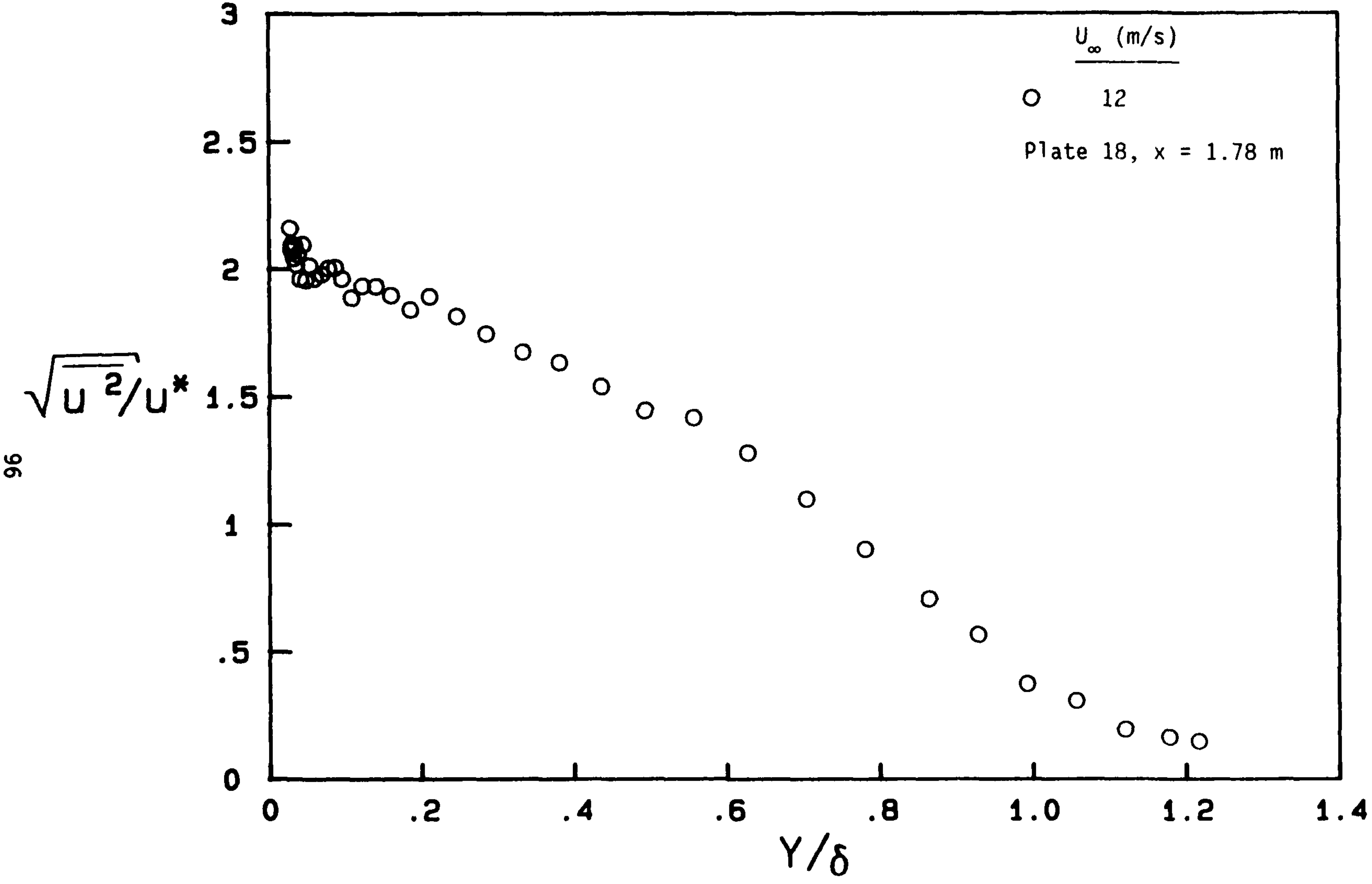

Figure 54. Rough Wall Axial Turbulence Intensity Profile for a Freestream Velocity of 12 m/s.

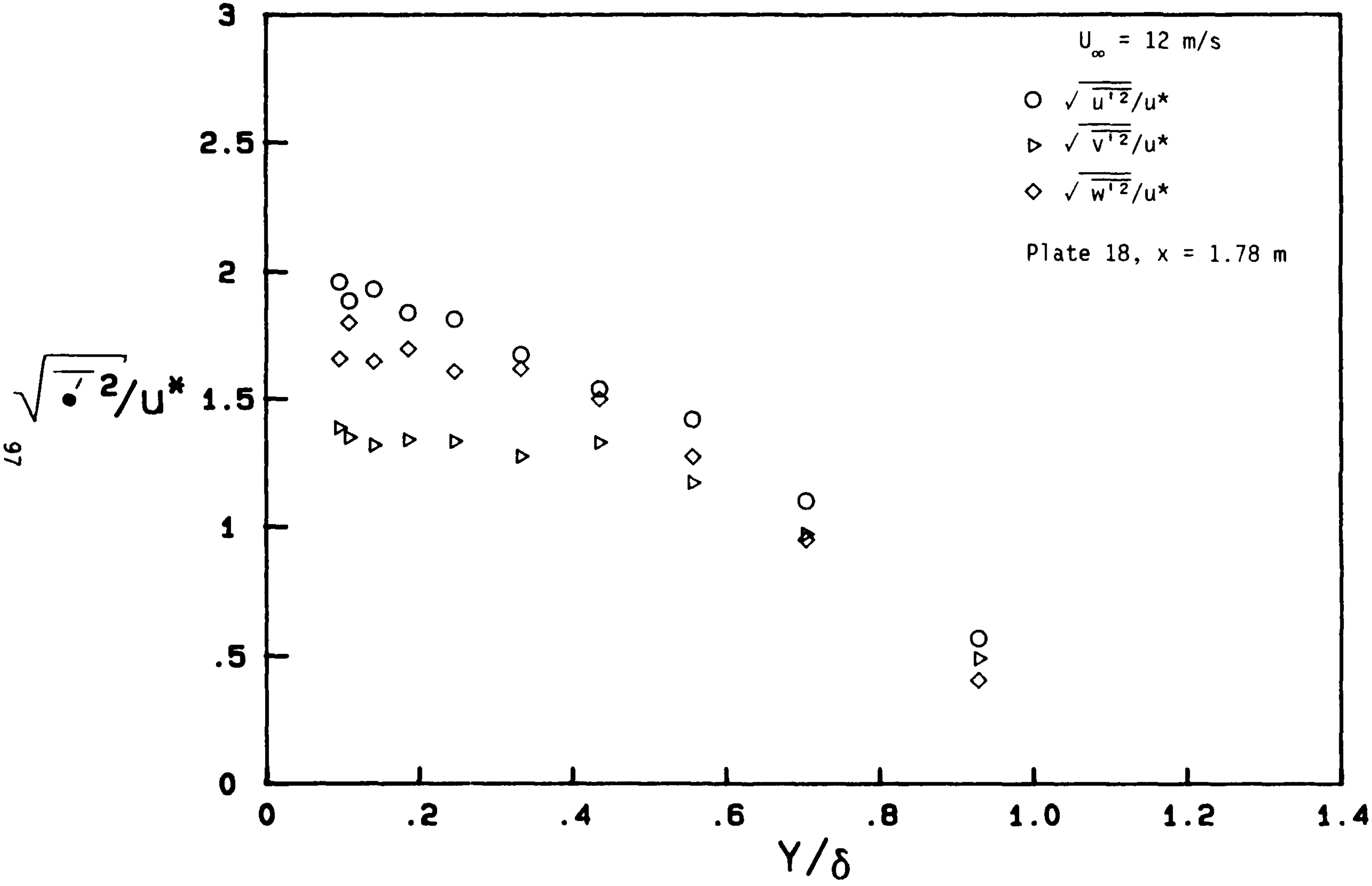

Figure 55. Rough Wall Profiles of the Three Normal Reynolds Stresses.

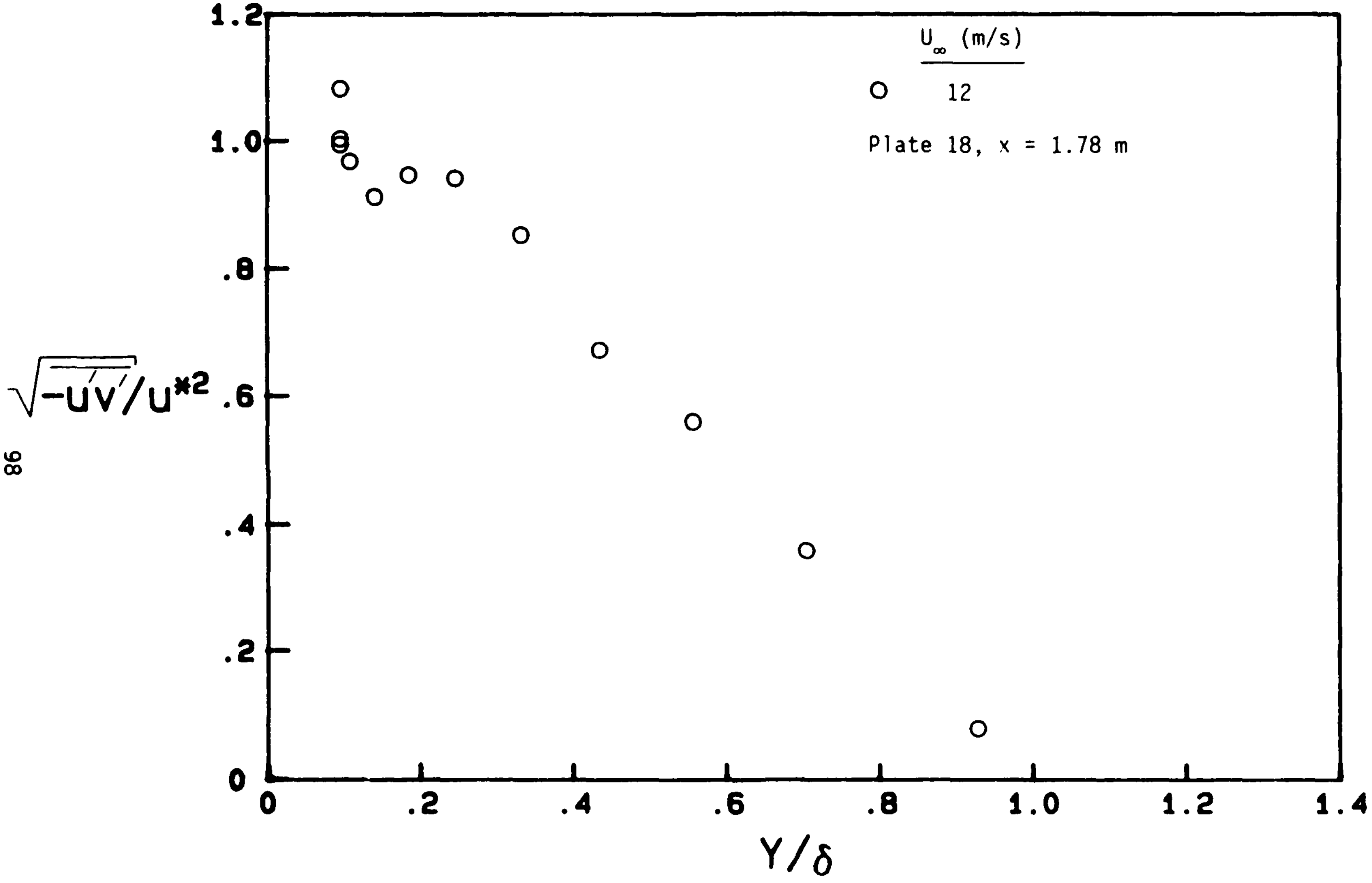

Figure 56. Rough Wall Reynolds Shear Stress Profile.

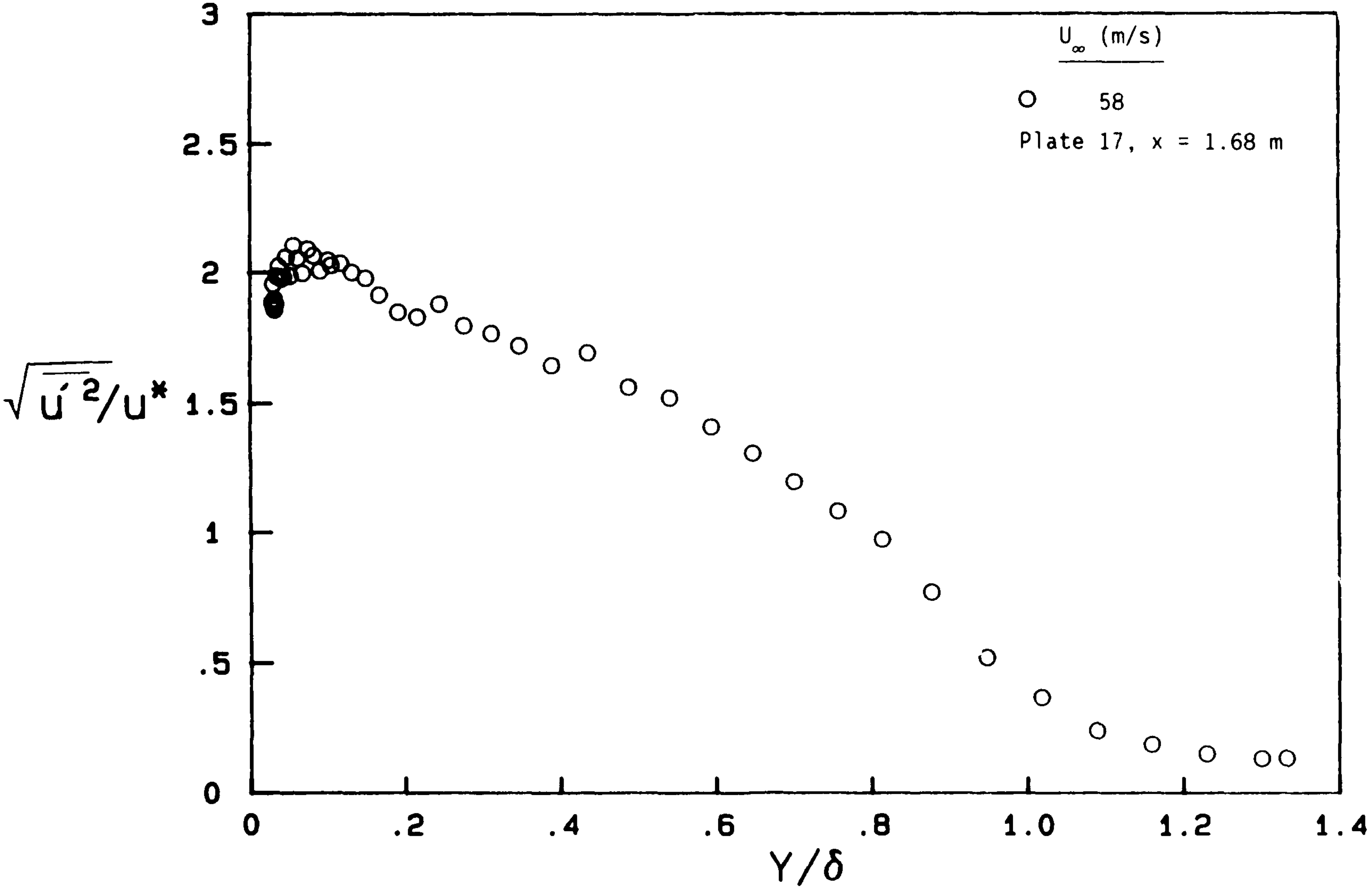

Figure 57. Rough Wall Axial Turbulence Intensity Profile for a Freestream Velocity of 58 m/s.

SECTION 7

SUMMARY

In this report, the uncertainty analysis, design, and qualification of the Turbulent Heat Transfer Test Facility (THTTF) with a smooth wall test section have been presented, and the initial results for a wall roughened with hemispherical elements spaced four base diameters apart have been discussed and compared with calculations from the discrete element prediction method.

A detailed description of the THTTF itself was provided in Section 2. Discussions of details of the instrumentation systems, calibration procedures and uncertainties associated with the measurements have been documented in Appendices I-III.

The smooth wall fluid dynamics data, presented in Section 3, showed that the facility was operating within the expected bounds over the Reynolds number range anticipated in future rough surface testing. Skin friction coefficient determinations from both the Preston tube method and the hot-wire method showed excellent agreement with the Schultz-Grunow correlation, which is generally accepted as representing smooth wall turbulent skin friction data very well. The agreement shown by the skin friction coefficients determined using the hot-wire method was especially important, since that is the technique which is used in rough wall tests. Also, the behavior of the hot-wire data was consistent with the 10-12% estimate of the uncertainty in skin friction coefficients determined using that method.

The baseline smooth wall heat transfer data, presented in Section 4, showed that the qualification of the THTTF was completed and successful for x-Reynolds numbers up to 10 million. Stanton numbers determined using the energy balance technique were in excellent agreement with previous smooth wall data for a constant wall temperature boundary condition, which had been reported up to x-Reynolds numbers of 3.5 million. To the authors' knowledge, no smooth wall Stanton number data has been reported previously in the

3.5-10 million range covered by the THTTF data. Stanton numbers are determined in the THTTF to uncertainties of 2-5%, depending on flow conditions.

Presented in Section 5 were smooth wall Stanton number data taken for other thermal boundary conditions: (1) constant heat flux, (2) step wall temperature, (3) step wall heat flux, (4) linear variations in wall temperature, and (5) bi-linear variations in wall temperature. These data were the first to be reported, to the authors' knowledge, in such an extended x-Reynolds number range.

Presented in Section 6 were the initial rough wall data taken using the THTTF. These data were for a surface roughened with hemispherical elements spaced four base diameters apart. The Stanton number and skin friction coefficient data were compared with predictions from the discrete element method using unmodified the roughness models developed previous to this effort. The skin friction predictions were in excellent agreement with the data. This was not surprising considering the large size of the data base on which the roughness element drag coefficient model had been developed. The heat transfer predictions were in reasonably good agreement with the Stanton number data, although improvement would be desirable. Since the roughness element Nusselt number model was developed based on heat transfer data from the single rough surface used in the Stanford studies, it is encouraging that the heat transfer predictions are as good as they are. Further development of the roughness element Nusselt number model will be made when data are taken on additional rough surfaces in the THTTF.

REFERENCES

1. Schlichting, H. (1936), "Experimentelle Untersuchungen Zum Rauhigkeits-Problem," Ingenieur-Archiv., Vol. VII, No. 1, pp. 1-34. (Also Experimental Investigation of the Problem of Surface Roughness, NACA TM 832).

2. Nikuradse, J. (1933), "Stromungsgesetze in Rauhen Rohren," VDI-Forchungsheft 361. (Also Laws of Flow in Rough Pipes, NACA TM 1292.)

3. Finson, M. L. (1975), "A Reynolds Stress Model for Boundary Layer Transition with Applications to Rough Surfaces," AFOSR-TR-76-0322.

4. Adams, J. C. and Hodge, B. K. (1977), "The Calculation of Compressible Transitional Turbulent and Relaminarizational Boundary Layers over Smooth and Rough Surfaces Using an Extended Mixing-Length Hypothesis," AIAA Paper 77-682.

5. Finson, M. L. and Wu, P. K. S. (1979), "Analysis of Rough Wall Turbulent Heating with Applications to Blunted Flight Vehicles," AIAA Paper 79-008.

6. Finson, M. L. and Clark, A. S. (1980), "The Effects of Surface Roughness Character on Turbulent Reentry Heating," AIAA Paper 80-1459.

7. Lin, T. C. and Bywater, R. J. (1980), "The Evaluation of Selected Turbulence Models for High-Speed Rough Wall Boundary Layer Calculations," AIAA Paper 80-0132.

8. Finson, M. L. (1982), "A Model for Rough Wall Turbulent Heating and Skin Friction," AIAA Paper 82-0199.

9. Coleman, H. W., Hodge, B. K. and Taylor, R. P. (1983), "Generalized Roughness Effects on Turbulent Boundary Layer Heat Transfer," AFATL-TR-83-90.

10. Taylor, R. P., Coleman, H. W. and Hodge, B. K. (1985), "Prediction of Turbulent Rough-Wall Skin Friction Using a Discrete Element Approach," Journal of Fluids Engineering, Vol. 107, pp. 251-257.

11. Coleman, H. W., Hodge, B. K. and Taylor, R. P. (1984), "A Reevaluation of Schlichting's Surface Roughness Experiment," Journal of Fluids Engineering, Vol. 106, pp. 60-65.

12. Healzer, J. M. (1974), "The Turbulent Boundary Layer on a Rough, Porous Plate: Experimental Heat Transfer with Uniform Blowing," Ph.D. Dissertation, Mech. Eng. Dept., Stanford Univ. (Also Report HMT-18).

13. Pimenta, M. M. (1975), "The Turbulent Boundary Layer: An Experimental Study of the Transport of Momentum and Heat with the Effect of Roughness," Ph.D. Dissertation, Mech. Eng. Dept., Stanford Univ. (Also Report HMT-21).

14. Coleman, H. W. (1976), "Momentum and Energy Transport in the Accelerated Fully Rough Turbulent Boundary Layer," Ph.D. Dissertation, Mech. Eng. Dept., Stanford Univ. (Also Report HMT-24).

15. Ligrani, P. M. (1979), "The Thermal and Hydrodynamic Behavior of Thick, Rough-Wall, Turbulent Boundary Layers," Ph.D. Dissertation, Mech. Eng. Dept., Stanford Univ. (Also Report HMT-29).

16. Holden, M. S. (1983), "Studies of Surface Roughness Effects in Hypersonic Flow," Calspan Report No. 7018-A-2, Advanced Technology Center, Buffalo, NY.

17. Scaggs, W. F. (1988), "Measurement and Prediction of Rough Wall Effects on Friction Factors in Turbulent Pipe Flow," M.S. Thesis, Mechanical and Nuclear Engineering Department, Mississippi State University.

18. Scaggs, W. F., Taylor, R. P. and Coleman, H. W. (1988), "Measurement and Prediction of Rough Wall Effects on Friction Factors in Turbulent Pipe Flow," Report TFD-88-1, Mech. and Nuc. Eng. Dept., Miss. State Univ.

19. Scaggs, W. F., Taylor, R. P. and Coleman, H. W. (1988), "Investigations of Rough Surface Effects on Friction Factors in Turbulent Pipe Flow," Final Technical Report to USAF Wright Aeronautical Laboratories, AFWAL-TR-87-3101.

20. Scaggs, W. F., Taylor, R. P. and Coleman, H. W. (1988), "Measurement and Prediction of Rough Wall Effects on Friction Factor - Uniform Roughness Results," *J. Fluids Engineering*, Vol. 110, pp. 385-391.

21. Taylor, R. P., Scaggs, W. F. and Coleman, H. W. (1988), "Measurement and Prediction of the Effects of Nonuniform Surface Roughness on Turbulent Flow Friction Coefficients," *J. Fluids Engineering*, Vol. 110, pp. 380-384.

22. Norton, B. A. (1983), "Preliminary Analysis and Design of a Turbulent Heat Transfer Test Apparatus," M.S. Thesis, Mechanical and Nuclear Engineering Department, Mississippi State University.

23. Suryananarayana, P. V. R. (1986), "Remote Data Acquisition and Control Techniques for Wind and Water Tunnel Experiments," M.S. Thesis, Mechanical and Nuclear Engineering Department, Mississippi State University.

24. Reynolds, W. C., Kays, W. M. and Kline, S. J. (1958), "Heat Transfer in the Turbulent Incompressible Boundary Layer, Parts I, II, and III," NASA MEMO 12-1-58W, 12-2-58W, and 12-3-58W.

25. Moffat, R. J. (1967), "The Turbulent Boundary Layer on a Porous Plate: Experimental Heat Transfer With Uniform Blowing and Suction," Ph.D. Dissertation, Mech. Eng. Dept., Stanford Univ.

26. Kearney, D. W. (1970), "The Turbulent Boundary Layer: Experimental Heat Transfer With Strong Favorable Pressure Gradients and Blowing," Ph.D. Dissertation, Mech. Eng. Dept., Stanford Univ. (Also Report HMT-12).

27. Orlando, A. F. (1974), "Turbulent Transport of Heat and Momentum in a Boundary Layer Subject to Deceleration, Suction and Variable Wall Temperature," Ph.D. Dissertation, Mech. Eng. Dept., Stanford Univ. (Also Report HMT-17).

28. Mehta, R. D. and Hoffmann, P. H. (1987), "Boundary Layer Two-Dimensionality in Wind Tunnels," Experiments in Fluids, Vol. 5, pp. 358-360.

29. Schultz-Grunow, F. (1941), "New Frictional Resistance Law for Smooth Plates," NACA TM 986, Washington, DC.

30. Schlichting, H. (1979), Boundary Layer Theory, 7th edition, McGraw-Hill, New York, NY.

31. Kays, W. M. and Crawford, M. E. (1980), Convective Heat and Mass Transfer, 2nd edition, McGraw-Hill, New York, NY.

32. Klebanoff, P. S. (1955), "Characteristics of Turbulence in a Boundary Layer with Zero Pressure Gradient," NACA TR 1247, Washington, DC.

33. Laufer, J. (1954), "The Structure of Turbulence in Fully Developed Pipe Flow," NACA Rep. 1174, Washington, DC.

34. Ligrani, P. M. and Bradshaw, P. (1987), "Spatial Resolution and Measurement of Turbulence in the Viscous Sublayer Using Subminiature Hot-Wire Probes," Experiments in Fluids, Vol. 5, pp. 407-417.

35. Rohsenow, W. M. and Hartnett, J. P. (1973), Handbook of Heat Transfer, McGraw-Hill, New York, NY.

36. Moffat, R. J. (1988), "Describing the Uncertainties in Experimental Results," Experimental Thermal and Fluid Science, Vol. 1, pp. 3-17.

37. Coleman, H. W. and Steele, W. G. (1989), Experimentation and Uncertainty Analysis, John Wiley, New York, NY.

38. Cebeci, T. and Bradshaw, P. (1984), Physical and Computational Aspects of Convective Heat Transfer, Springer-Verlag, New York, NY.

39. Reynolds, O. (1874), "On the Extent and Action of the Heating Surface for Steam Boilers," Proceedings of the Manchester Literary and Philosophical Society, Vol. 14, p. 7.

40. Von Karman, Th. (1939), "The Analogy Between Fluid Friction and Heat Transfer," Trans. ASME, Vol. 61, pp. 174-210.

41. Colburn, A. P. (1933), "A Method of Correlating Forced Convection Heat Transfer Data and a Comparison with Fluid FLow," Trans. Am. Inst. Chem. Eng., Vol. 29, pp. 174-210.

42. Bejan, A. (1984), Convective Heat Transfer, John Wiley, New York, NY.

43. Arpaci, V. S. and Larsen, P. S. (1984), Convective Heat Transfer, Prentice Hall, Englewood Cliffs, NJ.

44. Kader, B. A. and Yaglom, A. M. (1972), "Heat and Mass Transfer Laws for Fully Turbulent Wall Flows," Int. J. Heat Mass Transfer, 15, pp. 2329-2351.

45. Gatlin, B. (1983), "An Instructional Computer Program for Computing the Steady, Compressible, Turbulent Flow of an Arbitrary Fluid Near a Smooth Wall," M.S. Thesis, Mechanical and Nuclear Engineering Department, Mississippi State University.

46. Love, P., Taylor, R. P., Coleman, H. W. and Hosni, M. H. (1988), "Effects of Thermal Boundary Condition on Heat Transfer in the Turbulent Incompressible Flat Plate Boundary Layer," TFD-88-3, Mechanical and Nuclear Engineering Department, Mississippi State University.

47. Subramanian, C. S. and Antonia, R. A. (1981), "Effect of Reynolds Number on a Slightly Heated Turbulent Boundary Layer," Int. J. Heat Mass Transfer, 24, pp. 1833-1846.

48. Simonich, J. C. and Bradshaw, P. (1978), "Effect of Free-Stream Turbulence on Heat Transfer Through a Turbulent Boundary Layer," J. Heat Transfer, 100, pp. 671-677.

49. Taylor, R. P., Coleman, H. W. and Hodge, B. K. (1984), "A Discrete Element Prediction Approach for Turbulent Flow Over Rough Surfaces," Mechanical and Nuclear Engineering Department, Mississippi State University, Report TFD-84-1.

50. Lin, T. C. and Bywater, R. J. (1982), "Turbulence Models for High Speed, Rough-Wall Boundary Layers," AIAA J., Vol. 20, pp. 325-333.

51. Zukauskas, A. (1972), "Heat Transfer from Tubes in Crossflow," Advances in Heat Transfer, Academic Press, New York, NY.

52. ______________ (1986), Measurement Uncertainty, ANSI/ASME PTC 19.1-1985 Part 1.

53. ______________ (1985), ASHRAE Handbook 1985 Fundamentals, ASHRAE, Atlanta, GA.

54. ______________ (1955), Tables of Thermal Properties of Gases, U. S. National Bureau of Standards Circular 564.

55. Eckert, R. G. and Goldstein, R. J. (1976), Measurements in Heat Transfer, 2nd edition, McGraw-Hill, New York, NY.

56. Kline, S. J., Cantwell, B. J. and Lilley, G. M. (1980), "Report of the Working Group on Hot-wire Anemometry at Low Mach Numbers," The 1980-81 AFOSR-HTTM-Stanford Conference on Complex Turbulent Flows: Comparison of Computation and Experiment, Stanford Univ., Vol. 1, pp. 583-585.

57. Yavuzkurt, S. (1984), "A Guide to Uncertainty Analysis of Hot-Wire Data," Journal of Fluids Engineering, Vol. 106, pp. 181-186.

58. Blackwell, B. F. (1972), "The Turbulent Boundary Layer on a Porous Plate: An Experimental Study of the Heat Transfer Behavior with Adverse Pressure Gradients," Ph.D. Dissertation, Mech. Eng. Dept., Stanford Univ. (Also Report HMT-16).

59. Andersen, P. S. (1972), "The Turbulent Boundary Layer on a Porous Plate: "An Experimental Study of the Fluid Mechanics for Adverse Free-Stream Pressure Gradients," Ph.D. Dissertation, Mech. Eng. Dept., Stanford Univ. (Also Report HMT-15).

60. Preston, J. H. (1954), "The Determination of Turbulent Skin Friction by Means of Pitot Tubes," *J. Roy. Aero. Soc.*, *58*, 109.

61. Patel, V. C. (1965), "Calibration of the Preston Tube and Limitations on its Use in Pressure Gradients," *Journal of Fluid Mechanics*, Vol. 23, Part 1, pp. 185-208.

APPENDIX I

EXPERIMENTAL STANTON NUMBER DETERMINATION AND ITS UNCERTAINTY ANALYSIS

I.1 STANTON NUMBER DATA REDUCTION EQUATION

The Stanton number is the nondimensional convective heat transfer coefficient and may be defined as

$$St = \frac{h}{\rho C_p U_\infty} \tag{I.1}$$

where

h is the convective heat transfer coefficient
ρ is the density of freestream air
C_p is the specific heat of freestream air
U_∞ is the velocity of freestream air

The rate of convective heat transfer (q) from a test plate to the air in the tunnel is defined as

$$q = hA(T_p - T_o) \tag{I.2}$$

where

A is plate area
T_p is plate surface temperature
T_o is freestream air total temperature

Solving equation (I.2) for the convective heat transfer coefficient and substituting into equation (I.1) gives the Stanton number at each plate as

$$St = \frac{q}{\rho C_p U_\infty A(T_p - T_o)} \tag{I.3}$$

In order to determine the convective heat transfer rate q, for each plate, the corresponding radiation and conduction heat losses are required. The modes of heat exchange from each plate are depicted graphically in Figure I.1. Application of an energy balance to a plate gives

$$W = q + q_c + q_r \tag{I.4}$$

where

W is power supplied to the plate

q_r is radiation heat loss rate

q_c is conductive heat loss rate

Solving equation (I.4) for the convective heat transfer rate and substituting into equation (I.3) gives

$$St = \frac{W - q_c - q_r}{\rho C_p U_\infty A(T_p - T_o)} \tag{I.5}$$

The radiation heat loss rate is modeled using

$$q_r = \sigma \epsilon A(T_p{}^4 - T_r{}^4) \tag{I.6}$$

where

σ is the Stefan-Boltzmann constant

ϵ is the emissivity of the plate surface

T_r is the freestream recovery temperature

The conduction heat loss rate is modeled using

$$q_c = (UA)_{eff} (T_p - T_{rail}) \tag{I.7}$$

where

$(UA)_{eff}$ is an experimentally-determined effective conductance between a test plate and the side rails

T_{rail} is the side rail temperature at the axial location of the plate

Substitution of (I.6) and (I.7) into (I.5) gives the final form of the data reduction expression for the Stanton Number

$$St = \frac{W - (UA)_{eff}\ (T_P - T_{rail}) - \sigma\epsilon A(T_p^{\ 4} - T_r^{\ 4})}{\rho C_p U_\infty A(T_p - T_o)} \qquad (I.8)$$

This expression shows explicitly most of the variables involved in the experimental Stanton number determination. Additional variables enter in the determination of the static and total temperature of the freestream air and in the moist air property calculations for C_p and ρ. The freestream air total and static temperatures are calculated using the measured recovery temperature and a recovery factor, R, for the probe:

$$T_o = T_r + (1-R)\ \frac{U_\infty^{\ 2}}{2C_p} \qquad (I.9)$$

$$T_\infty = T_r - (R)\ \frac{U_\infty^{\ 2}}{2C_p} \qquad (I.10)$$

The functional relationship for the moist air specific heat calculation is

$$C_P = C_P(T_\infty,\ T_{wb},\ P_{bar},\ C_{P_{air}},\ C_{P_{H_2O}})$$

where

T_∞ is the freestream air static temperature and is also taken as the dry bulb temperature

T_{wb} is the freestream air wet-bulb temperature

P_{bar} is the barometric pressure

$C_{P_{air}}$ is the dry air specific heat

$C_{p_{H_2O}}$ is the water vapor specific heat

The functional relationship for the moist air density is

$$\rho = \rho(T_\infty, T_{wb}, P_{bar})$$

The Stanton number determination for each plate, therefore, involves the following thirteen variables which are either measured or found from a reference source:

- Plate heater power (W)
- Recovery temperature (T_r)
- Plate temperature (T_p)
- Rail temperature (T_{rail})
- Wet-bulb temperature (T_{wb})
- Effective conductance ($(UA)_{eff}$)
- Plate area (A)
- Barometric pressure (P_{bar})
- Specific heat of dry air ($C_{p_{air}}$)
- Specific heat of water vapor ($C_{p_{H_2O}}$)
- Freestream air velocity (U_∞)
- Recovery factor (R)
- Emissivity (ϵ)

I.2 UNCERTAINTY ANALYSIS OVERVIEW

The detailed uncertainty analysis procedure follows Coleman and Steele 1989 [37], which is consistent with the 1986 ANSI/ASME Standard on Measurement Uncertainty [52]. Briefly, the true value of a quantity, which is approximated by an experimental result r, lies within the interval r ± U_r with 95% confidence. Here U_r is the uncertainty in the result determined from the root-sum-square combination of the bias limit of the result, B_r, and the precision limit of the result, P_r,

$$U_r = (B_r{}^2 + P_r{}^2)^{1/2} \tag{I.11}$$

For a result (such as St) which is a function of J variables and parameters X_i

$$r = r(X_1, X_2, \ldots, X_J) \qquad (I.12)$$

the propagation of the precision limits P_{X_i} of the measured variables into the result is given by

$$P_r = [\sum_{i=1}^{J} (\frac{\partial r}{\partial X_1} P_{X_i})^2]^{1/2} \qquad (I.13)$$

and the propagation of the bias limits B_{X_i} of the variables into the result is given by

$$B_r = \{[\sum_{i=1}^{J} (\frac{\partial r}{\partial X_i} B_{X_i})^2] + 2(\frac{\partial r}{\partial X_1})(\frac{\partial r}{\partial X_2}) B'_{X_1} B'_{X_2} + \ldots\}^{1/2} \qquad (I.14)$$

As explained in [37], there is a term such as the second one on the right hand side of equation (I.14) for each pair of variables that have portions (B'_{X_1} and B'_{X_2}) of their bias limits which are perfectly correlated. These usually arise when the transducers used to measure different variables have been calibrated against the same standard or when two variables (often temperatures or pressures) are measured with the same transducer.

In the current experiments, all of the P_{X_i}'s are negligible compared to the bias limits, so

$$P_{St} = 0 \ . \qquad (I.15)$$

Exceptions to this occur at low freestream velocities--$U_\infty \lesssim 12$ m/sec for the smooth wall tests and $U_\infty \lesssim 6$ m/sec for the rough wall tests--for which the heat transfer coefficients are relatively low. At these conditions the time constant of the THTTF is large enough so that the relatively long period variations in facility line voltage to the test plate heater circuits and in the temperature of the incoming make-up water for the heat exchanger loop affect the ability to hold a tight steady state condition. These annoyances could be overcome with additional expenditures for power conditioning equipment and a water chiller system; however, the observed run-to-run scatter in St results at these low velocities is within acceptable limits. Observations of the St results for eight U_∞ = 12 m/sec replications with the smooth wall and three U_∞ = 6 m/sec replications with the rough wall produced a 95% confidence estimate of P_{St} = 3% for those conditions. This is present because of system unsteadiness and not because of measurement uncertainty.

Application of equation (I.14) to the case of equation (I.8) gives

$$\begin{aligned}
B^2_{St} = {} & \left[\frac{\partial St}{\partial T_p}\right]^2 B^2_{T_p} + \left[\frac{\partial St}{\partial T_r}\right]^2 B^2_{T_r} + \left[\frac{\partial St}{\partial T_{rail}}\right]^2 B^2_{T_{rail}} + \left[\frac{\partial St}{\partial T_{wb}}\right]^2 B^2_{T_{wb}} \\
& + \left[\frac{\partial St}{\partial P_{bar}}\right]^2 B^2_{P_{bar}} + \left[\frac{\partial St}{\partial W}\right]^2 B^2_{W} + \left[\frac{\partial St}{\partial U_\infty}\right]^2 B^2_{U_\infty} + \left[\frac{\partial St}{\partial R}\right]^2 B^2_{R} \\
& + \left[\frac{\partial St}{\partial A}\right]^2 B^2_{A} + \left[\frac{\partial St}{\partial c_{p_{air}}}\right]^2 B^2_{c_{p_{air}}} + \left[\frac{\partial St}{\partial c_{p_{H_2O}}}\right]^2 B^2_{c_{p_{H_2O}}} \\
& + \left[\frac{\partial St}{\partial (UA)_{eff}}\right]^2 B^2_{(UA)_{eff}} + \left[\frac{\partial St}{\partial \epsilon}\right]^2 B^2_{\epsilon} \\
& + 2\left[\frac{\partial St}{\partial T_p}\right]\left[\frac{\partial St}{\partial T_r}\right] B'_{T_p} B'_{T_r} + 2\left[\frac{\partial St}{\partial T_p}\right]\left[\frac{\partial St}{\partial T_{rail}}\right] B'_{T_p} B'_{T_{rail}} \\
& + 2\left[\frac{\partial St}{\partial T_r}\right]\left[\frac{\partial St}{\partial T_{rail}}\right] B'_{T_r} B'_{T_{rail}}
\end{aligned} \tag{I.16}$$

where, as discussed later, the only portions of biases that are considered correlated are those arising from calibrating the thermistors which measure T_p, T_r, and T_{rail} against the same reference standard.

I.3 MEASUREMENTS AND UNCERTAINTIES

The experimental determination of Stanton number requires values for thirteen variables, some of which can be measured directly and some which cannot. Therefore, the methodology used in determination of each variable will be discussed. Discussion of the determination of each variable will include description of the required measurement system, information about the calibration procedures, and uncertainty estimates for each variable.

I.3.1 Plate Heater Power

The power supplied to the heater pad of each plate is measured by a high precision ac watt transducer coupled to a Hewlett Packard (HP) Model 3054 A Automated Data Acquisition and Control System (ADACS), which in turn is connected to a Model 220 microcomputer. This watt transducer is a single phase transducer with a rated output of 1 ma corresponding to 500 watts. The manufacturer specifies ± 0.2% of reading accuracy and 0 to 1 ma dc current output proportional to electrical power.

A separate power circuit is used for each individual plate heater. There are 24 identical power circuits for the 24 test plates. A single watt transducer (Ohio Semitronics Inc. Model EW5-B) is used for all power measurements. The power delivered to a plate heater is measured by routing the power through the watt transducer by switch closures using the ADACS. Since the ADACS cannot process current signals directly, the transducer's output is measured indirectly. A 7.5 KΩ resistor is shunted across the transducer's output lines so that the current output is transformed into a measurable voltage. The shunt resistor is sized to compensate for the small current output from the watt transducer. The current output (ma) from the watt transducer is then obtained using Ohm's law

$$i = [\frac{V}{R}][\frac{1}{1000}] \qquad (I.17)$$

This current output is then translated into power (watts) using the relationship

$$W = 500 \times i \qquad (I.18)$$

A calibration plate heater circuit was used to check the calibration of the watt transducer by comparison of the transducer measurement to the heater power (W_{act}) determined using the ADACS. This power was obtained by measuring the ac voltage drop across the plate heater, the resistance of the plate heater, and using

$$W_{act} = \frac{V^2}{R} \qquad (I.19)$$

Due to the importance of resistance and voltage measurement in determination of both transducer and actual powers, extreme care was exercised to utilize the ADACS properly. In particular, the resistances from the plate heater and shunt resistor were measured using the four-wire technique. In this method, the resistance of the transmission line is measured and is subtracted from the measured total resistance automatically. Therefore, the resistance obtained by the four-wire technique represents the load resistance alone.

Uncertainties: The high resolution digital voltmeter (3456A) used for both voltage and resistance measurements has a voltage accuracy of ± 0.007% of reading with an ADACS environment temperature of 23 C and an additional 0.0002% error for every 1 C in the environment temperature above or below 23 C. Resistance accuracy for the ADACS is 0.008% of reading, and the environment temperature coefficient is 0.004%/C for four-wire ohm. It was assumed that the manufacturer's specification on the accuracies of the resistance and voltage measurements are the bias limits with 95% confidence level so that averaging multiple readings would not reduce these estimates. Therefore, the bias limits on the voltage and resistance measurements become

$$\frac{B_V}{V} = \pm 7 \times 10^{-5}$$

$$\frac{B_R}{R} = \pm 8 \times 10^{-5}$$

The bias limit in the determination of the watt transducer output current using equations (I.14) and (I.17) is

$$[\frac{B_i}{i}]^2 = [\frac{B_R}{R}]^2 + [\frac{B_V}{V}]^2$$

$$[\frac{B_i}{i}] = \pm 0.01\%$$

and the bias limit in the determination of the actual power measurement using equations (I.14) and (I.19) is

$$[\frac{B_{W_{act}}}{W_{act}}]^2 = [\frac{B_R}{R}]^2 + [2\,\frac{B_V}{V}]^2$$

$$[\frac{B_{W_{act}}}{W_{act}}] = \pm 0.02\%$$

These are so small as to be negligible for our purposes. Precision errors were also observed to be negligible.

Although the output from the watt transducer can be measured with high accuracy as indicated above, how well this is translated into power using equation (I.18) must be determined by comparing the power indicated by the watt transducer to the actual power as found from the calibration tests. (The inductance in the heating element was accounted for, with the power factor being greater than 0.999 [23].) The power indicated by equation (I.18) from the output of the watt transducer was compared with the actual power as measured by the ADACS (I.19) using 172 points over the 0-250 watt range of interest. Figure I.2 shows the cumulative probability curve of the absolute values of the percent differences. As shown, a 95% confidence estimate of the uncertainty in the watt transducer power measurement based on these points is ± 0.9% of reading. This appears as a bias error in W when equation (I.18) is used.

I.3.2 Temperatures

Temperatures are measured using thermistors, which are temperature sensitive resistors with a negative temperature coefficient. These thermistors have a nominal resistance of 50,000 ohms at 25 C and are highly sensitive to small temperature changes (about 1-2 KΩ/C). They are guaranteed, by the manufacturer, to have ± 0.2 C interchangeability over a range of temperatures from 0 C to 70 C. The resistances of the thermistors are measured by the ADACS. These thermistors are used to determine the freestream air temperature, the test plate temperatures, and the metal support rail temperatures.

The calibration of the thermistors was done in a Blue M Model MR-3210A-1 constant temperature bath. The bath temperature was monitored by a Hewlett Packard Model 2804A quartz thermometer instrumented with a Model 18111A quartz probe. The absolute accuracy of this thermometer/probe combination is specified by the manufacturer as ± 0.040 C over a range of -50 C to 150 C. The thermistors were placed individually inside glass test tubes to protect them and avoid their contamination. To ensure effective conduction of heat from the water bath to each thermistor, each test tube was filled with Megatherm 201 (by Omega Engineering, Inc.), which is a high thermal conductivity, filled silicone paste. The spatial variation in the temperature of the bath was found to be about ± 0.4 C. This variation was minimized to ± 0.02 C by centering the test tubes containing thermistors around the quartz probe in groups of fourteen. Since the reliability of measured thermistor resistances depends on the accuracy of measurements made by the ADACS, the proper use of the ADACS during the measurement process was carefully examined.

The thermistor calibrations were performed for the range of temperatures 22 C - 50 C using six evenly spaced points over this range. The thermistors are extremely nonlinear but their behavior can be very closely approximated by the Steinhart-Hart equation as

$$T[K] = 1/[A + B \ln R + C(\ln R)^3] \tag{I.20}$$

where R is resistance in ohms. The curvefit constants A, B and C were calculated using the thermistor manufacturer's data as $A = 9.6401 \times 10^{-4}$, $B = 2.1095 \times 10^{-4}$ and $C = 8.48 \times 10^{-8}$.

Uncertainties: The temperatures obtained using the measured thermistor resistances in the Steinhart-Hart relation (equation (I.20)) were compared with the temperatures from the quartz thermometer. The difference between the temperatures measured by the quartz thermometer and the temperatures calculated from the measured thermistor resistances using the curvefit equation was determined for a total of 360 calibration points. Figure I.3 shows the cumulative probability curve of the absolute values of the differences. As shown, 95% are less than about 0.09 C. This is taken as a bias limit since precision errors were observed to be negligible.

The bias limits for the elemental error sources which affect the various thermistors are estimated as

Elemental error source	Bias limit
Calibration: Quartz probe	± 0.04 C
Calibration: Bath nonuniformity & curvefit	± 0.09 C
Installation in test plates	± 0.1 C
Nonuniformity in side rail temperatures	± 0.4 C

The installation error for the test plate thermistors was estimated based on the temperature variations predicted within a test plate during the design calculations by Norton [22]. Since the temperature indicated by the plate thermistors is used as the plate surface temperature, T_p, in equation (I.8), such variations are the source of a bias error. The overall bias limit for each plate temperature measurement is found from the root-sum-square of the three appropriate elemental error sources as

$$B_{T_p} = [(0.04)^2 + (0.09)^2 + (0.1)^2]^{1/2} = 0.14 \text{ C}$$

For measurements of the side rail temperature, T_{rail}, at a given axial location, the overall bias limit is found from the root-sum-square of the three appropriate elemental error sources as

$$B_{T_{rail}} = [(0.04)^2 + (0.09)^2 + (0.4)^2]^{1/2} = 0.4 \text{ C}$$

For measurements of the freestream air recovery temperature, T_r, no installation bias appears and so

$$B_{T_r} = [(0.04)^2 + (0.09)^2]^{1/2} = 0.1 \text{ C}$$

Since the same calibration standard (quartz probe) was used for all thermistors, the standard's bias limit is a correlated bias error source that has to be accounted for in the data reduction uncertainty analysis. Thus, $B'_{T_p} = B'_{T_r} = B'_{T_{rail}} = 0.04$ C in equation (I.16).

I.3.3 Effective Conductance

The effective conductance $(UA)_{eff}$ was determined from

$$(UA)_{eff} = \frac{q_c}{(T_p - T_{rail})} \qquad (I.21)$$

where

$(UA)_{eff}$ is the effective conductance between a test plate and the support rails

q_c is the input power to a plate heater under conductance calibration conditions

In order to estimate the effective conductance, an experimental approach was taken. Insulation was placed over the top of the test plates, which then were heated by power input to the plate heaters. Since there were no radiative or convective heat losses from the covered plates, the total input power to the heater plates was equal to the conductive heat transfer loss from the plates, which was modeled with equation (I.21).

The support rails were heated by two 150 watt tape heaters installed on each side rail. When the plate temperatures and the rail temperatures reached a prespecified temperature, the powers to the plate heaters were reduced to 0.6 watts and the rail heaters were turned off. The test plate temperatures and the rail temperatures at $x = 1.2$ m were monitored until the temperature differences between each test plate and the rail temperature approached a steady state condition.

For each plate, from each temperature difference and the corresponding input power, an effective conductance was determined. A single value of effective conductance (0.42 watt/C) was determined for use with all test plates. This value was obtained by averaging the effective conductances of test plates 6 through 18. The precision index S of this sample of effective conductances was 0.08 watt/C .

Uncertainties: The uncertainties were determined by using the uncertainty analysis equations (I.11) - (I.14) and equation (I.21) which models the conductive heat loss. Since

$$(UA)_{eff} = \frac{q_c}{T_p - T_{rail}}$$

then

$$\left[\frac{B_{(UA)_{eff}}}{(UA)_{eff}}\right]^2 = \left[\frac{B_{q_c}}{q_c}\right]^2 + \left[\frac{-B_{T_p}}{(T_p - T_{rail})}\right]^2 + \left[\frac{B_{T_{rail}}}{(T_p - T_{rail})}\right]^2$$

$$+ 2\,B'_{T_p} B'_{T_{rail}} \left[\frac{-1}{T_p - T_{rail}}\right]\left[\frac{1}{T_p - T_{rail}}\right]$$

From previous discussion we have

$$B_{T_p} = 0.14\ C$$

$$B'_{T_p} = B'_{T_{rail}} = 0.04\ C$$

and

$$\frac{B_{q_c}}{q_c} = 0.009$$

The bias limit for T_{rail} does not include the 0.4 C nonuniformity contribution since only the middle 13 plates were used in the calibration test to avoid the larger variations in T_{rail} at the beginning and end of the test section. For this case, then,

$$B_{T_{rail}} = 0.1\ C$$

Using a nominal value for $(T_p - T_{rail})$ of 1.3 C from the calibration test, the bias limit in the effective conductance becomes

$$\left[\frac{B_{(UA)eff}}{(UA)_{eff}}\right]^2 = (0.009)^2 + \left[\frac{0.14}{1.3}\right]^2 + \left[\frac{0.1}{1.3}\right]^2 - 2(0.04)(0.04)\left[\frac{1}{1.3}\right]\left[\frac{1}{1.3}\right]$$

$$\left[\frac{B_{(UA)eff}}{(UA)_{eff}}\right] = 0.13$$

Using the precision limit ($P = tS = 0.174$ watt/C) at a 95% confidence level calculated from the t-distribution ($n=13$, $t=2.179$) and the precision index S, the overall uncertainty for the effective conductance becomes

$$\left[\frac{U_{(UA)eff}}{(UA)_{eff}}\right]^2 = \left[\frac{B_{(UA)eff}}{(UA)_{eff}}\right]^2 + \left[\frac{P_{(UA)eff}}{(UA)_{eff}}\right]^2$$

$$\left[\frac{U_{(UA)eff}}{(UA)_{eff}}\right]^2 = (0.13)^2 + \left[\frac{0.174}{0.42}\right]^2 = (0.13)^2 + (0.42)^2$$

$$\left[\frac{U_{(UA)eff}}{(UA)_{eff}}\right] = 45\%$$

Since the constant value of 0.42 watt/C is always used for $(UA)_{eff}$, this uncertainty is fossilized [37] into a bias limit when $(UA)_{eff}$ is used in the calculation of Stanton numbers. Therefore,

$$B_{(UA)eff} = 45\%.$$

I.3.4 Area

The surface area of the plates is determined from the lengths of the sides (10.16 cm by 45.72 cm)

$$A = (S_1)(S_2)$$

The plates were manufactured with length and width tolerances of ± 0.0025 cm.

Uncertainties: The uncertainty in the plate area is assumed to be all bias and may be expressed as

$$\left[\frac{B_A}{A}\right]^2 = \left[\frac{B_{S_1}}{S_1}\right]^2 + \left[\frac{B_{S_2}}{S_2}\right]^2$$

Substitution of the plate dimensions and bias limits gives

$$\left[\frac{B_A}{A}\right]^2 = \left[\frac{0.0025}{10.16}\right]^2 + \left[\frac{0.0025}{45.72}\right]^2$$

$$\left[\frac{B_A}{A}\right] = 0.03\%$$

The possibility of thermal expansion of the test plates (which could introduce additional uncertainty into the area) was considered. It was found that this effect was negligible compared to the bias due to manufacturing tolerance.

I.3.5 Air Density and Specific Heat

The fluid in the test section is actually a mixture of dry air and water vapor. Therefore, fluid properties such as density and specific heat for the test air will depend on the ratio of dry air and water vapor in the mixture. The ratio of dry air and water vapor in air is reflected by the partial pressures of each. The density and specific heat of the mixture may be expressed in terms of the partial pressures of the dry air and water vapor. Once the partial pressures of the dry air and water vapor are known, they may be substituted into expressions for the density and specific heat of the mixture.

Psychrometrics: The partial pressure of the water vapor at saturation, evaluated at the dry bulb temperature T_∞, is given by

$$P_{ws} = \exp[C8/T_\infty + C9 + (C10)T_\infty + (C11)T_\infty^2 + (C12)T_\infty^3 + (C13)\ \ell n(T_\infty)]$$

and the partial pressure of the water vapor at saturation, evaluated at the wet bulb temperature, is given by

$$P_{wswb} = \exp[C8/T_{wb} + C9 + (C10)T_{wb} + (C11)T_{wb}^2 + (C12)T_{wb}^3 + (C13)\ \ell n(T_{wb})]$$

where the constants are

$C8 = -10440.4$
$C9 = -11.2946669$
$C10 = -0.02700133$
$C11 = 1.289706 \times 10^{-5}$
$C12 = -2.478068 \times 10^{-9}$
$C13 = 6.5459673$

the temperatures are in degrees R, and the partial pressures in psia [53]. P_{wswb} can be used to determine the humidity ratio at wet bulb temperature from

$$W_{wb} = \frac{(0.62198)\ P_{wswb}}{(P_{bar} - P_{wswb})}$$

The humidity ratio is then obtained as

$$W = \frac{[1093 - (0.556)T_{wb}](W_{wb}) - 0.24(T_\infty - T_{wb})}{1093 + (0.44)T_\infty - T_{wb}}$$

and the humidity ratio at saturation as

$$W_s = \frac{(0.62198)\ P_{ws}}{P_{bar} - P_{ws}}$$

The degree of saturation is defined as

$$U_s = \frac{W}{W_s}$$

and the relative humidity is then calculated using

$$\phi = \frac{U_s}{1 - (1 - U_s)(P_{ws}/P_{bar})}$$

The partial pressure of the water vapor is determined from the relative humidity and the partial pressure of the water vapor at saturation, thus

$$P_w = P_{ws}\ \phi$$

Once the partial pressure of the water vapor and the ambient pressure are known, Dalton's law of partial pressure may be applied to determine the partial pressure of the dry air as

$$P_a = P_{bar} - P_w$$

Density: The density of the moist air flowing through the test section may be expressed as

$$\rho = \frac{m_a + m_w}{V_m} = \frac{m_a}{V_m} + \frac{m_w}{V_m}$$

The ideal gas law may be applied to the dry air and water vapor and written as

$$P_a V_m = n_a \bar{R} T_\infty$$
$$P_w V_m = n_w \bar{R} T_\infty$$

The number of moles of a gas is equal to the quotient of the mass of gas divided by the molecular weight of the gas. Therefore, the number of moles of dry air and water vapor may be expressed as

$$n_a = m_a/M_a$$
$$n_w = m_w/M_w$$

The specific gas constants of dry air and water vapor are defined as

$$R_a = \bar{R}/M_a$$
$$R_w = \bar{R}/M_w$$

Substitution into the ideal gas law relations gives

$$P_aV_m = m_aR_aT_\infty$$
$$P_wV_m = m_wR_wT_\infty$$

Solving for the dry air mass and the water vapor mass and substituting in the density equation yields

$$\rho = \frac{P_a}{R_aT_\infty} + \frac{P_w}{R_wT_\infty} \qquad (I.22)$$

This equation states that the density of a mixture of gases is the sum of the densities of the component gases at their respective partial pressures.

Specific Heat: The specific heat of the test air may be determined by applying an energy balance to the dry air and water vapor system.

$$C_pm_mT_\infty = C_{p_a}m_aT_\infty + C_{p_w}m_wT_\infty$$

Solving for the specific heat of the mixture and substituting for the mass of mixture yields

$$C_p = \frac{C_{p_a} m_a + C_{p_w} m_w}{m_a + m_w}$$

Substituting for the mass of the dry air and the mass of water vapor and dividing by the total number of moles in the mixture gives

$$C_p = \frac{C_{p_a} M_a n_a/n}{M_a(n_a/n) + M_w(n_w/n)} + \frac{C_{p_w} M_w n_w/n}{M_a(n_a/n) + M_w(n_w/n)}$$

From the thermodynamic principles of the mixture of gases, we know that the ratio of each partial pressure to the total pressure is equal to the mole fraction of each component. Therefore, we have

$$\frac{P_a}{P} = \frac{n_a}{n}$$

$$\frac{P_w}{P} = \frac{n_w}{n}$$

Substitution for the number of moles in terms of partial pressures gives the final expression for the specific heat of the test air as

$$C_p = \frac{C_{p_a} M_a P_a + C_{p_w} M_w P_w}{M_a P_a + M_w P_w} \qquad (I.23)$$

It should be noted that the following assumptions have been made in this section. The curvefit equations used to obtain partial pressures are assumed very accurate, and their uncertainties are negligible in comparison with the measurement uncertainties.

The ideal gas thermodynamic relationships used to calculate the test air properties are applicable to the dry air and saturated water vapor, and the uncertainties introduced by their application to a non-ideal gas are negligible as compared with the measurement uncertainties and the uncertainties in the properties obtained from reference tables.

Uncertainties: A sling psychrometer is inserted through an access hole in the top of the test section and is used to find the wet bulb temperature of the test air. The bias limit in T_{wb} is taken as 1.0 C and precision error is assumed negligible. The static air temperature determined from the recovery temperature measured by the thermistor probe is used for the dry bulb temperature. A temperature compensated barometer with a resolution of 0.5 mm Hg is used to determine the ambient pressure. Since the pressure of the test air mixture (dry air + water vapor) in the test section is kept equal to the outside ambient pressure, using make-up air controls, the pressure read from the barometer is used as the air mixture pressure. A bias limit of 1.0 mm Hg and negligible precision error are assumed for P_{bar}.

The specific heats for dry air and for water vapor were obtained as [54] $C_{p_{air}} = 1.006$ kJ/kg C and $C_{p_{H_2O}} = 1.86$ kJ/kg C with an uncertainty in each estimated as 0.5%. These uncertainty estimates are fossilized into bias limits when the specific heat values are used in calculations.

I.3.6 Air Velocity

A Pitot probe is used to determine the freestream velocity. The Pitot probe channels the stagnation pressure and static pressure exerted by the freestream into a differential pressure transducer so that the freestream dynamic pressure can be measured. Once the dynamic pressure (ΔP) is known, the freestream velocity may be determined from

$$U_\infty = \left(\frac{2\Delta P}{\rho}\right)^{1/2} \qquad \text{(I.24)}$$

where ρ is the density of the freestream air. The procedure for determination of the test air density has already been described. The dynamic pressure determination methodology is presented next.

Dynamic pressure measurement is performed using two differential pressure transducers with ranges of 0.55 and 3.45 KPa. These transducers cover the full range of dynamic pressures expected. Their accuracy, specified by the manufacturer, is ± 0.5 percent of full scale. Each transducer provides a voltage output of 0-5 Vdc proportional to the applied pressure difference. The voltage outputs of the pressure transducers are measured by the ADACS.

The calibration of each pressure transducer was accomplished by employing a very sensitive water micromanometer as the pressure source. The 25.4 cm range micromanometer is equipped with a magnifier which amplifies the fluid meniscus at the reference hairline and provides direct reading indication to 0.0025 cm of water.

Each pressure transducer was calibrated individually. Various pressures within the pressure transducer range were generated using the micromanometer and were applied to the transducer. The values of these generated pressures indicated by the micromanometer were recorded and the corresponding voltage outputs from the pressure transducer were measured using the ADACS in a manner corresponding to actual testing. The number of pressure calibration points obtained for the 0.55 and 3.45 KPa range transducers were 23 and 10, respectively. Both pressure transducers demonstrated small but stable voltage outputs at zero pressures (zero shift). The pressure calibration data collected from each transducer was corrected for the zero shift.

Subsequently, the data of each transducer was used to arrive at an appropriate curvefit equation for that transducer. A linear curvefit equation for the 3.45 KPa range pressure transducer was satisfactory, but a quadratic equation was necessary to fit the 0.55 KPa range pressure transducer calibration data satisfactorily.

Uncertainties: A comparison between the direct pressure measurement data (micromanometer readings) and the pressures calculated from the curvefit equation was made for each pressure transducer. The results indicated that the bias limits associated with using the calibration curvefits for the 0.55 and 3.45 KPa range transducers were 0.5 percent and 0.1 percent of reading, respectively. Precision errors were observed to be negligible during the calibration process, and the bias error inherent in the micromanometer (which was used as the calibration standard) was assumed negligible.

During the actual dynamic pressure measurement when a Pitot probe in the flow stream is the pressure source for the transducer, the elemental bias error sources are the Pitot probe and the measurement system calibration. Therefore, the calibration bias and the additional biases introduced by the Pitot probe must be combined using RSS to arrive at the overall bias limit for actual dynamic pressure measurements. Biases in the dynamic pressure due to errors caused by Pitot probe design, use, and misalignment have been estimated at 0.5 percent since the freestream flow is uniform and relatively free of perturbations and since the Pitot probe is very carefully aligned with the flow. The bias limit estimates are

for Pitot probe	0.5% of reading
for 0.55 KPa transducer (calibration)	0.5% of reading
for 3.45 KPa transducer (calibration)	0.1% of reading.

Therefore, bias limits for dynamic pressure measurements become

$$(\frac{B_{\Delta P}}{\Delta P}) = [(0.005)^2 + (0.005)^2]^{1/2} = 0.7\%$$

for the 0.55 KPa transducer, and

$$(\frac{B_{\Delta P}}{\Delta P}) = [(0.001)^2 + (0.005)^2]^{1/2} = 0.5\%$$

for the 3.45 KPa transducer.

The bias limit in the free stream velocity is dependent on the bias limit in the dynamic pressure and on the bias limit in the density. As discussed above, bias limits for the dynamic pressures measured using the 0.55 KPa and 3.45 KPa transducers are 0.5% and 0.7% of reading, respectively. For the bias limit of the air density, based on an analytical uncertainty analysis using nominal values of the related variables, an estimated value of 0.3% is used. This is a conservative value and does not change significantly with small changes in the environment and/or operating conditions of the tunnel.

Applying equation (I.14) to equation (I.24), the expression for the bias limit of the freestream velocity is

$$(B_{U_\infty})^2 = [\frac{\partial U_\infty}{\partial \Delta P} B_{\Delta P}]^2 + [\frac{\partial U_\infty}{\partial \rho} B_\rho]^2$$

which, after substitution of the appropriate partial derivatives and division by the velocity gives

$$[\frac{B_{U_\infty}}{U_\infty}]^2 = [\frac{1}{2}]^2 [\frac{B_{\Delta P}}{\Delta P}]^2 + [\frac{1}{2}]^2 [\frac{B_\rho}{\rho}]^2$$

The bias limit when the 0.55 KPa pressure transducer is used is

$$\left[\frac{B_{U_\infty}}{U_\infty}\right] = \left[\frac{1}{2}\right]^2 (0.007)^2 \left[\frac{1}{2}\right]^2 (0.003)^2$$

$$\left[\frac{B_{U_\infty}}{U_\infty}\right] = 0.4\%$$

The bias limit when the 3.45 KPa pressure transducer is used is

$$\left[\frac{B_{U_\infty}}{U_\infty}\right]^2 = 0.3\%$$

Precision errors have been observed to be negligible in the determination of U_∞, so the precision limit for U_∞ is assumed zero.

I.3.7 Air Temperature Probe Recovery Factor

The temperature obtained from the air thermistor is the recovery temperature T_r. The freestream total temperature and static temperature are computed from T_r using equations (I.9) and (I.10), but a value for recovery factor R is necessary for the calculation. Based on the review of available data [55], a value of R = 0.86 was chosen with an uncertainty of 0.09. This uncertainty is fossilized into a bias limit when the recovery factor is used in calculations.

I.3.8 Test Plate Emissivity

Radiation from the heated test plates primarily falls within the infrared range from 2 to 100 microns. Plexiglass has a high absorbtivity at these wavelengths and transmits only 2% of the incident infrared radiation. Since the test plates are enclosed by the plexiglass side and top walls, a gray body enclosure radiation model is used. Because plexiglass has a high emissivity of about 0.9 and because of the magnitude of the areas involved, the general gray body enclosure model simplifies to the special case of a small object in a large cavity.

As discussed previously with equation (I.6), the radiative heat losses from the test plates are modeled using

$$q_r = \sigma \epsilon A({T^4}_p - {T^4}_r)$$

The emissivity ϵ of the test plates is very dependent on the state of oxidation and cleanliness of the plates. Typical values of the emissivity as quoted in various handbooks are ~0.05 for a polished electroplated nickel surface at 23 C, ~0.11 for an unpolished electroplated nickel surface at 20 C, and ~0.37 for heavily oxidized nickel at 200 C. An emissivity typical of unpolished electroplated nickel (0.11) was assumed with a bias limit of ± 0.05.

I.4 UNCERTAINTY ANALYSIS RESULTS

A jitter program [37] was used to determine an uncertainty estimate for each experimentally determined Stanton number. In the jitter program, the data reduction computer program was treated as a subroutine and used to approximate the partial derivatives in equation (I.16) using finite differences. In this numerical uncertainty analysis scheme, the first step was to read the original experimental data from a data file and calculate the Stanton number for each of the 24 plates using the data reduction subroutine. Then the partial derivatives of the Stanton number with respect to each of the thirteen variables were determined numerically using finite difference approximations. The evaluation of a partial derivative was accomplished using a loop through which the original value of one variable was perturbed by a prespecified amount and calculating new Stanton numbers for all 24 plates using the data reduction subroutine. The difference between each new Stanton number and the original unperturbed Stanton number divided by the amount that the particular variable was perturbed resulted in a value for a partial derivative. Before calculation of the next partial derivative the perturbed value of the previous variable was reset to the original value and then the next variable was perturbed.

Upon completion of all partial derivatives, equation (I.16) was evaluated. Since precision limits in the measurements were assumed negligible, only the bias limits for the thirteen variables were required, and the bias limits used were

Variable	Bias limit	Nominal Values
Plate Temperature	0.14 C	45 C
Rail Temperature	0.4 C	45 C
Recovery Temperature	0.10 C	30 C
Wet-Bulb Temperature	1.0 C	27 C
Barometric Pressure	1.0 mm Hg	760 mm Hg
Recovery Factor	0.09	0.86
Power	0.9%	20-150 W
Area	0.03%	464.5 cm^2
Air Velocity	0.4%	6-70 m/s
$c_{p_{air}}$	0.5%	1.006 kJ/kg C
$c_{p_{H_2O}}$	0.5%	1.86 kJ/kg C
$(UA)_{eff}$	45%	0.42 W/C
Emissivity	45%	0.11

In addition, some of the bias errors in temperatures were correlated since the same calibration standard was used. The correlated biases are

$$B'_{T_p} = B'_{T_r} = B'_{T_{rail}} = 0.04\ C$$

For the Stanton number data discussed in this report, the overall uncertainty (as computed using equation (I.11)) ranged from about 2 percent to 5 percent, depending on flow conditions. Uncertainty bars are indicated on representative data points when the St data are plotted.

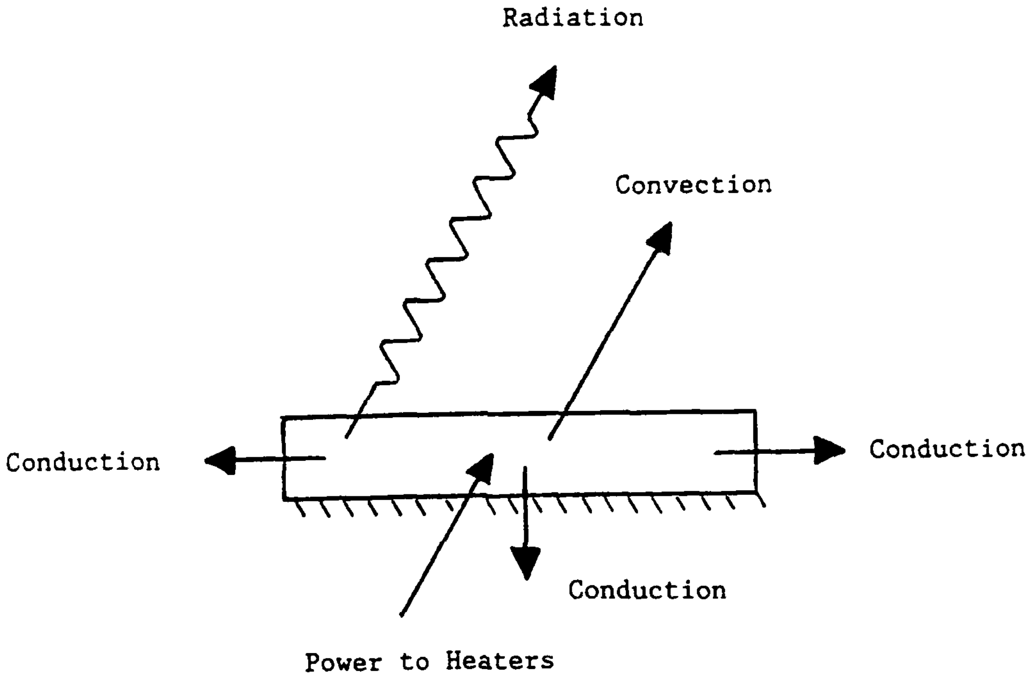
Radiation
Convection
Conduction
Conduction
Conduction
Power to Heaters

Figure I.1 Energy Balance on a Test Plate.

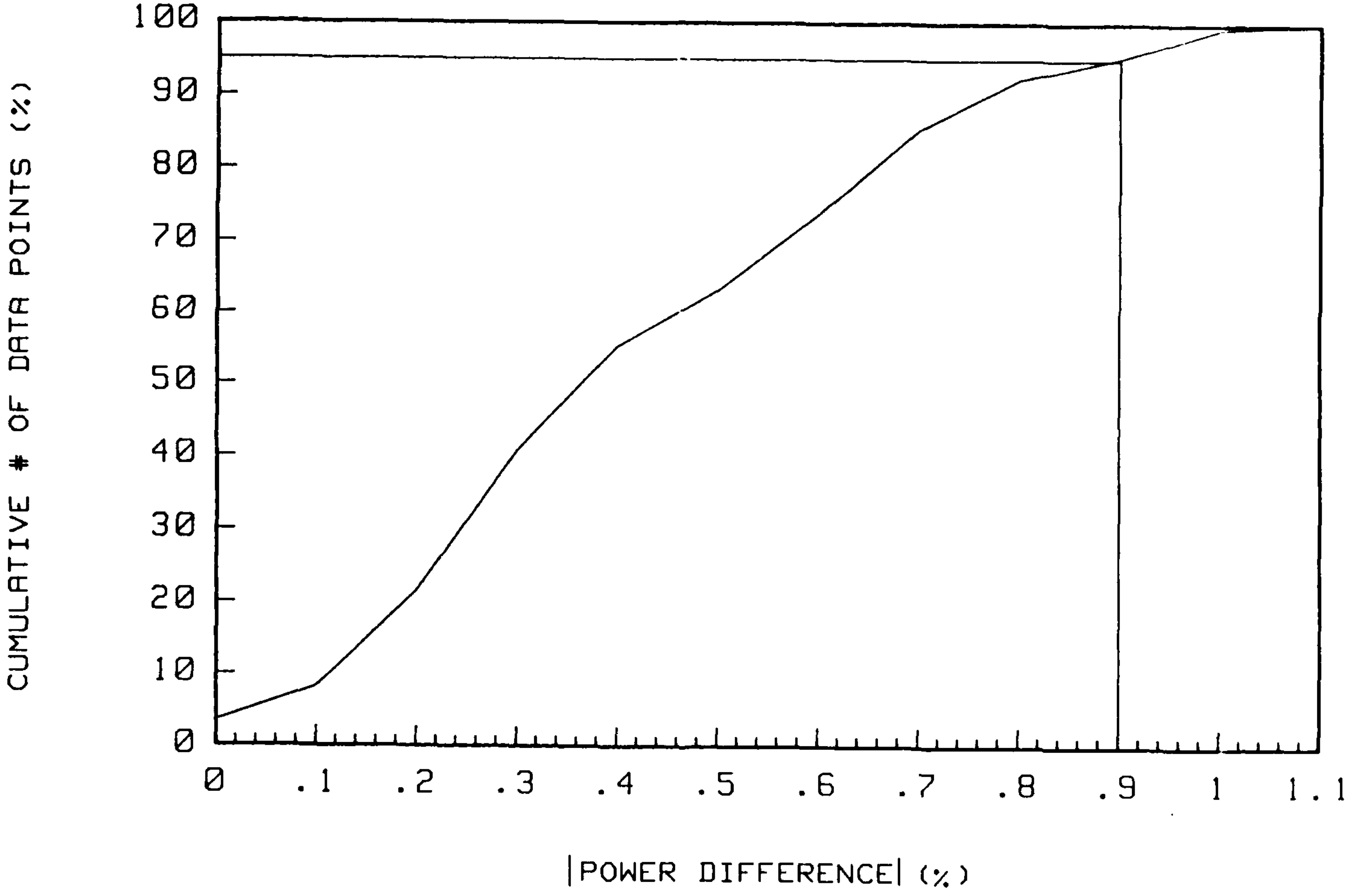

Figure I.2 Power Measurement Calibration Results.

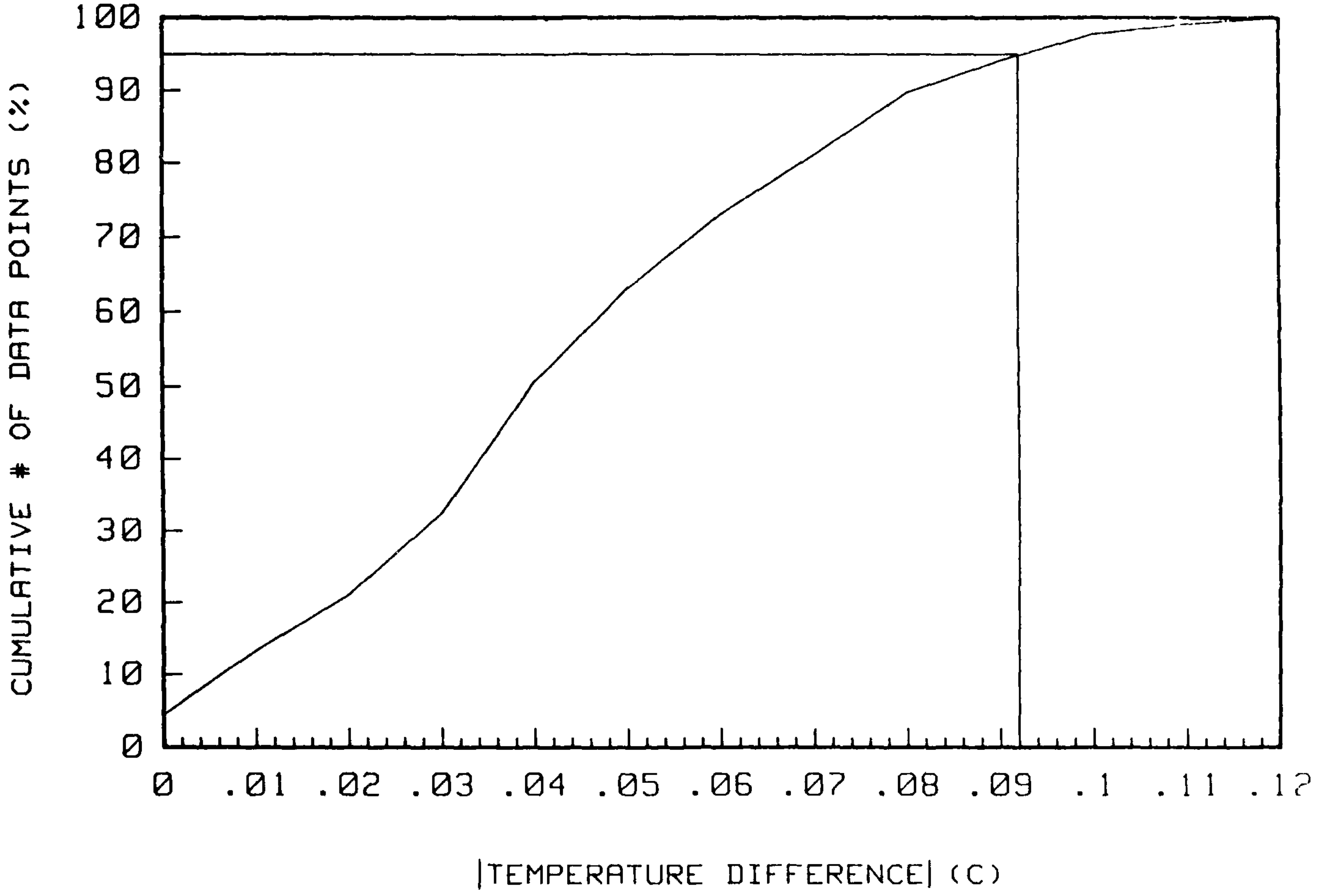

Figure I.3 Thermistor Calibration Results.

APPENDIX II

BOUNDARY LAYER PROBE MEASUREMENTS

II.1 HOT-WIRE ANEMOMETRY

Profiles of boundary layer mean velocity and turbulence components were measured with hot-wire anemometry. The hot-wire instrumentation consisted of a TSI-IFA 100 Intelligent Flow Analyzer System with two constant temperature anemometer units and an HP-3437A high speed system voltmeter in the HP-3054A Automatic Data Acquisition and Control System (ADACS) which was linked to an HP-Series 9000 Model 220 microcomputer. Two hot-wire probes were used: a DANTEC 55P05 horizontal, boundary-layer type probe and a DANTEC 55P02 45° slant probe, both of 5 micron diameter platinum plated tungsten wire with gold plated ends. Each of the two anemometer units in the flow analyzer was dedicated to either the horizontal or slanted probe. Digital readings of the anemometer voltages were made with the HP-3437A high speed voltmeter connected directly to the signal conditioned anemometer output. These digital voltage readings were then relayed to the microcomputer.

The horizontal hot-wire probe and the slanted hot-wire probe are shown schematically with their supports in Figures II.1 and II.2, respectively. These probes are identical to those used by Pimenta 1975 [13] and Coleman 1976 [14]. Each probe was mounted in a custom made holder with a vertical micrometer head traversing mechanism having a resolution of 0.025 mm. Both probe holders were supported by an xz traverse attached to a special sled that spanned the tunnel and rested on the side walls. Locating pins held the xz traverse in place on the special sled. Four hold down screws fixed the sled to the side walls of the test section.

In use, both probes had to be lowered to the plate surface for a reference height above the plate to be established. To prevent the horizontal wire from hitting the wall, a keel or wall stop was epoxied to the probe stem of the horizontal wire. A collar on the spindle of the slant wire probe provided a wall stop for the slant wire. The probes were lowered until electrical continuity through the wall stop between the probe stem and the plate surface was established. Conductive ink was placed on the back of the horizontal wire keel to provide electrical continuity between the keel and probe stem. With the hot-wire/plate clearance provided by the wall stops known, any desired vertical probe height above the plate could be set to within 0.025 mm. When used with the rough surface, a cylindrical rod slightly longer than the roughness height was attached to the wall stops so that the smooth portion of the rough wall could be used as a reference position.

II.1.1 Horizontal Hot-Wire Probe Measurements

Measurements of the mean velocity and the fluctuating longitudinal velocity component $(\overline{u'^2})$ were made with the horizontal hot-wire. The horizontal wire was aligned with the flow by matching etched marks on the holder and horizontal traversing mechanism. Once the probe was aligned with the flow and freestream measurements had been taken, the boundary layer velocity profile measurements began with the probe keel starting just above the wall for the first measurement. Measurements were typically taken at every 1-2% of the normalized velocity (u/U_∞) in the inner region of the boundary layer and every 2-4% of the normalized velocity in the outer region. At each measurement position, 1000 instantaneous anemometer output voltage readings were taken 0.01 seconds apart and used to compute 1000 corresponding velocities. A fourth order least squares calibration equation was used to convert anemometer voltages into velocities. The mean of the 1000 computed velocities was used as the mean velocity at that location. The longitudinal velocity fluctuation $(\overline{u'^2})$ was taken as the square of the standard deviation (the variance) of the 1000 computed velocities. Experience showed that stable averages were obtained using this number of readings over the 10 second time period.

II.1.2 Slant Hot-Wire Probe Measurements

The slant wire was used to determine the Reynolds shear stress factor ($\overline{u'v'}$), the normal velocity fluctuation ($\overline{v'^2}$), and the transverse velocity fluctuation ($\overline{w'^2}$). The slant wire was mounted on the rotatable spindle of the probe holder with its prongs parallel to the mean flow direction at any angle of rotation. The spindle was rotated by a cable drive, which could be operated with the probe in the tunnel. A "lock-drum" system with eight radially drilled holes spaced 45° apart and a spring loaded pin with a lever located at the top of the vertical traverse mechanism were used to lock the spindle into the desired orientation by fitting the pin into one of the drilled holes.

Alignment of the slant wire spindle with the mean flow was done in the freestream. A schematic of the slant wire geometry and coordinates is given in Figure II.3. The slant wire was placed in the horizontal plane (θ=90°,270°) and the output of the anemometer was noted for these two probe orientations. Alignment of the probe spindle and slant wire with the mean flow was adjusted by rotating the probe stem around its y-axis. The alignment of the probe was adjusted back and forth in small increments across the flow direction in a iterative manner until the difference between the electrical signals at probe rotation angles of θ=90° and θ=270° was 3-5mV from a 3-5V signal. The corresponding error in the indicated mean velocity due to misalignment of the slant wire probe was less than 0.12 m/s for freestream velocities as high as 46 m/s.

To determine $\overline{v'^2}$, $\overline{w'^2}$, and $\overline{u'v'}$, the slant wire was positioned approximately 3.3 mm above the surface of the smooth plate (or about 4 mm above the smooth surface of the rough plate) and measurements were made at three probe rotation angles θ=45°, 90°, and 135°. At each probe rotation angle, 4000 instantaneous anemometer output voltage readings 0.025 seconds apart were taken and used to compute 4000 corresponding effective velocities (u_{eff}). A fourth order least squares calibration correlation was used to convert anemometer voltages into effective velocities. The fluctuating component of the effective velocity ($\overline{u'^2_{eff}}$) at each rotation angle was taken as the square of the standard deviation (the variance) of the 4000 computed effective velocities. Experience showed that this many readings taken over the 100 second time period provided stable averages.

The values of $\overline{u'^2_{eff}}$ at the three slant wire probe orientations were used in conjunction with the value of $\overline{u'^2}$ from the horizontal wire measurements at the same y-position to solve a system of three linear equations for $\overline{v'^2}$, $\overline{w'^2}$, and $\overline{u'v'}$. These linear equations were generated with equation (II.1) evaluated at the three probe rotation angles as discussed in detail by Coleman 1976 [14].

$$\overline{u'^2_{eff}} = A\,\overline{u'^2} + \frac{D^2}{4A}\,\overline{v'^2} + \frac{F^2}{4A}\,\overline{w'^2} + D\,\overline{u'v'} + \frac{DF}{2A}\,\overline{v'w'} + F\,\overline{u'w'} \qquad \text{(II.1)}$$

The coefficients in this equation depend on the orientation of the probe with respect to the flow coordinates,

$$A = \cos^2\phi + k_1^2 \sin^2\phi$$
$$B = (\sin^2\phi + k_1^2 \cos^2\phi) \cos^2\theta + k_2^2 \sin^2\theta$$
$$C = (\sin^2\phi + k_1^2 \cos^2\phi) \sin^2\theta + k_2^2 \cos^2\theta$$
$$D = (1 - k_1^2) \sin 2\phi \cos\theta$$
$$E = (\sin^2\phi + k_1^2 \cos^2\theta - k_2^2) \sin 2\theta$$
$$F = (1 - k_1^2) \sin 2\phi \sin\theta$$

where

θ is the probe rotation angle (45°, 90°, 135°)

ϕ is the wire slant angle (45°)

The constants k_1 and k_2, which are known for a DANTEC 55P02 probe, depend on the construction characteristics of the slant wire probe and were taken to have the values of

$$k_1 = 0.2$$
$$k_2 = 1.02$$

as previously done by others (Pimenta 1975 [13] and Coleman 1976 [14], for example).

II.1.3 Hot-Wire Calibration

The hot-wires were calibrated in the test section in the uniform flow at the nozzle exit. A Pitot probe placed 2-3 cm to the side of the hot-wire and coupled to one of the differential pressure transducers discussed in Appendix I was used to determine the freestream velocity. The freestream air velocity in the tunnel was adjusted to different set points over the desired measurement range with the static temperature of the freestream held constant to within ± 0.1°C. At each velocity set point, 1000 anemometer voltage readings were taken and averaged. A least squares analysis was applied to the average voltages and the velocities determined from the Pitot tube to obtain a fourth order polynomial calibration equation for each wire.

In practice, the resistance of the heated wire during measurements (the operating resistance) is set above the resistance of the unheated wire (the cold probe resistance) to satisfy the desired overheat ratio requirements. The cold probe resistance is temperature dependent and must be remeasured and re-entered into the anemometer unit if the freestream temperature of the test air changes more than about ± 0.2°C from the conditions of calibration. The required operating resistance used was always 3 ohms higher than the cold probe resistance at all operating conditions. A comparison of calibration equations from a calibration done at a freestream temperature of 25.6°C (78°F) and a calibration done at a freestream temperature of 29.9°C (84°F) showed that the velocities computed with the two equations differed by less than 1% over the entire calibration range. Since these calibrations had different cold probe resistances and the operating resistances were set by adding 3 ohms to the cold probe resistance, it was concluded that calibrations of the hot-wires at one freestream temperature would be valid over a small temperature range (± 3°C) as long as the difference in the probe resistances was held at 3 ohms and the freestream temperature of the test air was not allowed to vary more than about ± 0.1°C while data were taken for a profile at a particular x-location.

II.1.4 Uncertainties

Uncertainties in the hot-wire measurements were estimated by considering the uncertainties in the Pitot-determined velocity, in curvefitting of the calibration data, in anemometer adjustments, and in probe alignment; the observed scatter in the data; and the suggested uncertainties given in the literature (Kline, Cantwell, and Lilley 1981 [56], Yavuzkurt 1982 [57]). The order of the overall uncertainties (bias and precision) associated with the hot-wire measurements are: u, 2%; $\overline{u'^2}$, 5%; $\overline{v'^2}$, 15%; $\overline{w'^2}$, 10%; and $\overline{u'v'}$, 10%.

II.2 THERMOCOUPLE PROBE

Time mean temperatures in the boundary layer were measured using a Type E (chromel-constantan) butt-welded thermocouple probe similar in design to that of Blackwell 1972 [58]. The output of the thermocouple is in the millivolt range and is measured by the ADACS.

The thermocouple probe holder, which is almost identical to the horizontal wire holder, was mounted on the same support sled used with the hot-wires. A schematic of the thermocouple probe and its support is shown in Figure II.4.

The thermocouple calibration was done in a Blue M Model MR-3210A-1 constant temperature bath, and the Hewlett-Packard quartz thermometer described in Appendix I was utilized to measure the bath temperature. The calibration water bath was in continuous movement due to an automatic stirrer, and the risk of breaking the fine thermocouple wire was large if the probe was placed directly into it. Besides, water could deposit some residue on the wire surface and the prongs, which could influence the thermocouple temperature response. Moreover, the water temperature close to the thermocouple could not be accurately monitored by the quartz thermometer. To alleviate those difficulties it was decided to insert the wire into a jar filled with alcohol, which was placed in the water bath. The quartz thermometer was also positioned in the jar next to the thermocouple probe so that it would encounter the same conditions. To prevent any air current from convecting heat to or from the alcohol surface, the opening of the jar was sealed. The time constant of the jar was also accounted for by waiting an hour after the water bath temperature had reached the steady state condition before proceeding with the temperature measurement.

Calibration was performed for temperatures between 23°C-39°C using four points over this range. The thermocouple probe voltage outputs, as measured by the ADACS, were converted to temperatures using the HP system software package. The temperature of the reference junction (the isothermal terminal block) required for software compensation is established by the ADACS via a temperature transducer which provides a 100 mV/°C output voltage. This software performs the voltage-temperature conversion by dividing the thermocouple characteristic curve into eight sectors and approximating each sector by a third order nested polynomial. The temperatures measured by the thermocouple were compared with the temperatures from the quartz thermometer over the above mentioned calibration range. The departure of thermocouple temperatures, using the software package for conversion, from the corresponding temperatures obtained by the quartz thermometer was less than ± 0.08°C.

APPENDIX III

SKIN FRICTION COEFFICIENT DETERMINATION

Skin friction coefficients in this study were determined in two ways: (1) from hot-wire measurements of Reynolds shear stress and mean velocity profiles, and (2) from Preston tube measurements. These skin friction determination methods are discussed briefly below with detailed references given for further information.

III.1 HOT-WIRE METHOD

The first means of determining the skin friction coefficients in this study was the hot-wire data method. (This procedure is the only method used for skin friction determination in the rough wall boundary layers.) Skin friction coefficients were determined using

$$\frac{C_f}{2} = \frac{\nu}{U_\infty^2}\frac{\partial u}{\partial y}\bigg|_{Y_1} - \frac{\overline{u'v'}}{U_\infty^2}\bigg|_{Y_1} - \frac{d}{dx}\left[\int_0^{Y_1}\left(\frac{u}{U_\infty}\right)^2 dy\right] + \frac{u_{Y_1}}{U_\infty}\frac{d}{dx}\left[\int_0^{Y_1}\left(\frac{u}{U_\infty}\right) dy\right] \qquad \text{(III.1)}$$

To derive equation (III.1), the Reynolds-averaged momentum equation (incorporating the usual boundary layer assumptions) and the continuity equation are integrated from the plate surface to a position Y_1 in the boundary layer. Calculations of C_f are made using equation (III.1), mean velocity profiles measured over adjacent test plates ($\Delta X = 10.2$ cm), and the measured value $\overline{u'v'}$ at $y=Y_1$. The position Y_1 was about 3.3 mm for smooth wall studies and 4 mm for rough wall studies. Further details of hot-wire data determinations of the skin friction coefficient are given by Andersen 1972 [59], Pimenta 1975 [13], and Coleman 1976 [14].

The estimated uncertainty in the hot-wire determined skin friction coefficients in this study is about ±10-12%. This estimate is based on smooth wall comparisons of the hot-wire determined values of C_f with accepted C_f correlations and with the values determined using the Preston tube.

III.2 PRESTON TUBE METHOD

The method of Preston 1954 [60] for determining the skin friction in turbulent boundary layer flows uses a simple Pitot tube (Preston tube) resting on the surface and depends upon the assumption of a universal inner law (law of the wall) common to smooth wall boundary layer flows. The difference between the total pressure at the Preston tube of 1.6 mm (1/16 in) inside diameter and the undisturbed static pressure at a pressure tap in the test section sidewall at the same x-location was measured with the pressure transducers described in Appendix I. This difference in pressure was then used in conjunction with the calibration equations as given by Patel 1965 [61] to solve for the local skin friction coefficient.

The Preston tube method of determining skin friction coefficients is only of use for the smooth plate case because calibrations have only been made for smooth walls. However, skin friction coefficient determinations made by Preston's method are quick and easy to make. The relatively low uncertainty (less than about 6%) in the skin friction coefficients determined with Preston's method made this method very important in establishing the qualification of the test facility and the correctness of the hot-wire based skin friction determination method.